ABSTRACT

Title of dissertation: LOW REYNOLDS NUMBER FLOW VALIDATION USING COMPUTATIONAL FLUID DYNAMICS WITH APPLICATION TO MICRO AIR VEHICLES

Eric J. Schroeder, Master of Science, 2005

Thesis directed by: Associate Professor James D. Baeder
Department of Aerospace Engineering

The flow physics involved in low Reynolds number flow is investigated computationally to examine the fundamental flow properties involved with Micro Air Vehicles (MAV). Computational Fluid Dynamics (CFD) is used to validate 2-D, 3-D static and hover experimental data at Reynolds numbers around 60,000, with particular attention paid to the prediction of laminar separation bubble (LSB) on the upper surface of the airfoil. The TURNS and OVERFLOW flow solvers are used with a low Mach preconditioner to accelerate convergence.

CFD results show good agreement with experimental data for lift, moment, and drag for 2-D and static 3-D validations. However, 3-D hover thrust and Figure of Merit results show less agreement and are slightly overpredicted for all measured collectives. Areas of improvement in the hover model include better vortex resolution and wake capturing to ensure that all the flow physics are accurately resolved.

Low Reynolds Number Flow Validation Using Computational Fluid Dynamics with Application to Micro-Air Vehicles

by

Eric J. Schroeder

Thesis submitted to the Faculty of the Graduate School of the
University of Maryland, College Park in partial fulfillment
of the requirements for the degree of
Master of Science
2005

Advisory Committee:

James D. Baeder, Associate Professor, Chair/Advisor
J. Gordon Leishman, Professor
Inderjit Chopra, Professor

ACKNOWLEDGMENTS

Though I am responsible for this body of work, I have received immeasurable help from many colleagues and coworkers in the Rotorcraft Center. Much thanks to Vinit Gupta for all his patience and insight. I am also indebted to Karthik Duraisamy for his wisdom and wish the Maryland basketball team the best of luck next year for his sake. Of course I would also like to thank my advisor, Dr. Jim Baeder for steering me along these two years. Others I would like to thank include Justin, Robin, and Ben; the CFD group, especially Jaina, Ayan, and Brandon, the AHS design team for sticking with it, and the Rotorcraft center as a whole. Also, to Dr. Leishman for helpful conversations throughout this journey.

Finally, to my wife: thank you so much for standing by me all these months, for your grace, for your understanding, and for your happiness. No words can say how much you mean to me.

"Your word is a lamp unto my feet, and a light unto my path." Psalm 119

TABLE OF CONTENTS

List of Tables vi

List of Figures vii

1 Introduction 1
1.1 Motivation . . . 1
1.2 Previous Work . . . 4
1.2.1 Experimental . . . 4
1.2.2 Computational . . . 7
1.3 Objectives . . . 9
1.4 Organization . . . 10

2 Flow Physics and Airfoil Geometry Considerations 11
2.1 Non-dimensional Parameters . . . 11
2.2 Pressure Distribution . . . 13
2.3 Shear Stress . . . 14
2.4 Lift, Drag, and Moments . . . 19
2.5 Reynolds Number Effects . . . 22
2.6 Static Stall Types . . . 24
2.6.1 Trailing Edge Stall . . . 24
2.6.2 Leading Edge Stall . . . 24
2.6.3 Thin Airfoil Stall . . . 25
2.7 Mach Number Effects . . . 25
2.8 3-D Effects . . . 26
2.8.1 Hover Effects . . . 28
2.9 Geometric Effects . . . 30
2.9.1 Blade Thickness . . . 30
2.9.2 Camber . . . 31
2.10 Summary . . . 31

3 Methodology 33
3.1 Mesh System . . . 33
3.1.1 Grid Generation Techniques . . . 34
3.1.2 Overset Mesh Technique . . . 35
3.2 Governing Equations . . . 40
3.2.1 Compressible Reynolds Averaged Navier–Stokes (RANS) Equations . . . 40
3.2.2 Turbulence Model . . . 44
3.2.3 Boundary Conditions . . . 45
3.3 Flow Solvers . . . 46
3.3.1 Implicit Time Marching . . . 47
3.3.2 Preconditioning . . . 47
3.3.3 TURNS . . . 48

3.3.4 OVERFLOW . . . 48
3.4 TCL/Tk Scripting . . . 49
3.5 Airfoil Geometries . . . 49
3.5.1 Leading Edge and Trailing Edge Considerations . . . 50
3.5.2 Eppler 387 . . . 51
3.5.3 Mueller . . . 51
3.5.4 Hein . . . 52

4 Results for Static Cases 54
4.1 2-D Results: Eppler 387 Airfoil . . . 54
4.1.1 The Experiment . . . 54
4.1.2 Validation . . . 54
4.1.3 Velocity Vectors . . . 57
4.1.4 Skin Friction Coefficient . . . 59
4.1.5 Pressure Contours . . . 60
4.1.6 Eddy Viscosity . . . 62
4.1.7 Low-Mach Preconditioner Results . . . 64
4.1.8 Summary . . . 64
4.2 2-D Results: Mueller Airfoil . . . 66
4.2.1 The Experiment . . . 66
4.2.2 Validation . . . 66
4.2.3 Velocity Vectors . . . 69
4.2.4 Skin Friction Coefficient . . . 69
4.2.5 Pressure Distribution . . . 71
4.2.6 Eddy Viscosity . . . 73
4.2.7 Low Mach Preconditioner Survey . . . 73
4.2.8 Summary . . . 76
4.3 Static 3-D Results: Mueller Airfoil . . . 77
4.3.1 The Experiment . . . 77
4.3.2 Validation . . . 77
4.3.3 Chordwise Flow Separation . . . 78
4.3.4 Chordwise Pressure Distribution . . . 80
4.3.5 Spanwise Pressure Contours . . . 82
4.3.6 Lift Distribution . . . 83
4.3.7 Vorticity . . . 86
4.3.8 Eddy Viscosity . . . 86
4.3.9 Summary . . . 88
4.4 Reynolds Number Effects . . . 91

5 Micro Air Vehicle in Hover 93
5.1 Experimental Setup . . . 93
5.2 Static 2-D Results . . . 94
5.2.1 Lift, Moment, Drag Curves . . . 94
5.2.2 Sharpened Leading Edge Effects . . . 97
5.2.3 Velocity Vectors . . . 97

5.2.4 Pressure Distribution . . . 99
5.2.5 Eddy Viscosity . . . 99
5.2.6 Grid Refinement . . . 99
5.2.7 Summary . . . 103
5.3 Static 3-D Results . . . 105
5.3.1 Lift, Moment, Drag Curves . . . 105
5.3.2 Contours of Chord-wise Recirculation . . . 105
5.3.3 Pressure Distribution . . . 107
5.4 Summary . . . 107
5.5 Hover 3-D Results . . . 109
5.5.1 Convergence . . . 111
5.5.2 Performance Curves . . . 111
5.5.3 Flowfield . . . 115
5.5.4 Lift and Thrust Distributions . . . 121
5.5.5 Chordwise Flow Separation . . . 123
5.5.6 Summary . . . 126

6 Summary and Conclusions 127
6.1 Future Work . . . 131

Bibliography 133

LIST OF TABLES

4.1 Eppler 387 Turbulent Viscosity Levels, ν_t 62

4.2 Mueller 2-D Turbulent Viscosity Levels 75

4.3 Mach Number Survey Results (**—No low Mach Preconditioner) . . 75

4.4 Mueller 3-D Turbulent Viscosity Levels, ν_t 88

5.1 Hein 2-D Turbulent Viscosity Levels, ν_t 101

5.2 2-D Grids used in Refinement Study 103

LIST OF FIGURES

2.1 Characteristic pressure contours on a NACA 0012 14

2.2 Boundary Layer profiles, from Leishman [25] 15

2.3 Laminar Separation Bubble, from Leishman [25] 18

2.4 Chord-axis system, from Leishman [25] 20

2.5 Representative results for NACA 0012, $M = 0.1$, $Re = 1,000,000$ . . 21

2.6 Reynolds number effects on NACA 64-210, from Leishman [25] . . . 23

2.7 Qualitative flowfield at low Reynolds numbers, from Bastedo [13] . . 27

2.8 Flow near a hovering rotor, from Leishman [27] 29

3.1 Curvilinear Coordinate Transformation from Holst [28] 34

3.2 2-D C-type Grid made with hyperbolic grid generator 36

3.3 A C-O grid topology created by algebraically collapsing 2-D airfoil sections at the tip 37

3.4 A single axial plane in background mesh models 1/2 the rotor disk. This mesh was created by an algebraic grid generator. 38

3.5 A blade mesh surrounded by a background mesh 39

3.6 A hole cut in the background mesh 40

3.7 Wake cut boundary condition at trailing edge of airfoil 46

3.8 TCL Interface 50

3.9 Eppler 387 Airfoil 52

3.10 Mueller Airfoil 53

3.11 Hein Airfoil 53

4.1 Eppler 387 2-D Results 56

4.2 Eppler 387 Velocity Vectors 58

4.3 Skin Friction Coefficient over Eppler 387 2-D airfoil 60
4.4 Pressure distribution 61
4.5 Eddy viscosity ratio over Eppler 387 airfoil at $\alpha = 2.93°$ 64
4.6 Eppler 387 Eddy viscosity ratio 65
4.7 Mueller 2-D Results 67
4.8 Mueller 2-D Velocity Vectors 70
4.9 Skin Friction Coefficient over Mueller 2-D airfoil 71
4.10 Mueller 2-D Pressure Contours 72
4.11 Pressure Contour for Different Flow Solvers 73
4.12 Contours of eddy viscosity ratio over Mueller 2-D airfoil 74
4.13 Mueller 3-D Results 79
4.14 Mueller Wing Chordwise Reverse Flow Regions for Semi-Span Wing . 81
4.15 Pressure Distribution for Mueller 3-D Results 82
4.16 Pressure Contour over Mueller wing, $\alpha = 6°$, $x/c = 0.61$ 83
4.17 Lift Distribution 84
4.18 Pressure Contours showing vortex development over wing tip, $\alpha = 6°$ 85
4.19 Chordwise vorticity showing vortex development over wing tip, $\alpha = 6°$ 87
4.20 Eddy Viscosity, $\alpha = 6°$ 89
4.21 Eddy Viscosity, $\alpha = 12°$ 90
4.22 Reynolds Number Effects 92

5.1 Hein 2-D Results 96
5.2 Close-up of Leading Edge of Hein Airfoil 98
5.3 Hein 2-D Velocity Vectors 100
5.4 Hein 2-D Pressure Distribution 101

5.5 Eddy Viscosity Contours over Hein 2-D airfoil 102
5.6 Grid Refinement Study Results 104
5.7 Hein 3-D Lift, Moment, Drag Curves 106
5.8 Regions of Chordwise Recirculation 108
5.9 Hein 3-D Pressure Contours, $\alpha = 15°$ 109
5.10 Flow Visualization for Hein rotor, from [11] 110
5.11 Hein Rotor Convergence Rates 112
5.12 Hein Hover Results 112
5.13 Hein Rotor Performance 113
5.14 Hein Rotor Ideal Power 114
5.15 Hein Rotor Actual Power 115
5.16 Background mesh, $\theta = 8°$ 116
5.17 Wake Contraction in Hover 118
5.18 Velocity Flow-field at $\theta = 8°$, 63% span, looking from trailing edge . . 119
5.19 Axial velocity and pressure contours in the plane of the rotor, $\theta = 8°$ 120
5.20 Velocity Flowfield at $\theta = 8°$, 63% span, looking from the trailing edge 120
5.21 Induced Inflow at $\frac{1}{2}c$ Below the Rotor 121
5.22 Lift Distribution for Hovering MAV 122
5.23 Spanwise Thrust Distribution for Hovering MAV 124
5.24 Regions of chord-wise flow separation 125

NOMENCLATURE

ABBREVIATIONS

AR	Aspect Ratio, R^2/S_{ref}
BEMT	Blade-Element Momentum Theory
CFD	Computational Fluid Dynamics
FM	Figure of Merit
LSB	Laminar Separation Bubble
LE	Leading Edge
MAV	Micro Air Vehicle
TE	Trailing Edge
UAV	Unmanned Air Vehcile

SYMBOLS

a_∞	Local speed of sound
A	Axial force
c	Chord
C_d, C_D	Drag coefficient
C_{d_0}	Zero-lift drag coefficient
C_{f_x}	Skin Friction coefficient
C_l, C_L	Lift coefficient
C_{l_α}	Lift curve slope
$C_{L_{MAX}}$	Maximum lift coefficient
C_m, C_M	Moment coefficient
C_p	Pressure coefficient
C_P	Power coeficcient, $P/(\rho A(\Omega R)^3)$
$C_{P_{actual}}$	Actual Power coeficcient
$C_{P_{ideal}}$	Ideal Power coeficcient
$C_{P_{induced}}$	Induced Power coefficient
$C_{P_{profile}}$	Profile Power coefficient
C_T	Thrust coefficient, $T/(\rho A(\Omega R)^2)$
$\frac{C_T}{\sigma}$	Blade loading coefficient
e	Energy per unit volume
f_x,f_y,f_z	Cartesian body force components
H	Stagnation enthalpy per unit volume
J	Determinant of Jacobian for coordinate transformations
k	Coefficient of thermal conductivity
L	Lift force
L	Characteristic length
L/D	Lift-to-Drag ratio
M	Local Mach Number
M_{root}	Root Mach Number
M_{tip}	Tip Mach Number

M_∞	Freestream Mach number
N	Normal force
N_b	Number of Blades
p	Local Pressure
p_∞	Freestream Pressure
q_∞	Dynamic Pressure
R	Blade radius
R_{WAKE}	Wake radius
Re	Reynolds Number
Re_{root}	Root Reynolds Number
Re_{tip}	Tip Reynolds Number
Re_x	Local Reynolds Number
S_{ref}	Reference Area
T	Static temperature
t/c	Non-dimensional thickness
V_∞	Free stream velocity (m/s)
x/c	Non-dimensional chord location

GREEK SYMBOLS

α	Angle of attack (deg)
α_0	Zero-lift angle of attack (deg)
γ	Specific heat ratio
δ	Boundary layer thickness
θ	Collective angle (deg)
κ	Induced power factor
μ	Laminar viscosity
μ_t	Turbulent viscosity
ρ_∞	Density of air
σ	Rotor solidity
τ	Shear stress force
τ_w	Shear stress force at wall
ΩR	Rotor tip speed

Chapter 1

Introduction

1.1 Motivation

Over the past decade, Micro Air Vehicles (MAVs) have received an increasing amount of attention in military and civilian markets. With a characteristic length no longer than 15 cm (6 in.), MAVs are barely detectable to the naked eye at 100 yards. This stealth capability makes MAVs a prime candidate for surveillance, detection, and reconnaissance missions. Often, prototype MAVs have been outfitted with cameras with the ability to send and receive data. Unmanned Air Vehicles (UAVs) have already begun undertaking this task in Iraq and Afghanistan, with their number to increase over the next several years. With the advent of MAV feasibility, these aircraft will be able to be produced cheaply and in large quantity. MAVs have the potential, therefore, to be used in high-risk situations rather than losing a larger (more expensive) UAV or a full-size aircraft.

MAV research generally falls into three vehicle classes: fixed wing, rotary wing, and flapping wing. Each class of MAVs has unique benefits and problems because the aerodynamics of each class is different, due to the different range of operating Reynolds numbers. The Reynolds number (Re) can be defined as the non-dimensional ratio of inertial to viscous forces, thus the viscous forces become more dominant with a decrease in Reynolds number.

MAVs generally fly in the Reynolds number range of 1,000 to 120,000 (whereas full size helicopters and airplanes experience Reynolds numbers on the order of 10^7). Fixed-wing MAVs fly at the upper end of this range at Reynolds numbers of on the order of 10^5 [1]. Rotary-wing MAVs generally fly in the 20,000 to 70,000 Reynolds number range, though the smallest rotary-wing MAVs may fly at a Reynolds number below 10,000 [2] – [10]. Flapping-wing MAVs usually fly in the Reynolds number range between 1,000 and 10,000 — a range in which viscous effects can be expected to be significant.

Each class of MAVs show promise, though the rotary-wing class has several key advantages. Primary among these is the ability to hover, which allows the vehicle to remain stationary in the air while gathering information or waiting for a signal to move. Additionally, the ability of a rotary-wing aircraft to takeoff and land vertically gives it operational flexibility by requiring minimal takeoff and landing zones. Because a rotary wing vehicle can fly in any direction, it is ideal for use in pursuit or search and rescue missions where the flight path is dynamic. Most rotary-wing MAVs can also better withstand crosswind gusts that may destabilize aircraft in other classes of MAVs.

Rotary MAV development is hindered in part by relatively poor aerodynamic efficiency of the rotor, defined as the figure of merit (FM) — most other development issues have to do with power [11]. The figure of merit is defined as the ratio of ideal power required to actual power required. MAV rotors have achieved a FM around 0.6 while full-scale helicopters may have a FM near 0.80 or higher [3]. This relatively low FM is in part due to degraded airfoil performance at low Reynolds

numbers where the flow is susceptible to separate at a relatively low angle of attack. Induced losses also increase at low Reynoldsnumber. In addition, the large viscous forces and the associated thick boundary layer result in a higher viscous drag, and a lower maximum lift coefficient. Laminar separation bubbles (LSBs) often form on the upper surface of the airfoil at Reynolds numbers above 50,000, and often lead to a substantial decrease in performance (L/D) [1].

A good airfoil choice for MAVs will try to accomplish several goals: to delay the onset of the laminar separation bubble and therefore flow separation, to achieve a high maximum lift coefficient, and to keep induced and profile drag at a minimum. Thus, the selection of airfoils is of paramount importance; however, few experimental and computational studies have systematically investigated thin, cambered airfoils and wings of low aspect ratio which are commonly used in MAVs. There is noticeably little research on comparing low Reynolds number experimental data to computational models, particularly with application to rotary-wing MAVs [3, 9].

To aid the selection process of airfoils, Computational Fluid Dynamics (CFD) can be used where low Reynolds number flows are too difficult to investigate experimentally. CFD is also useful in extrapolating on published results when there is a gap in experimental data, or where little data is available. Thus, a more judicious approach to selecting airfoils can be made using CFD. However, CFD typically has difficulty in predicting the location and size of the laminar separation bubble which in turn may result in poor quantitative predictions for lift, moment, and drag. Poor aerodynamic prediction may also result from the fact that low Reynolds number

flows are not well understood computationally due to inherent problems in modeling thicker boundary layers where the flow may transition from laminar to turbulent. While CFD methods have been validated for a number of airfoils, reliance solely on computational results is ill-advised at this point [3, 9].

1.2 Previous Work

Low Reynolds number flows have been investigated experimentally for dozens of years, although there has been an increase in work in this area in the last decade. Most experimental work focuses on the problems associated with low Reynolds number flow, with particular attention paid to laminar separation bubble formation and transition. Several computational studies have also been completed although relatively few have validated experimental data.

1.2.1 Experimental

A comprehensive study on low Reynolds number flow physics and pre-1981 low Reynolds number data can be found in the work of Carmichael [12]. This reference also contains a good qualitative description of the flow physics in different Reynolds number flight regimes.

Mueller [1] has conducted extensive experimental studies on 2-D and 3-D flow around flat plates and cambered airfoils at Reynolds numbers ranging from 60,000 to 200,000. The data show that cambered plates offer better aerodynamic performance characteristics than flat plates. Additionally, it is shown that the trailing

edge geometry has little effect on the lift and drag on thin wings at low Reynolds numbers. Several of the experiments from Mueller's research are validated in this thesis. Mueller has also published data with other researchers [6, 7], though this data is in more complete form in Ref. [1].

Selig [5] has published a large and consistent amount of 2-D experimental data on low Reynolds number airfoils. Lift, moment, and drag data is available for over 100 airfoils that have all been tested systematically in the same wind tunnel using the same force balance and wake rake. Several of these airfoils are examined in Ref. [5], where it was noted that the influence of laminar separation bubbles was found to significantly affect performance of several high-lift airfoils in the Reynolds number range of 80,000 to 150,000. Additionally, degraded performance at Reynolds numbers of 40,000 may be improved by using boundary layer trips to make the flow over the airfoil more turbulent, and therefore potentially attached for a greater distance.

Bastedo and Mueller [13] provide an excellent discussion on the effect of tip vortices on spanwise pressure distributions with special attention to laminar separation bubble formation. Results from 2-D and 3-D measurements show that increasing the Reynolds number increases performance while decreasing the aspect ratio decreases performance due to tip vortex effects. The laminar separation bubble was found to exist over the majority of the blade span except near the tip.

Results from Laitone [8, 17] suggest that a good airfoil for use in flow with Reynolds numbers less than 70,000 should be a thin plate with 5% circular arc camber. This type of airfoil has a better L/D at low Reynolds numbers compared

to a NACA 0012, and a reversed NACA 0012, among others. Additionally, the thin, cambered airfoil geometry produced a higher total lift for all angles of attack. Sharpening the leading edge resulted in the largest lift curve slope, similar to the findings in Ref. [15].

O'Meara and Mueller [18] analyzed laminar separation bubble length and height with respect to Reynolds number and angle of attack over a Reynolds number range of 50,000 to 200,000. Their results included the fact that increasing the Reynolds number decreases the bubble length while increasing the bubble height. Alternatively, increasing the angle of attack from $\alpha = 10^\circ$ to $\alpha = 12^\circ$ increased both bubble height and length. Increasing bubble height may improve performance by acting as a boundary layer trip. However, lengthening the bubble generally decreases performance and usually leads to a low $C_{L_{MAX}}$ associated with thin airfoil stall.

Sathaye, et al. [4] investigated a NACA 0012 wing with an aspect ratio of unity in the Reynolds number range of 30,000 to 90,000. Their results show that a dramatic increase in induced drag coefficient is observed for Reynolds numbers below 50,000. An additional experiment with a 3% thin flat plate with a sharpened leading edge gives the interesting result of the maximum lift per unit span at the mid-span location, and then tapering off to the tip, due to the tip vortex formation.

Marchman [14] investigated Reynolds number flows in the range of 50,000 to 500,000 with emphasis on methods of data acquisition. This gives good insight into the underlying problems in gathering low Reynolds number lift and drag data, namely that hysteresis is often present if the wind tunnel turbulence intensity is too high. Lowson [15] completed a similar analysis and suggests that data taken

from a balance will give results showing higher drag, lower lift, and more significant hysteresis compared to data using wake rakes. Lowson also claims that the airfoils that offer the best performance in this flight regime are thin, cambered blades with sharpened leading edges.

Additionally, Ol et al. [16], compared laminar separation bubble formation over an SD7003 airfoil in three different facilities (water tow tank, wind tunnel, and water tunnel). The main result was that the LSB had qualitatively similar shape and velocity gradient, but differed in the measured location and flow structure due to differences in the facilities. This result gives good insight into the possibility of discrepancy between experimental facilities.

1.2.2 Computational

Several authors [2, 19] have computationally and experimentally investigated airfoils at ultra-low Reynolds numbers (below 10,000). Though this research is not directly applicable to the present study, it still gives good insight into viscous-dominated flows.

Singh et al. [20], performed computations using XFOIL over several airfoils at $Re = 80,000$. XFOIL is a freeware program that computes basic airfoil performance characteristics with extension to viscous flows. Their results show that a thin, cambered airfoil (8.89%) from Selig had the best lift and drag characteristics over thicker, less cambered Wortmann and NACA symmetric airfoils.

Kellogg and Bowman [21] completed a parametric computational study on

the thickness of MAV airfoils for the Reynolds numbers of 60,000, 100,000, and 150,000 and found that decreasing the Reynolds number also decreased the optimal thickness with respect to L/D. Thus, an airfoil designed for use in low Reynolds number flow should be relatively thin.

Bohorquez et al. [3] give a good computational and experimental investigation of a rotary MAV. The computational results agree reasonably well with the experimental results with respect to figure of merit. However, the computational model predicted less flow separation than was found experimentally, resulting in an over-prediction of rotor performance. This study examined the rotor performance as a whole rather than analyzing 2-D and 3-D airfoil characteristics. This study has helped lay the groundwork for this thesis in marrying a rotary-wing MAV experiment with a computational model.

Shum [22] developed a computational model to investigate laminar separation bubble size and reattachment velocity gradient over an Eppler 387 airfoil at $Re = 200,000$. Though the Reynolds number is larger than the range in which rotary MAVs operate, the discussion on LSBs gives a good understanding of the flow physics. Elimelech, et al. [23], conducted a similar study comparing experimental and computational results on turbulence characteristics over NACA 0009 and Eppler 61 airfoils. It was found that a very fine mesh could capture the turbulence quite well compared to flow visualization and suggested that these airfoils transition from laminar to turbulent flow in the Re =20,000 to 60,000 range at low angles of attack.

Low Mach number flows have been investigated by Gupta and Baeder [24]

in a computational study of a quad-tiltrotor using the Transonic Unsteady Rotor Navier-Stokes (TURNS) code (used in this thesis). The flow solver implemented a low-Mach pre-conditioner but at a significantly higher Reynolds number than in this thesis. This thesis has built on their work and extends the computations to the low Reynolds number regime.

1.3 Objectives

This research has been undertaken for several reasons:

1. Computational validation of experimental data has rarely been conducted in the Reynolds number range of 20,000 to 100,000. The current work aims to not only add to the computational validations of low Reynolds number flow but also to thoroughly investigate the flow physics. Low Reynolds number flow is well understood from a theoretical viscous flow perspective but not as well from a computational aerodynamics perspective. In particular, the ability of current CFD codes to correctly model the laminar separation bubble and the transition to turbulence is of importance. To have confidence in the flow solver, it is imperative to ensure that the flow physics is represented correctly.

2. Validating experimental data from various wind tunnels and different researchers gives the flow solver credibility. Because the low-Mach preconditioner has not been validated in the literature yet, this thesis paves the way for future use of this capability through validation with experimental results. The TURNS flow solver has already been used for several other applications, and this thesis aims to

further extend its capability.

3. Rotary-wing MAVs, due to their unique capabilities, have received increasing attention from industry, government, and academia. For instance, there exists a good foundation of experimental work at the University of Maryland with low Reynolds number flow with application to MAVs. This thesis aims to validate CFD as a tool to systematically investigate issues/problems that are hindering rotary MAV development, and further extend the computational research tools available to those persons interested in MAV performance.

1.4 Organization

A quick treatment of the underlying flow physics, with special attention paid to low Reynolds number aerodynamics and applicable geometric considerations is given in Chapter 2. The governing equations are presented in Chapter 3 along with the computational methodology and grid topology for the 2-D and 3-D validations. Results from 2-D and 3-D static cases are presented with validation with experimental data in Chapter 4, with figures examining velocity vectors, chordwise and spanwise pressure distributions, eddy viscosity, and other flow properties. Results from a 3-D hover CFD model are presented in Chapter 5 with validation against experimental data for a rotary MAV. A summary concludes this thesis in Chapter 6.

Chapter 2

Flow Physics and Airfoil Geometry Considerations

In this chapter, the fundamental flow properties of low Reynolds number aerodynamics are examined to gain insight into the flow physics of MAVs. Low Reynolds number flow consists of a smaller ratio of inertial forces to viscous forces, leading to relatively thick boundary layers and high viscous drag. MAV blade designs attempt to overcome the Reynolds number effects by introducing camber into the blade planform to produce more lift and keeping the blade thickness low. By designing a blade to promote a short laminar separation bubble, the flow may remain attached downstream over the airfoil surface in the form of a turbulent boundary layer, giving better performance.

2.1 Non-dimensional Parameters

Non-dimensionalizing flow characteristics allows for comparisons to be made between airfoils under the same dynamic conditions. The non-dimensionalization of the Navier-Stokes equations leads to two key non-dimensional parameters: Mach number and Reynolds number. The free-stream Mach number relates the free-stream convection velocity, V_∞, to the local speed of sound, a_∞:

$$M_\infty \equiv \frac{V_\infty}{a_\infty} \tag{2.1}$$

where, for a perfect gas:

$$a_\infty = \sqrt{\frac{\gamma p_\infty}{\rho_\infty}} \tag{2.2}$$

where γ is the ratio of specific heats of the fluid, ρ is the density of the fluid, and p is the pressure of the fluid. The Reynolds number relates the inertial forces to the viscous forces:

$$Re \equiv \frac{\rho_\infty V_\infty c}{\mu} \tag{2.3}$$

where μ is the absolute viscosity of the fluid and c is the characteristic length, generally taken to be the chord for aerodynamic applications. For micro air vehicles, the velocities and chord size are both relatively small, and the flow is characterized by low Mach numbers and low Reynolds numbers. Thus, the flow is nearly incompressible and viscous forces dominate with relatively thick boundary layers. Rotary MAVs may experience tip Mach numbers of around 0.15, with regions of local Mach number possibly above 0.3, where compressibility effects cannot be completely ignored.

An additional non-dimensional parameter is the blade aspect ratio which relates the blade radius R to the reference area S_{ref}, generally taken as the total blade area:

$$AR \equiv \frac{R^2}{S_{ref}} \tag{2.4}$$

For a rectangular blade, this definition reduces to:

$$AR \equiv \frac{R}{c} \tag{2.5}$$

which is simply the ratio of blade radius to chord. Due to size limitations, rotary MAVs generally are constrained to relatively low aspect ratio blades in the range

of $AR = 1 - 5$ while a full-size helicopter may have blades with aspect ratio of 10 or higher. Low aspect ratio blades have degraded performance due to a more significant influence of the tip vortex on the spanwise lift distribution [13]. Low aspect ratio blades generally have the same zero-lift angle of attack as high aspect ratio blades but will have a more shallow lift-curve slope [4].

2.2 Pressure Distribution

The pressure coefficient is a non-dimensional parameter that relates the local pressure differential to the free-stream, dynamic pressure ($q_\infty = \frac{1}{2}\rho_\infty V_\infty^2$):

$$C_p \equiv \frac{p - p_\infty}{\frac{1}{2}\rho_\infty V_\infty^2} \tag{2.6}$$

which for a perfect gas can be rewritten as:

$$C_p = \frac{2}{\gamma M_\infty^2}\left(\frac{p}{p_\infty} - 1\right) \tag{2.7}$$

An example of chord-wise pressure distribution over a NACA 0012 airfoil is given in Figure 2.1 for several angles of attack for moderate Mach number and Reynolds number. The chord-wise pressure distribution is negative (suction) over the majority of the airfoil except for a region of positive pressure near the leading edge (near the stagnation point). For small positive lift, a suction peak forms on the upper surface near the leading edge. As the angle of attack increases, the negative pressure peak is increased in magnitude and covers a larger portion of the upper surface near the leading edge. This is due to the rapid acceleration of the flow as it traverses around the leading edge. The pressure will increase downstream of the

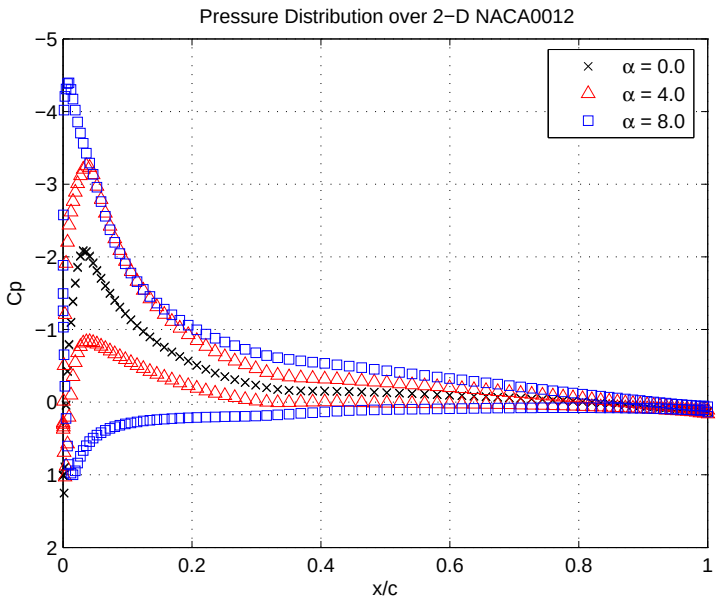

Figure 2.1: Characteristic pressure contours on a NACA 0012

suction peak, creating an adverse pressure gradient that will tend to decelerate the flow. If the adverse pressure gradient is strong enough (brought about by increasing the angle of attack), the flow is susceptible to separation.

2.3 Shear Stress

A boundary layer will form around an airfoil surface due to friction between the fluid and the wall. A boundary layer around an airfoil can be described as the region in which the flow velocity increases from zero at the airfoil surface to 99% of the free-stream velocity, and thickens downstream on the airfoil surface due to increasing shear stress. Boundary layers have two main forms, while a transition phase also exists between the two. The first type is a laminar boundary layer, which is characterized by low levels of mixing between adjacent layers, and is relatively

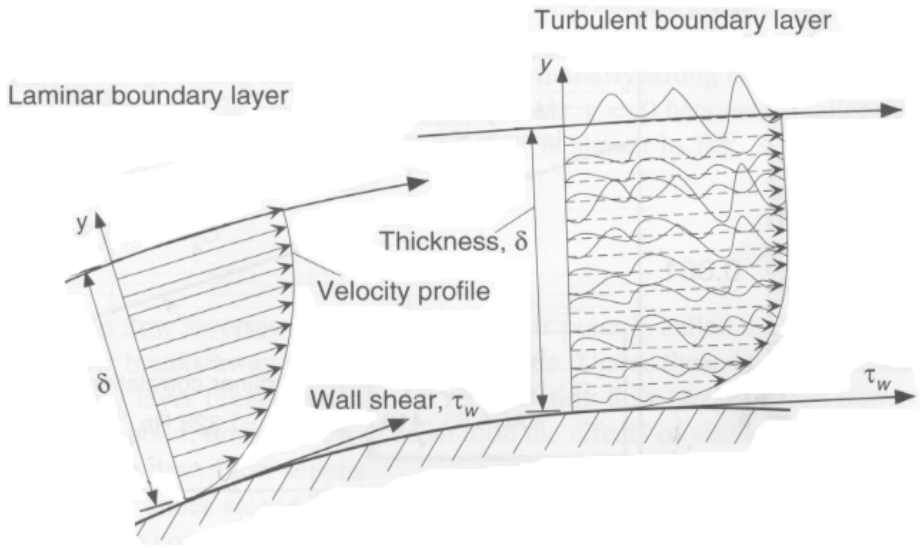

Figure 2.2: Boundary Layer profiles, from Leishman [25]

thin. In contrast, a turbulent boundary layer is relatively thick with significant mixing between adjacent layers. These two main types of boundary layers can be seen in Figure 2.2.

It is important to discuss shear stress in conjunction with boundary layers. Shear stress is the physical force that produces a resistance that tends to slow down the flow. Shear stress, which is tangential to the surface, is related to the absolute viscosity and is given by:

$$\tau = \mu \left(\frac{\partial u}{\partial y} + \frac{\partial v}{\partial x} \right) \tag{2.8}$$

where μ is the absolute viscosity of the fluid. Equation 2.8 can be approximated at the surface by $(y = 0)$:

$$\tau_w \approx \mu \frac{\partial u}{\partial y} \tag{2.9}$$

When the velocity gradient changes from positive to negative, the shear stress

changes sign as well and effectively decelerates the flow. If the shear stress is strong enough (which will also lead to an adverse pressure gradient), the flow will separate and reverse the flow direction at the surface.

The local shear stress is a function of the non-dimensional chord position, x/c, although it is usually more convenient to define a skin friction coefficient that is dimensionless (useful in calculating drag):

$$c_{f_x} \equiv \frac{\tau_w}{\frac{1}{2}\rho_\infty V_\infty^2} \tag{2.10}$$

For laminar flow, the Blasius solution to equation 2.10 for a flat plate in a zero pressure gradient is given by (with $Re_x = \rho_\infty V_\infty x/\mu_\infty$):

$$c_{f_x} = \frac{0.664}{\sqrt{Re_x}} \tag{2.11}$$

The laminar boundary layer thickness is given by:

$$\delta = \frac{5.2x}{\sqrt{Re_x}} \tag{2.12}$$

For a turbulent boundary layer, the Blasius solution to equation 2.10 for a flat plate in a zero pressure gradient is similarly given by:

$$c_{f_x} = \frac{0.0592}{Re_x^{0.2}} \tag{2.13}$$

The turbulent boundary layer thickness is given by:

$$\delta = \frac{0.37x}{Re_x^{0.2}} \tag{2.14}$$

Because a turbulent boundary layer is thicker than a laminar boundary layer, the laminar shear stress is also less than the turbulent shear stress. Thus, an airfoil

that promotes laminar boundary layers will in general have less skin friction drag. The skin friction coefficient can be integrated over the chord to find the skin friction drag. Using equation 2.11, the resultant drag over a flat plate is:

$$C_D(L) = \frac{1}{L}\int_0^L C_f dx = 2C_f(L) = \frac{1.328}{\sqrt{Re_L}} \tag{2.15}$$

where L is the length of the chord [26]. The turbulent drag due to skin friction is similarly calculated using the results of equation 2.13:

$$C_D(L) = 0.1166 Re_L^{-0.2} \tag{2.16}$$

At low Reynolds numbers, the skin friction drag may add a significant contribution to the total calculated drag at low angles of attack where the flow is not separated. Drag is discussed further in Section 2.4.

Near the leading edge of the airfoil, the flow is laminar and at higher Reynolds numbers this region of laminar flow only exists for a short while (generally 2-15% chord) before transitioning to turbulent flow. At low Reynolds numbers, the flow may be laminar over the majority of the airfoil at low angles of attack. When the flow encounters an adverse pressure gradient on the upper surface of the airfoil, it begins to decelerate. The flow near the surface will be affected significantly by the shear stress on the airfoil, because there is no momentum transfer between layers. If the pressure gradient is strong enough over the airfoil surface (brought about by a high angle of attack), the flow will separate. The mode of separation varies with airfoil and flow characteristics, and is discussed in conjunction with static stall in Section 2.6.

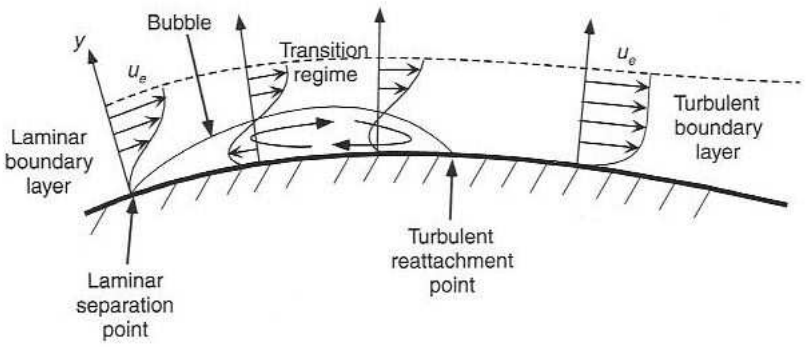

Figure 2.3: Laminar Separation Bubble, from Leishman [25]

Generally a laminar boundary layer separates and soon re-attaches downstream on the airfoil as a turbulent boundary layer. The transition from laminar flow to turbulent flow may cause a laminar separation bubble to form on the airfoil surface. Laminar separation bubbles are constant pressure regions of recirculating flow, found on the upper surface of an airfoil toward the leading edge. A schematic of a laminar separation bubble is in Figure 2.3. Laminar separation bubbles are commonly found on airfoils in the low Reynolds number regime due to the relatively high viscous forces that cause the flow to separate at relatively low angles of attack. Laminar boundary layers are advantageous because they have a lower profile drag. However, though a turbulent boundary layer has a higher profile drag, it is less likely to separate. This is advantageous because the airfoil will produce more lift and will undergo deep stall at a higher angle of attack, giving better performance. Thus, it is more beneficial for the flow to be turbulent over the airfoil from a performance perspective. Boundary layer trips may be used on some airfoils to artificially force transition to a turbulent boundary layer to give better performance.

Laminar separation bubbles, therefore, may be beneficial to airfoil performance by providing a natural trip to turbulent, attached flow. However, there exists two types of separation bubbles which have differing effects on airfoil performance. A short separation bubble is generally a few percent of the chord and does not modify the pressure distribution significantly. These bubbles serve as a tripping mechanism to allow reattachment of an otherwise separated shear layer, increasing performance. A long bubble, however, may cover 20-30% of the airfoil and degrades performance because the flow is separated for a significant part of the airfoil [13]. As discussed in Ref. [18], decreasing the Reynolds number will increase the bubble length while decreasing the height, tending for the bubble to be long rather than short. The type of separation bubble plays a key role in determining the type of static stall and the maximum lift coefficient and is discussed further in Section 2.6.

2.4 Lift, Drag, and Moments

The forces and moments on the airfoil are obtained by integrating the local values of pressure and shear stress acting normal and parallel to the airfoil surface. The forces are resolved using a chord-axis system as seen in Figure 2.4 to obtain the normal and axial forces acting on the airfoil, and from these, the lift, moment, and drag can be derived by integration along the airfoil .

The lift, drag, and moment coefficients are defined as $\left(q_\infty = \frac{1}{2}\rho V_\infty^2\right)$:

$$C_l = \frac{L}{q_\infty c} \tag{2.17}$$

$$C_d = \frac{D}{q_\infty c} \tag{2.18}$$

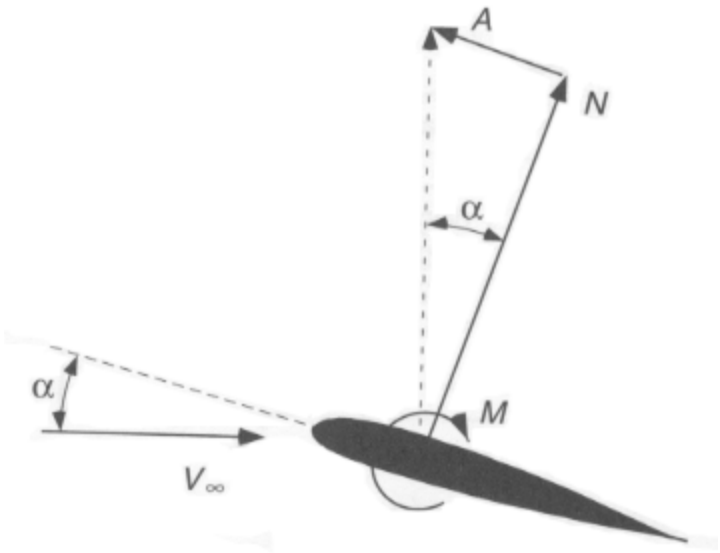

Figure 2.4: Chord-axis system, from Leishman [25]

$$C_m = \frac{M}{q_\infty c^2} \tag{2.19}$$

where the pitching moment is defined as positive nose-up. Representative airfoil characteristics are shown for a NACA 0012 airfoil at $M = 0.1$ and $Re = 10^6$ in Figure 2.5.

The lift-curve slope is linear through the majority of the angle of attack and is defined (in a least squares sense) using α_0 = zero-lift angle of attack, as follows:

$$C_{l_\alpha} = \frac{C_l}{\alpha - \alpha_0} \approx 2\pi \tag{2.20}$$

For the NACA 0012, $C_{l_\alpha} = 5.62$ and $\alpha_0 = 0°$. At high angles of attack the lift-curve slope becomes nonlinear due to airfoil stall, which occurs around $\alpha = 16°$ in Figure 2.5(a). Additionally, formation of the laminar separation bubble at low Reynolds numbers may also make the lift curve slope nonlinear because the bubble

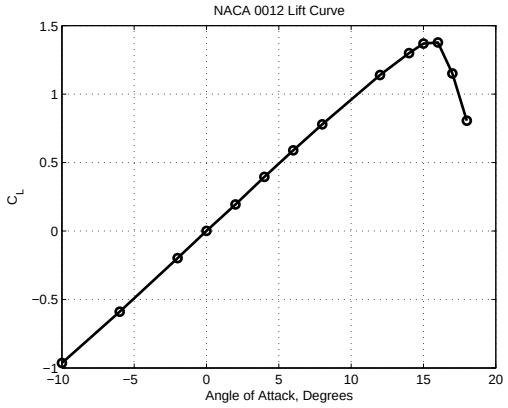

(a) Lift

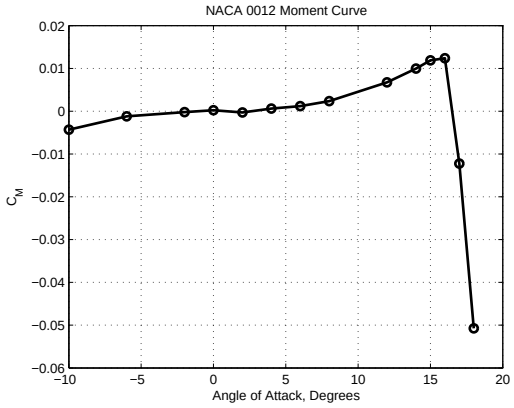

(b) Moment

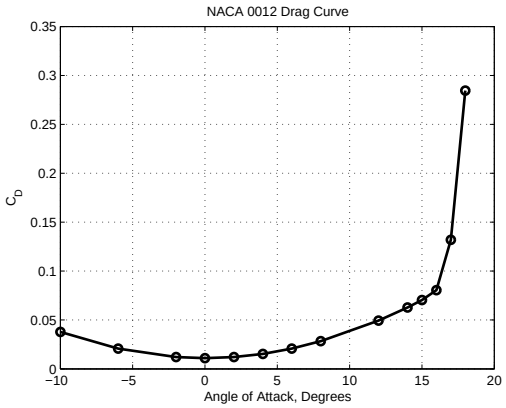

(c) Drag

Figure 2.5: Representative results for NACA 0012, $M = 0.1$, $Re = 1,000,000$

may move or change size (depending on angle of attack) which may have a significant effect on the lift, moment, and drag calculations.

The pitching moment curve in Figure 2.5(b) is typical of symmetric airfoils and is usually a good indicator of stall. As the angle of attack increases and the airfoil approaches stall, the airfoil may pitch up slightly before pitching down dramatically. Alternatively, cambered airfoils may exhibit more extreme pitching moments than symmetric airfoils .

Figure 2.5(c) shows a characteristic drag curve for symmetric airfoils like the NACA 0012. The minimum drag occurs around $\alpha = 0^\circ$ and at a zero-lift drag coefficient (C_{d_0}) of 0.01. In the separated flow region above $\alpha = 15^\circ$, there is a significant contribution to the overall drag by pressure drag due to separation. At lower angles of attack, the skin friction drag component is more significant because there is less pressure drag than at high angles of attack. Skin friction drag, or viscous drag, may be relatively high for airfoils operating at low Reynolds numbers at moderately low angles of attack due to the thicker boundary layers and is discussed further in the next section.

2.5 Reynolds Number Effects

The low Reynolds number commonly associated with MAVs is due to their small size as well as their relatively slow velocities. Therefore, viscous forces will have a stronger influence on airfoil characteristics in low Reynolds number flow. There are several effects brought about by the low Reynolds number flow. The

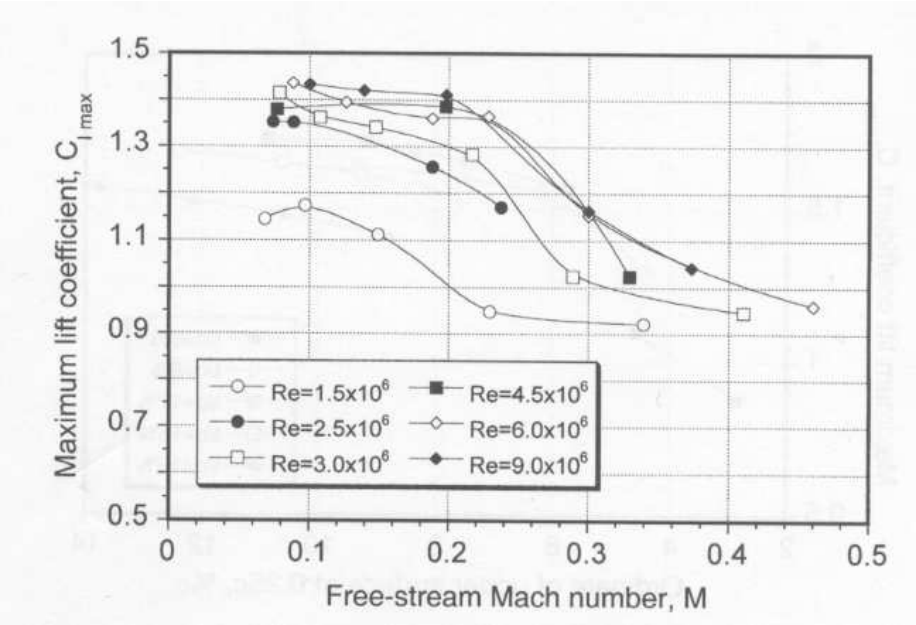

Figure 2.6: Reynolds number effects on NACA 64-210, from Leishman [25]

main physical effect is that the relatively high viscous forces tend to thicken the boundary layer although the flow may be laminar for a larger portion of the airfoil. The thicker boundary layer will increase skin friction drag due to increased shear stress. Laminar flow over the airfoil may degrade performance if a long separation bubble forms on the upper surface, which tends to occur at low Reynolds numbers as suggested by Refs. [13] and [18]. Generally, airfoils operating at low Reynolds numbers will also tend to have a lower maximum lift coefficient, as can be seen in Figure 2.6, because the flow is apt to separate at lower angles of attack. All of the effects discussed here are generally not desirable, but understanding the issues that negatively affect performance is the first step in airfoil selection.

2.6 Static Stall Types

Airfoils generally stall in three different ways although some airfoils may exhibit stall characteristics of more than one type. Stall can be difficult to characterize due to the large amount of flow recirculation.

2.6.1 Trailing Edge Stall

Trailing edge stall is typical of thicker airfoils. The large leading edge radius of curvature results in moderate suction peaks near the leading edge with relatively small negative pressure gradients downstream that lead to attached flow over most of the airfoil. As the angle of attack increases, the turbulent separation point moves forward from the trailing edge of the airfoil toward the leading edge. The flow separation at the trailing edge significantly raises drag even though the airfoil has not fully stalled. This will also cause the lift-curve slope to flatten, and eventually the airfoil reaches $C_{L_{MAX}}$. This is accompanied by a slight rise in nose-up pitching moment just before the airfoil stalls, at which point the pitching moment will plunge nose-down [25]. This type of stall is moderately abrupt compared to other types.

2.6.2 Leading Edge Stall

Airfoils that exhibit short laminar separation bubbles generally have a leading edge stall type, which is typical of airfoils that have a smaller leading edge radius. Once a LSB forms due to the adverse pressure gradient on the upper surface, increasing the angle of attack will move it further forward on the airfoil, and eventually

it approaches the suction peak. The adverse pressure gradient continues to develop and, when strong enough, prohibits the flow from reattaching as a turbulent boundary layer and the flow will be separated from the leading edge to the trailing edge. Effectively, the bubble has "burst" and reattachment no longer exists. This type of stall is common on thinner airfoils which have a relatively high $C_{L_{MAX}}$ and is generally much more abrupt than trailing edge stall [25].

2.6.3 Thin Airfoil Stall

Thin airfoils may exhibit another type known as "thin airfoil stall." These thin airfoils have a relatively low value of $C_{L_{MAX}}$ due to the formation of a long laminar separation bubble. Similar to airfoils that exhibit leading edge stall, thin airfoils have a high adverse pressure gradient near the leading edge, causing the flow to separate at low angles of attack. The point of reattachment of the turbulent boundary layer moves aft as the angle of attack is increased, lengthening the laminar separation bubble and flattening the lift-curve slope. The airfoil stalls when the turbulent boundary layer fails to reattach, decreasing the lift while increasing the drag and nose-down pitching moment. For thin airfoil stall, these trends are generally more shallow than other types of stall [25].

2.7 Mach Number Effects

Due to the low speed environment in which MAVs operate, airfoil performance will be slightly improved compared to larger rotary-wing vehicles because the flow is

nearly incompressible. Airfoils achieve a higher $C_{L_{MAX}}$ and exhibit a more shallow lift-curve slope at low Mach numbers. The lift-curve slope can be approximated at higher Mach numbers by the Glauert approximation:

$$C_{l_\alpha} = \frac{2\pi}{\sqrt{1 - M_\infty^2}} \tag{2.21}$$

The low Mach number will further delay the break in pitching moment to higher angles of attack, effectively delaying stall (due to the lack of compressibility effects). Low Mach number flow also generally has a higher suction peak closer to the leading edge than higher Mach number flow [25].

2.8 3-D Effects

Several flow phenomena exist in 3-D flow that are not present in 2-D flows. Experimentally, all flows are 3-D. To make measurements "2-D," endplates are placed on both ends of the wing, effectively making an infinite wing and eliminating tip vortices. However, true 2-D flow is never really achieved, in part due to "corner flow," where flow interacts with the endplates, and may lead to higher drag measurements. Experimentalists can give reasonable 2-D results by averaging several span-wise measurements through data reduction.

Chief among the effects of a 3-D finite wing (without endplates) is the formation of a tip vortex on the upper surface at the wing tip (assuming positive lift). A vortex forms as a result of the high pressure on the lower surface of the wing mixing with the low pressure flow on the upper surface at the wing tip. The vortex begins to form near the quarter-chord and continues to gain strength over the chord to

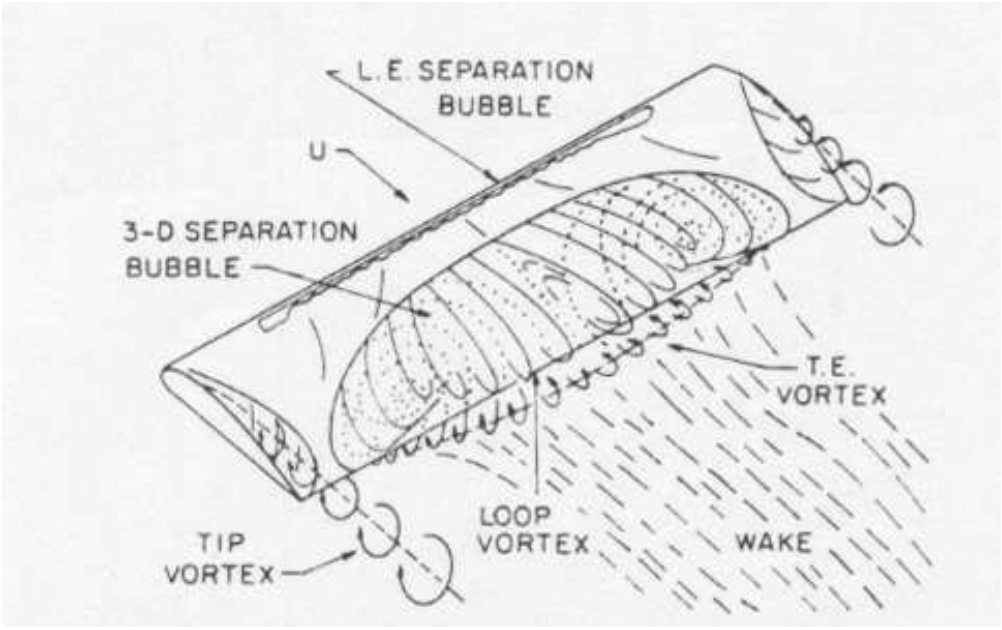

Figure 2.7: Qualitative flowfield at low Reynolds numbers, from Bastedo [13]

the trailing edge where it leaves the wing and continues to evolve in the wake. In the specific case of a hovering rotor, the vortex will contract along the slipstream boundary of the wake.

The velocity induced by the tip vortex effectively reduces the local angle of attack in the tip region, making it less susceptible to turbulent flow separation near the trailing edge. At inboard sections, the tip vortex has little effect and the airfoil characteristics are similar to 2-D results. However, for moderate aspect ratio wings, the outboard 20% experiences strong spanwise flow due to the induced velocity of the tip vortex [13]. Figure 2.7 shows a good qualitative flow field description for a rectangular wing at low Reynolds number.

Additionally, the tip vortex affects the span-wise lift distribution through the change in pressure at the tip. A tip vortex induces a spanwise pressure difference

that may result in loss of lift near the tip. Over the rest of the blade, the suction pressure at the leading edge increases from the root to about 3/4 span and then begins to taper off due to the formation of the tip vortex. The momentum theory lift distribution for an untwisted rectangular blade gives the point of maximum lift at mid-span and gradually decreasing until 3/4 span, at which point the lift decreases sharply due to the tip vortex [4, 25].

2.8.1 Hover Effects

A hovering rotor will induce inflow over the blade in addition to the free-stream velocity. The local induced inflow increases with radial position and reaches a maximum at the tip for an untwisted rotor [27]. The local lift and thrust also increase radially and decrease dramatically at the tip because of a loss in suction pressure due to the tip vortex. Induced drag is generally much higher than profile drag in a hovering rotor though there may be a significant contribution from the profile drag at low Reynolds number.

Additionally, a hovering rotor has a contracting wake that will affect the movement of the tip vortex after it is shed from the blade. The tip vortex contracts with the rotor wake at the slipstream boundary. Momentum theory gives this final contraction ratio as $\frac{\sqrt{2}}{2}$. The basic flow physics involved in a hovering rotor are illustrated in Figure 2.8.

Hover performance is measured as the figure of merit, which is defined as the ratio of ideal power to actual power. Ideal power has no viscous effects, and so profile

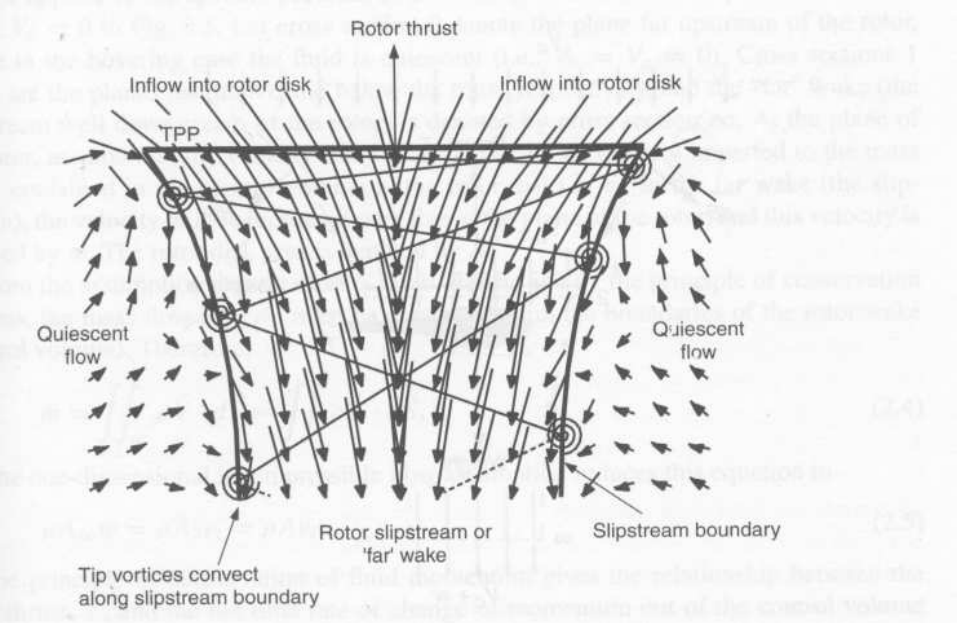

Figure 2.8: Flow near a hovering rotor, from Leishman [27]

drag due to low Reynolds number leads to a relatively low FM. At low Reynolds numbers, it may not be possible to treat induced and viscous effects independently due to the thick boundary layers and high skin friction drag. However, in the absence of a low Reynolds number-specific FM calculation, the traditional equation (5.5) is used with κ as the induced power coefficient and C_{d_0} as the zero lift drag coefficient:

$$FM = \frac{C_{P_{IDEAL}}}{C_{P_{INDUCED}} + C_{P_{PROFILE}}} \tag{2.22}$$

$$FM = \frac{\frac{C_T^{3/2}}{\sqrt{2}}}{\frac{\kappa C_T^{3/2}}{\sqrt{2}} + \frac{\sigma C_{d_0}}{8}} \tag{2.23}$$

Rotors operating at low Reynolds numbers generally have higher profile drag than full-size helicopters due to thicker boundary layers which may give a high C_{d_0}. Additionally, MAV rotors use blades with high solidity to have achieve a higher

Reynolds number although this may increase profile power. Solidity is defined as:

$$\sigma = \frac{N_b c}{\pi R} \tag{2.24}$$

2.9 Geometric Effects

MAV blades are designed with specific consideration to thickness, camber, and aspect ratio to maximize performance. This is necessary because rotor aerodynamic performance is a limiting factor in MAV development. Aerodynamic performance is inherently poor at low Reynolds number and has been discussed in conjunction with low aspect ratio wings in Sections 2.5 and 2.1. Aerodynamicists have examined insects and birds (flying in the low Reynolds number regime) and found that their wings are generally thin and cambered, giving good insight into the design of MAV wings and blades.

2.9.1 Blade Thickness

Airfoil thickness is defined non-dimensionally as t/c. Most MAV blades have high solidity and therefore have a low t/c (about 3%) compared to full-size helicopters, which are thick at the root (can be as much as 20%) and thin in the transonic region at the tip. MAV airfoils are thin because thinner airfoils perform better than thicker airfoils in the lower Reynolds number regime [1, 5, 8] by promoting short laminar separation bubbles. Additionally, some thin airfoils may stall with a leading edge stall type rather than a thin airfoil stall type if the turbulent boundary layer remains attached at moderately high angles of attack. An additional

consideration is to keep MAV blades light to keep the total rotor hub weight low.

2.9.2 Camber

To maximize the amount of lift produced by the blades, camber has historically been used in MAV airfoils up to 8%. Camber increases lift at a given angle of attack while also marginally increasing drag and (nose-down) pitching moment. A cambered airfoil will produce lift at moderate negative angle of attack. Ref. [1] suggests that the lift-curve slope is more nonlinear for cambered airfoils than for flat plates. Camber is often greatest at mid-chord because many MAV airfoils are designed as circular arcs, as this shape has shown good performance in experimental studies [1, 8, 11]. Generally, a strong pressure gradient may form on the upper surface as the flow expands around the curved nose, making the flow more apt to separate near the leading edge. This may be beneficial to trip the boundary layer if the turbulent boundary layer is able to reattach.

2.10 Summary

It can be seen from this chapter that several flow features in the low Reynolds number flight regime have a negative impact on airfoil performance. Low Reynolds number flow over low aspect ratio blades generally have a shallower lift-curve slope and lower $C_{L_{MAX}}$ than higher Reynolds number flow over higher aspect ratio wings. It is suggested that selecting an airfoil that promotes a short laminar separation bubble may increase performance, although care must be taken to ensure that the

bubble does not elongate and degrade performance. It is therefore beneficial to computationally investigate the flow physics to gain more insight into the problem.

Chapter 3

Methodology

Computational Fluid Dynamics (CFD) is a valuable tool with the ability to investigate fluid flow for MAV airfoils, wings, and rotors. In this work, as in all CFD approaches, the first step is to generate an appropriate mesh system that accurately resolves the geometry and flow features of interest. The second step is to choose the appropriate governing equations for the flow field points as well as the boundary conditions on the aerodynamic surfaces and in the far-field. Finally, the actual flow solvers are chosen to efficiently and accurately solve the governing equations. Since a large number of cases are examined, a scripting language with a Graphical User Interface (GUI) is used to minimize mistakes and increase the efficiency of the CFD practitioner.

3.1 Mesh System

In this thesis, solving for the viscous flow about MAV airfoils, wings, and rotors is accomplished using body-fitted structured curvilinear meshes (overset meshes for rotors). The individual grids are generated using either a hyperbolic or an algebraic grid generator.

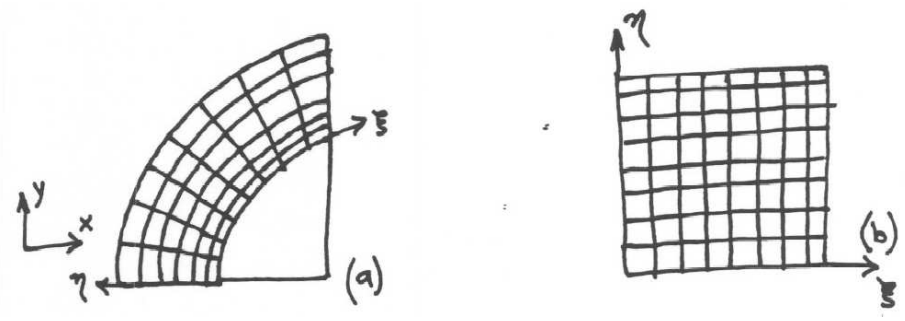

Figure 3.1: Curvilinear Coordinate Transformation from Holst [28]

3.1.1 Grid Generation Techniques

An airfoil surface is modeled as a viscous, adiabatic wall and the surface is discretized into a number of points. For the blade mesh, planes normal to the surface are extruded based on a hyperbolic grid generation scheme to ensure good cell sizing and good resolution at the airfoil surface. However, this mesh system is in "physical space" whereas the governing equations must be solved in the "computational space." The physical space consists of curvilinear coordinates which can be thought of as Cartesian coordinates when "unwrapped" from the airfoil as in Figure 3.1. A simple one-to-one mapping is possible to account for the stretching factors used in the physical space. Thus, it is computationally inexpensive to transform between coordinate systems and accuracy is maintained during this process.

A hyperbolic grid generator is a powerful tool to create grids normal to the airfoil surface while allowing for the flexibility of clustering at aerodynamically interesting points; in low Reynolds number flow, these are generally the leading edge and trailing edge. It is possible to specify the cell size or distance for the grid and initial surface data with this type of grid generation. The computational time to

create the largest C-type grid used in this thesis, with 9×10^5 points, is less than 10 seconds and, therefore, trivial. A representative 2-D C-type mesh is shown in Figure 3.2. The mesh system is clustered with fine wall spacing and is nearly orthogonal to the wall to accurately resolve the expected boundary layer flow.

For the 3-D cases, an additional grid meshing program is used to collapse the mesh at the tip, giving good resolution for solving the region where the tip vortex will form, as can be seen in Figure 3.3. This meshing program is algebraic in nature. Algebraic grids are much simpler to create and are generated even faster than hyperbolic grids.

A final background mesh was created for the hover 3-D cases using an additional algebraic grid generator. Though algebraic grids are not guaranteed to generate orthogonal cells, they are still useful in creating coarser background meshes that solve the flow in the blade wake. Additionally, it is possible to define the spacing, as can be seen in Figure 3.4.

3.1.2 Overset Mesh Technique

Overset meshes are used in the 3-D hover cases to efficiently calculate the solution over the rotor disk. The Navier–Stokes equations are solved on both grids. The near body mesh is fairly fine at the wing surface to capture viscous effects occurring in the boundary layer. It is not computationally efficient to maintain this level of mesh spacing throughout the flowfield, and so a global, relatively coarse background mesh is generated that encompasses the entire blade region, as shown

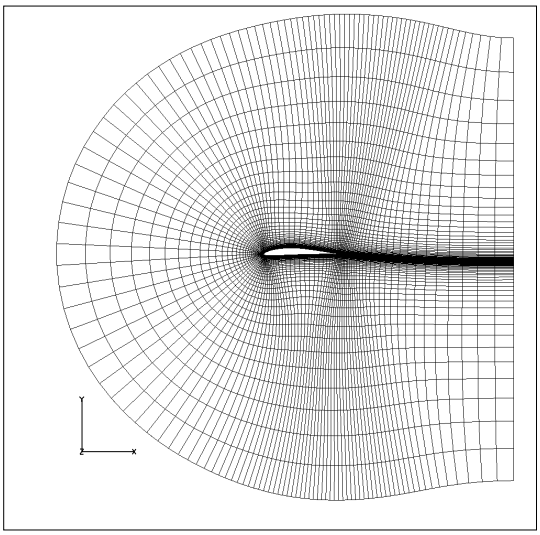

(a)

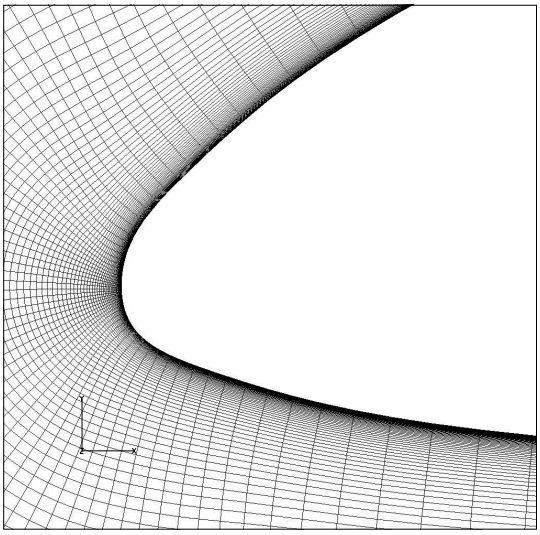

(b)

Figure 3.2: 2-D C-type Grid made with hyperbolic grid generator

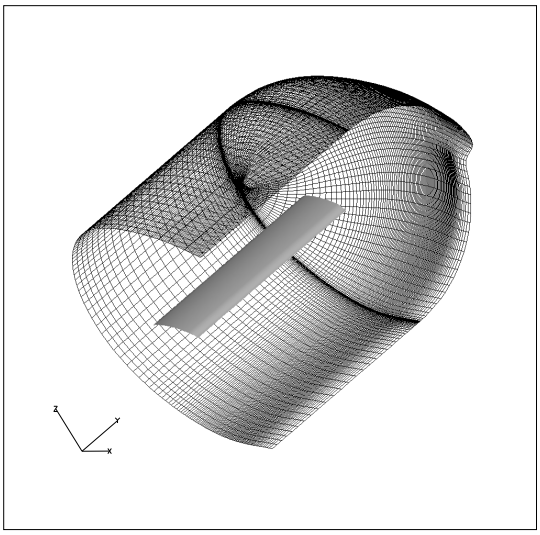

(a) C-O mesh

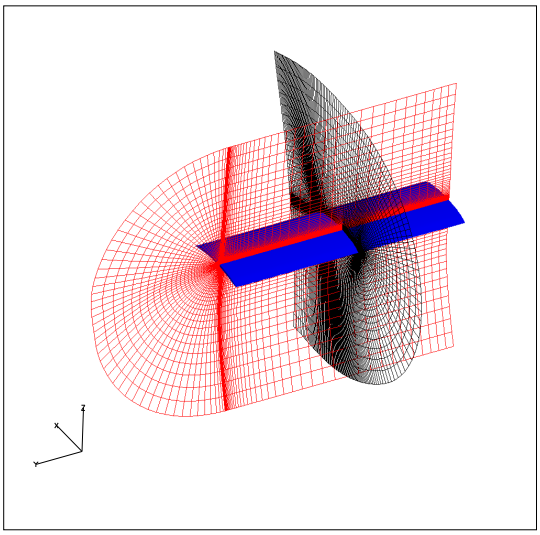

(b) C-O mesh (red) over a blade (blue).

C-type mesh used inboard (black)

Figure 3.3: A C-O grid topology created by algebraically collapsing 2-D airfoil sections at the tip

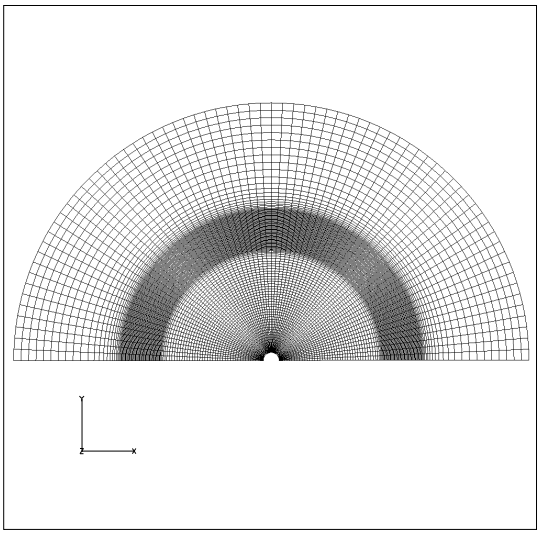

Figure 3.4: A single axial plane in background mesh models 1/2 the rotor disk. This mesh was created by an algebraic grid generator.

in Figure 3.5. Source terms are accounted for in a background mesh simulating the flow and transferred to the near-body mesh through a process called domain connectivity.

Domain connectivity is the general name for the process in which information is transferred between two overlapping meshes. A search is made for points which lie at the mesh interfaces in both grids. For each interface, one cell will give information (the "donor"), while a cell on the other mesh will receive information (the "receiver"). Interpolating between the donor and receiver cells allows information to be transferred. Care is taken to ensure good mesh resolution at the mesh interface; however, some regions are too fine in the blade mesh (near the tip) and hence some accuracy may be lost to keep the background mesh reasonably coarse. For this study, the computational quantities of interest are the lift, drag, and thrust, and

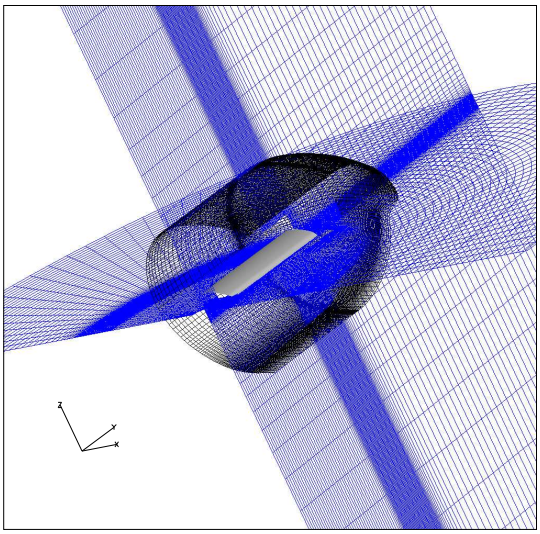

Figure 3.5: A blade mesh surrounded by a background mesh

so capturing intricate details of the vortex is not necessary. However, knowing the general path of the tip vortex allows for somewhat fine resolution in the background grid, and so capturing the vortex through one rotor revolution is possible. This way, the induced effects of the vortex on the blade can be captured without an excessive number of grid points. Beyond capturing this single blade-vortex interaction (BVI), fine wake spacing is not of primary interest, and so the background mesh is coarse in the far-field wake to save computational time.

Furthermore, to maintain consistency, a "hole" is cut in the background mesh where the blade mesh is located, as can be seen in Figure 3.6. The background mesh solution does not need to be computed inside the blade mesh because the information is transferred at the blade mesh boundary.

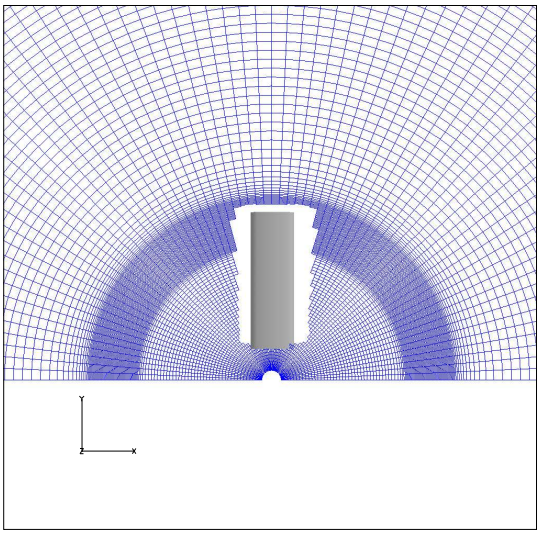

Figure 3.6: A hole cut in the background mesh

3.2 Governing Equations

It is necessary to solve the Navier–Stokes equations at each point in the mesh because viscous effects play an important role in low Reynolds number flow. A turbulence model must be used to obtain closure of the Reynolds Averaged Navier–Stokes (RANS) equations. To simulate the hover condition, source terms are utilized in the far-field boundary conditions.

3.2.1 Compressible Reynolds Averaged Navier–Stokes (RANS) Equations

Derived from Stokes' Theorem, the Navier–Stokes equations contain viscous terms in all directions in addition to compressibility terms. These equations conserve mass, momentum, and energy. Though rotary MAVs generally operate at

Mach numbers around 0.15, it may be possible for the local Mach number to reach 0.3 where compressibility may begin to have a non-negligible effect. Thus, the compressible flow terms are included in the Navier–Stokes equations to capture all the physical effects. Although this comes as additional computational expense, there was minimum development time because the flow solvers already have this capability. The 3-D compressible Navier–Stokes equations in Cartesian coordinates are given by:

$$\frac{\partial Q}{\partial t} + \frac{\partial E}{\partial x} + \frac{\partial F}{\partial y} + \frac{\partial G}{\partial z} = S \tag{3.1}$$

where Q is the state vector, E, F and G are the flux vectors, and S is the source term vector. These vectors are given below:

$$Q = \left\{ \begin{array}{c} \rho \\ \rho u \\ \rho v \\ \rho w \\ e \end{array} \right\} \tag{3.2}$$

$$E = \left\{ \begin{array}{c} \rho u \\ \rho u^2 + p - \tau_{xx} \\ \rho uv - \tau_{xy} \\ \rho uw - \tau_{xz} \\ uH - u\tau_{xx} - v\tau_{xy} - w\tau_{xz} + k\frac{\partial T}{\partial x} \end{array} \right\} \tag{3.3}$$

$$F = \begin{Bmatrix} \rho v \\ \rho uv - \tau_{xy} \\ \rho v^2 + p - \tau_{yy} \\ \rho uw - \tau_{yz} \\ vH - u\tau_{xy} - v\tau_{yy} - w\tau_{yz} + k\frac{\partial T}{\partial y} \end{Bmatrix} \tag{3.4}$$

$$G = \begin{Bmatrix} \rho w \\ \rho uw - \tau_{zx} \\ \rho vw - \tau_{zy} \\ \rho w^2 + p - \tau_{zz} \\ wH - u\tau_{xx} - v\tau_{xy} - w\tau_{xz} + k\frac{\partial T}{\partial z} \end{Bmatrix} \tag{3.5}$$

$$S = \begin{Bmatrix} 0 \\ f_x \\ f_y \\ f_z \\ uf_x + vf_y + wf_z \end{Bmatrix} \tag{3.6}$$

In these definitions, ρ is the density, (u, v, w) and (f_x, f_y, f_z) are the Cartesian velocity and body force components in the directions (x, y, z), respectively. In this thesis, the body forces are zero since they are captured and not modeled. The quantity e is the total energy per unit volume, τ_{ij} are the stress terms and H is the stagnation enthalpy per unit volume. The quantity k is the coefficient of thermal conductivity and T is the static temperature. The pressure is determined by the equation of state for a perfect gas given by:

$$p = (\gamma - 1)\left\{e - \frac{1}{2}\rho(u^2 + v^2 + w^2)\right\} \tag{3.7}$$

and the stagnation enthalpy is given by

$$H = e + p \tag{3.8}$$

where γ is the ratio of specific heats. The shear stress (τ_{xy}) is defined as :

$$\tau_{xy} = \left(\frac{\mu + \mu_t}{2})(\frac{\partial u}{\partial y} + \frac{\partial v}{\partial x}\right) \tag{3.9}$$

where μ is the laminar viscosity and μ_t is the turbulent viscosity. Laminar viscosity can be easily evaluated using Sutherland's Law [29]. However, turbulent viscosity must be evaluated using a turbulence model — see Section 3.2.2 for a discussion of turbulence models. Using the curvilinear coordinate transformation described earlier, it is possible to convert the physical form of the Navier–Stokes equations to a computational form on a uniformly spaced Cartesian system. Once the coordinates have been transformed, the Navier–Stokes equations are given by:

$$\frac{\partial \hat{Q}}{\partial \tau} + \frac{\partial \hat{E}}{\partial \xi} + \frac{\partial \hat{F}}{\partial \eta} + \frac{\partial \hat{G}}{\partial \zeta} = \hat{S} \qquad \text{in } \Omega \tag{3.10}$$

where the vector of conservative quantities $\hat{Q} = \frac{1}{J}Q$ and the flux contributions are now defined with respect to the computational cell faces (created from making a plane out of four adjacent points) by (J = determinant of Jacobian):

$$\hat{E} = \frac{1}{J}\left(\frac{\partial \xi}{\partial x}E + \frac{\partial \xi}{\partial y}F + \frac{\partial \xi}{\partial z}G\right) \tag{3.11}$$

$$\hat{F} = \frac{1}{J}\left(\frac{\partial \eta}{\partial x}E + \frac{\partial \eta}{\partial y}F + \frac{\partial \eta}{\partial z}G\right) \tag{3.12}$$

$$\hat{G} = \frac{1}{J}\left(\frac{\partial \zeta}{\partial x}E + \frac{\partial \zeta}{\partial y}F + \frac{\partial \zeta}{\partial z}G\right) \tag{3.13}$$

$$\hat{S} = \frac{1}{J}S \tag{3.14}$$

These partial differential equations are solved for the conservative variables, $\hat{Q}$, in the computational domain described earlier using the Transonic Unsteady Rotor Navier–Stokes (TURNS) code [30]. This code is a compressible Reynolds Averaged Navier–Stokes solver modified to include a low Mach preconditioner described in Section 3.3.2. Boundary conditions are specified according to the discussion in Section 3.2.3.

3.2.2 Turbulence Model

It is necessary to calculate the turbulent viscosity in addition to the conservative variables to obtain a complete solution. Various models have been developed in recent years to better represent the turbulent viscosity. As described in Ref. [31], linear eddy viscosity models range from zero equation algebraic turbulence models (Baldwin-Lomax, as in Ref. [32]), to four equation turbulence models ($v^2 - f$ model in Ref. [33]). The zero equation model developed by Baldwin and Lomax calculates the turbulent viscosity as an algebraic function of the conservative variables. On the other hand, $v^2 - f$ model by Durbin solves four differential equations to obtain four scalar field variables (k, ϵ, v^2 and f). The turbulent viscosity is obtained as an algebraic function of these four variables.

For this thesis, the one equation model of Spalart and Allmaras [34] is utilized to keep computational time low. The Spalart–Allmaras turbulence model has been

used with separated flows in Ref. [35]. This model is given by:

$$\frac{D\nu_t}{Dt} = c_{b1}S\nu_t + \frac{1}{\sigma}\left(\bigtriangledown.(\nu_t \bigtriangledown \nu_t + c_{b2}(\bigtriangledown\nu_t)^2)\right] - c_{w1}f_w[\frac{\nu_t}{d}\Big)^2 \tag{3.15}$$

where ν_t is the turbulent eddy viscosity, c_{b1}, c_{b2} and c_{w1} are constants, d is the distance from the wall and f_w is a function of distance from the wall. This differential equation is loosely coupled to the Navier–Stokes equations, and the additional field variable turbulent viscosity (ν_t) is obtained as a solution to be used in post-processing. The shear stress in the momentum and energy equations is evaluated once the turbulent viscosity is calculated and hence closure is achieved for all the variables in the Navier–Stokes equations. More details about the turbulence model can be found in the original work by Spalart and Allmaras [34].

3.2.3 Boundary Conditions

A viscous wall boundary condition is used over the airfoil/blade planes to ensure no slip at the walls. A wake-cut condition is used at the interface of the trailing edge of the airfoil in the wake as in Figure 3.7, where the information is averaged from the upper and lower surface.

Free-stream boundary conditions are used at all other boundaries in the blade mesh. For the hover case, the background mesh contains only $360/N_b$ degrees of the azimuth, where N_b = number of blades. For instance, a two-bladed rotor only needs half of the azimuth to be modeled due to aerodynamic symmetry in hover. A periodic boundary condition is therefore implemented at the azimuthal boundaries to model the effect of additional blades.

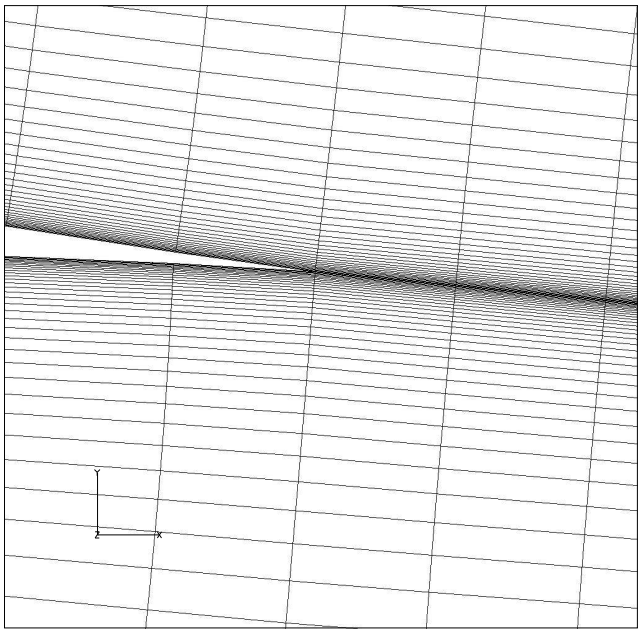

Figure 3.7: Wake cut boundary condition at trailing edge of airfoil

For a hovering rotor, the far-field boundary condition is modified to account for the far-field induced velocities. By prescribing an estimate of the total thrust (based on computational results), the inflow and wake contraction effects are modeled.

3.3 Flow Solvers

Low Mach number, low Reynolds number flow has been previously discussed to have several interesting flow properties that require special attention when computationally solving the Navier–Stokes equations. Due to the low-speed environment in which MAVs operate, it is beneficial to use implicit time marching in the flow solvers so as to be able to use larger timesteps than explicit methods. Additionally, a low Mach preconditioner is introduced with the benefit of reducing the stiffness and computational dissipation, yielding a more accurate solution and accelerating

convergence. Two flow solvers, OVERFLOW [36] and TURNS, take advantage of these methods and are introduced later in this section.

3.3.1 Implicit Time Marching

Implicit time marching methods have a key advantage over explicit methods, in that they do not have a numerical stability limit. Explicit methods, on the other hand, are limited as to the maximum timestep size. Because implicit methods have no stability limit, it is possible to obtain a converged solution much quicker than with an explicit method.

3.3.2 Preconditioning

Compressible Navier–Stokes flow solvers generally do not perform well in low Reynolds number and low Mach number flows with respect to convergence and accuracy. There are several benefits to using a low Mach preconditioner in the flow solver to help solve these problems [24]. Generally, there is a large difference between eigenvalues in low Mach number flows, making the solution computationally stiff, and increasing the time to reach the steady state solution. A preconditioner accelerates convergence to the steady state solution by bringing the magnitude of the acoustic eigenvalues closer to the convective eigenvalues (effectively reducing the stiffness).

Low Mach number flows may also have scaling inaccuracies where some dissipation terms may be too high while some dissipation terms may be too low. Pre-

conditioning removes these scaling inaccuracies by making the dissipation terms more consistent. The benefits are largest near the stagnation point and near surface boundary layers where inaccuracies may arise in the pressure terms relative to convective terms.

3.3.3 TURNS

The Transonic Unsteady Rotor Navier–Stokes (TURNS) code was developed at the University of Maryland [30] for use in rotor CFD calculations. It was modified to include a low-Mach preconditioner [24]. Furthermore, the fully implicit RANS solver includes the full viscous terms in all directions and includes the effects of turbulence using the model of Spalart–Allmaras. Though the flow may be laminar for a significant portion of the airfoil at low Reynolds numbers, transition phases exist where the flow becomes turbulent, particularly at high angles of attack where the flow is separated. Therefore, a turbulence model needs to be used to capture the laminar, transition, and turbulent boundary layer characteristics.

3.3.4 OVERFLOW

In addition to TURNS, the OVERFLOW 1.8s code primarily developed at NASA-Langley is also used. OVERFLOW is a structured compressible Navier–Stokes flow solver that utilizes overset meshes [36]. OVERFLOW is also implicit in time and third order in space. A multigrid option is used to speed convergence to steady state in some cases. For the current validation, the OVERFLOW solver has

been used with its low-Mach preconditioner (similar to that of TURNS) to further accelerate convergence. The Spalart–Allmaras turbulence model is used, and so one would expect OVERFLOW and TURNS to give similar results because they share a common methodology.

3.4 TCL/Tk Scripting

TCL/Tk is a scripting language with the ability to read and write data while also executing UNIX commands. Due to the large number of CFD cases necessary to validate experimental data, it was decided to write a graphical-user-interface (GUI) with TCL/Tk to efficiently run the grid generation and domain connectivity programs, and other basic utilities. This GUI was developed solely for the task of efficiently managing cases while reducing mistakes. A typical operation of generating a C-type mesh is shown in Figure 3.8.

3.5 Airfoil Geometries

Several airfoils are examined in this thesis, including the Eppler 387, an airfoil designed by Mueller, and an airfoil designed by Hein for use in MAV applications. The MAV airfoils are particularly thin, requiring special consideration for grid generation around the boundary layer. These airfoils exhibit different leading edge geometry, requiring particular attention paid to adequately resolving the stagnation point for each mesh system.

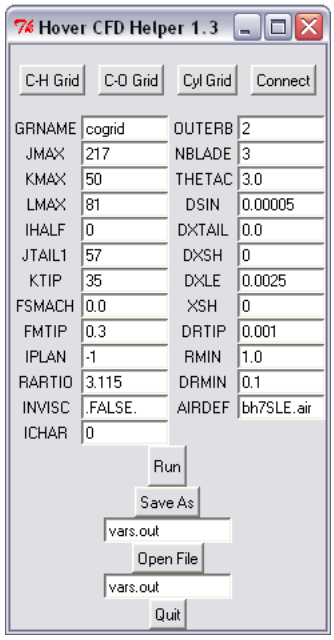

Figure 3.8: TCL Interface

3.5.1 Leading Edge and Trailing Edge Considerations

Computational considerations must be taken into account when validating airfoil geometry to ensure that the flow solver can converge to an accurate solution. The leading edge must be rounded to a certain degree for good resolution of the stagnation point. Sharpened leading edges or any sort of geometric discontinuity will induce flow separation over the airfoil; thus rounding these surfaces computationally will give a more accurate comparison to experimental data due to the nature of structured meshes, which are orthonormal to the airfoil surface. Several leading edge geometries have been examined in this body of research, including an elliptical leading edge [1] and a sharpened leading edge [11]. The effect of slightly rounding the surfaces should not be too large with respect to lift and drag calculations.

Mueller [1] suggests that trailing edge geometry has little effect in lift and drag measurements at low Reynolds number. Tested geometries in Ref. [1] include an elliptical trailing edge and a linearly-tapered trailing edge. Differences were slightly apparent only in pitching moment measurements. This allows for slightly altering the trailing edge geometry without losing accuracy in lift and drag results, because grid generators must close the airfoil trailing edge for the wake cut boundary condition.

3.5.2 Eppler 387

The Eppler 387 airfoil is chosen for a 2-D validation due to its common use in low Reynolds number flow. This airfoil is about 9% thick with 3.87% camber. Though thicker than most MAV airfoils, the Eppler 387 validation shows the usefulness of the flow solver and gives insight into low Reynolds number flow physics. The airfoil geometry was taken from Ref. [10] and is shown in Figure 3.9. Validations were run with the TURNS flow solver.

3.5.3 Mueller

The TURNS and OVERFLOW flow solvers are used to validate data from Mueller [1]. The airfoil used is a circular arc with 5% camber and 1.93% thickness and can be seen in Figure 3.10. This airfoil is indicative of those generally used by MAVs with its characteristic thin shape and camber. Mueller also presents 3-D results for the same airfoil with a semi-span aspect ratio of 3, and these results are

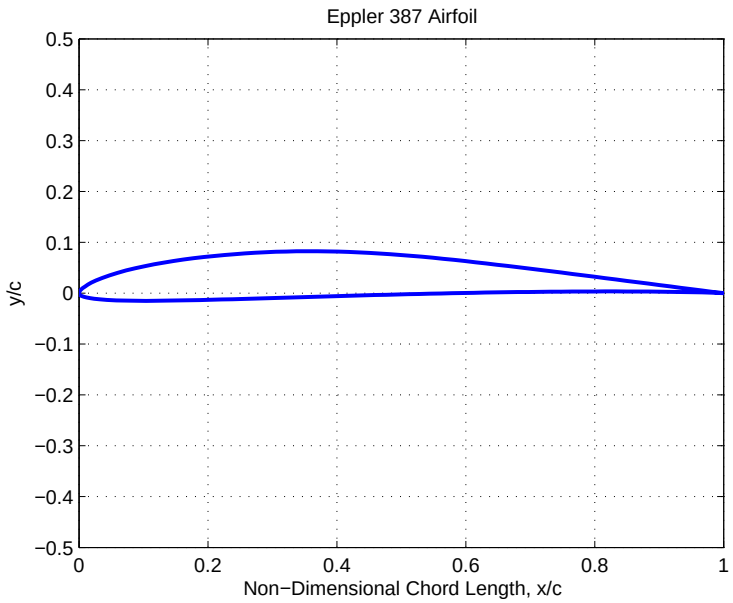

Figure 3.9: Eppler 387 Airfoil

also validated in Chapter 4.

3.5.4 Hein

The recent work of Hein [11] is examined because it has a similar geometry to the Mueller wing, and Hein tested the airfoil in a 2-bladed hover model. Additionally, the data is readily available. The rotor blades are 2.75% thick with 7% camber as can be seen in Figure 3.11. The 3-D blade has an 18% root cutout and an aspect ratio of 3.81. Of the geometries examined in [11], the sharpened leading edge blade was chosen because it gave the highest FM. The trailing edge geometry was modified from a square plate to include a small amount of taper to close the trailing edge. This was determined to have a only a slight effect on the lift, drag, and thrust calculations as discussed in Section 3.5.1.

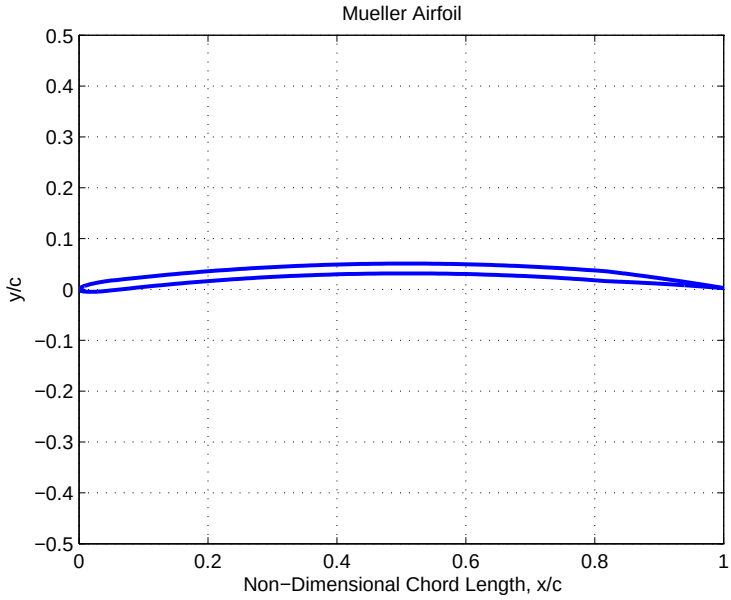

Figure 3.10: Mueller Airfoil

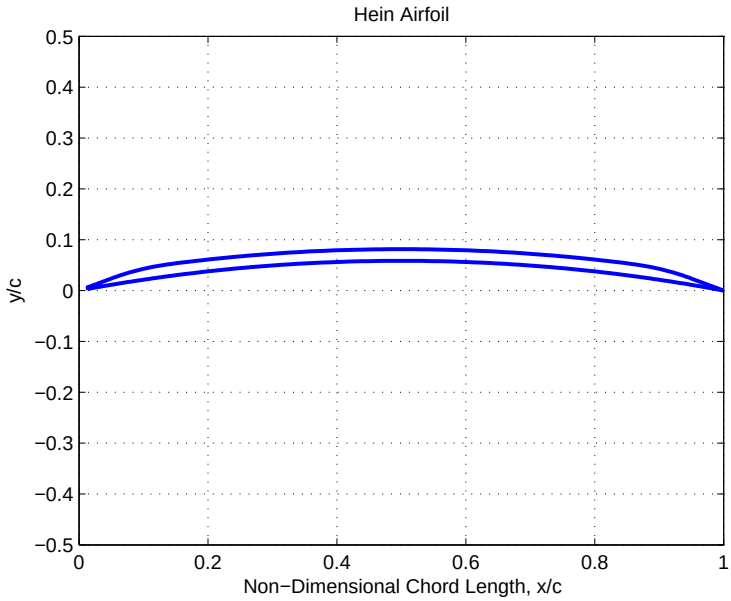

Figure 3.11: Hein Airfoil

Chapter 4

Results for Static Cases

4.1 2-D Results: Eppler 387 Airfoil

4.1.1 The Experiment

The data used in the Eppler 387 validation was found in Ref. [10], and the experimental procedure is documented further in Ref. [5]. The UIUC low-speed subsonic wind tunnel was used, which has a low turbulence intensity ($< 0.1\%$) for low Reynolds number tests. The particular experiment validated in this thesis used a 6-inch model rather than a 12-inch model common to the majority of the airfoil data taken from the UIUC low-speed subsonic wind tunnel. The Reynolds number was 60,000 and the Mach number was 0.017. The lift and moment measurements were made using a force balance while the drag measurements used the momentum deficiency method, with the measurements made at 1.25 chords behind the airfoil trailing edge. The experimental data was taken by increasing the angle of attack, and there was no experimental pressure data.

4.1.2 Validation

The results of the Eppler 2-D airfoil lift, moment, and drag validation are presented in Figure 4.1. This airfoil stalls around 13 degrees angle of attack in

these flow conditions. From the lift validation in Figure 4.1(a), it can be seen that the TURNS flow solver predicts a smoother lift curve slope than was measured in the experiment. TURNS gives a good quantitative prediction of stall and the non-linear lift curve slope region above 10° degrees angle of attack. The experimental data has a slightly steeper lift-curve slope though there is a "dip" around $\alpha = 6°$ that may result from the formation and movement of the laminar separation bubble. This can also be seen as an increase in nose-down pitching moment drag, and is fairly typical of low Reynolds number flows.

For the moment validation in Figure 4.1(b), TURNS again predicts a smoother curve than the experiment which had significant variation in measured data. The pitching moment also increases through the moderate angle of attack range as the laminar separation bubble (LSB) moves forward on the airfoil surface. Stall is qualitatively well predicted at higher angles of attack. This includes a small nose up pitching moment before the drastic nose-down moment around 13 degrees angle of attack where the flow is separated. Though the TURNS solutions are quantitatively different than those in the experiment, the computational solutions agree reasonably well with 2-D airfoil theory.

Finally, the drag validation is in Figure 4.1(c). Both the experimental data and the flow solver predict $C_{d_0} = 0.02$ at around $\alpha = -2°$, which is about twice the C_{d_0} commonly found on airfoils used on full-size helicopters. The experimental data contains a small "hump" around $\alpha = 6°$ that is not in a traditional "drag bucket" commonly found in 2-D airfoil data but may be the result of a laminar separation bubble forming on the upper surface. TURNS predicts a significant increase in drag

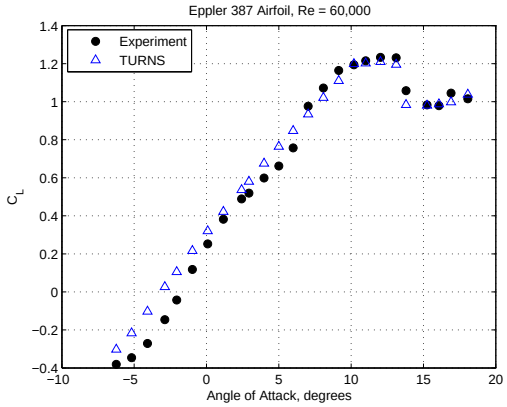

(a) Lift Validation

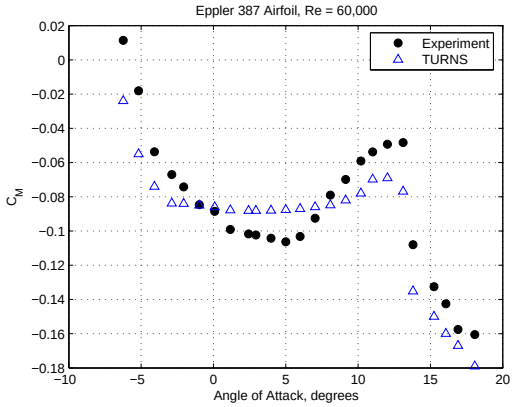

(b) Moment Validation

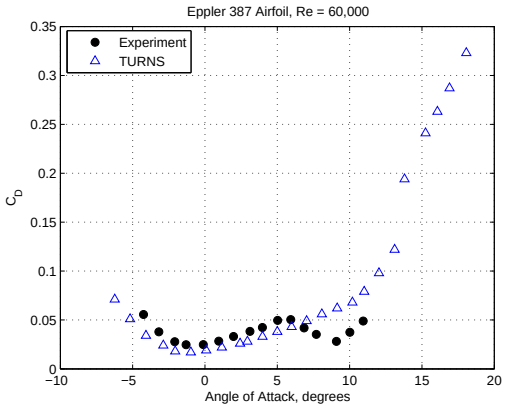

(c) Drag Validation

Figure 4.1: Eppler 387 2-D Results

in the stalled flow regime, as expected. There was no experimental data available for high angles of attack because of the possibility of decreased accuracy in the measurements as the flow may have more 3-D effects with a large region of separated flow.

4.1.3 Velocity Vectors

Figure 4.2 shows the velocity vector field around the Eppler 387 airfoil predicted by the TURNS code. For the $\alpha = 5.99^\circ$ case in Figure 4.2(a), there is a small amount of flow separation on the upper surface near mid-chord aft of the point of maximum thickness, where the flow usually tends to separate. This is possibly the point of laminar separation and transition to a turbulent boundary layer because the flow is attached aft to the trailing edge. As the angle of attack increases to $\alpha = 11.01^\circ$ in Figure 4.2(b), the point of laminar separation has effectively moved forward to form a small laminar separation bubble on the upper surface near the leading edge. The flow reattaches as a turbulent boundary layer. It remains attached over the rest of the airfoil because the turbulent boundary layer is thicker and does not separate as easily as a laminar boundary layer. However, the flow appears to separate at the trailing edge of the airfoil with increasing angle of attack (the boundary layer is thicker towards the trailing edge). Trailing edge stall, as discussed previously, is characteristic of relatively thicker airfoils, and one would expect to see some amount of flow separation at the trailing edge of the airfoil, particularly at high angles of attack.

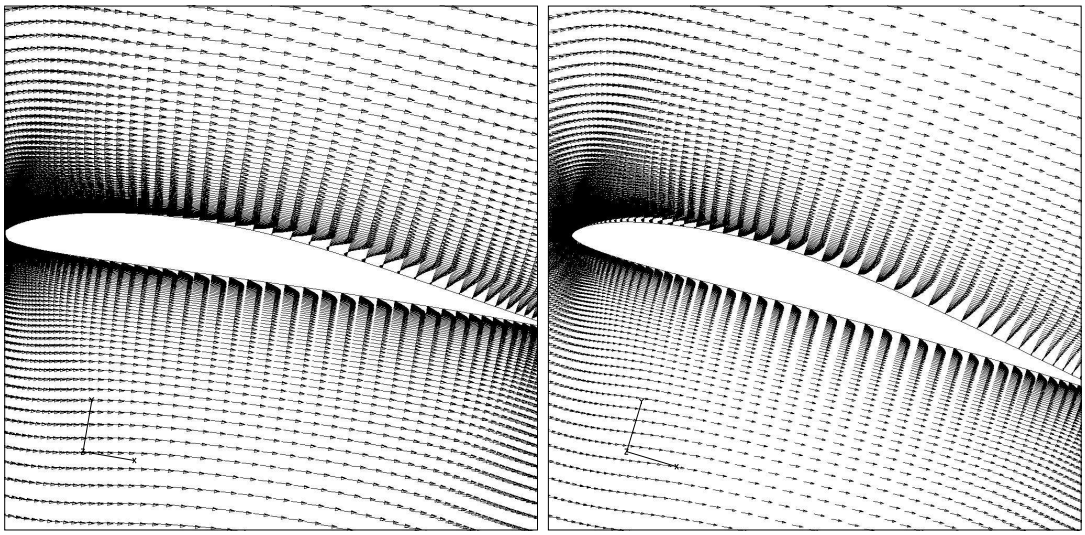

(a) $\alpha = 5.99$ (b) $\alpha = 11.01$

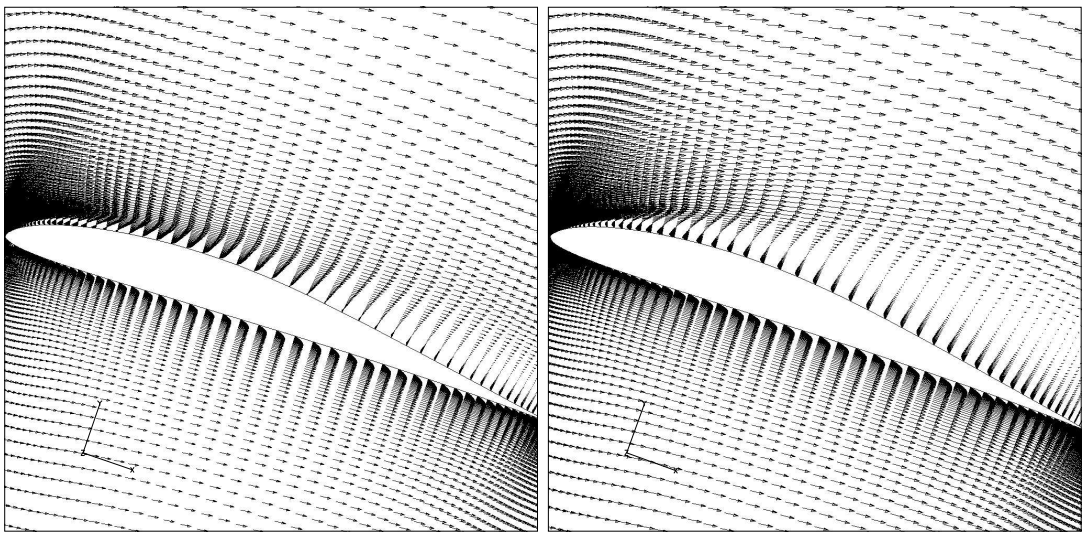

(c) $\alpha = 13.11$ (d) $\alpha = 13.80$

Figure 4.2: Eppler 387 Velocity Vectors

In fact, the flow does separate at the trailing edge with a moderate increase in angle of attack (to $\alpha = 13.11°$) as shown in the computations in Figure 4.2(c). The LSB still exists at the leading edge of the airfoil although it appears as if the flow recirculation within the bubble has intensified and moved further forward. A final increase in angle of attack to $\alpha = 13.80°$ in Figure 4.2(d) shows that the LSB has effectively "burst" as the trailing edge and leading edge separation regions have merged, and the flow is completely separated over the entire upper surface of the airfoil. A significant amount of flow recirculation exists above the airfoil and beyond the trailing edge. The airfoil has stalled at this angle of attack, drastically reducing the lift while increasing the nose-down pitching moment and the drag over the airfoil. It is noteworthy that the angle of attack increased only 0.69° and yet the TURNS code was able to capture stall at the same angle of attack as in the experiment. This is the same point at which the integrated lift drops, the negative pitching moment increases, and the drag increases dramatically as seen in Figure 4.1.

4.1.4 Skin Friction Coefficient

The point of flow separation can readily be seen where the skin friction coefficient changes sign, as in Figure 4.3. From this figure, it can be seen that the flow separates at $x/c = 0.45$ at $\alpha = 2.93°$. The point of laminar separation moves forward as the angle of attack is increased to $\alpha = 5.99°$. Increasing the angle of attack to the point just before stall, at $\alpha = 13.11°$, the laminar separation point has

moved to the leading edge. The laminar separation bubble covers 20% of the airfoil near the leading edge at this angle of attack, which also has turbulent separation over the trailing edge. The airfoil stalls after increasing the angle of attack further to $\alpha = 13.80°$, as the skin friction coefficient is negative over the entire airfoil.

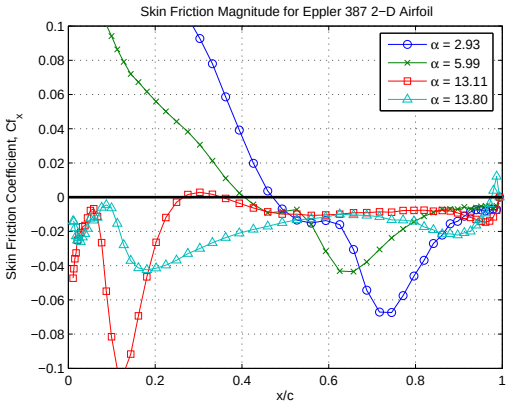

Figure 4.3: Skin Friction Coefficient over Eppler 387 2-D airfoil

4.1.5 Pressure Contours

To further analyze airfoil stall, the pressure distribution over the airfoil is examined over a range of angle of attack. In the pre-stall regime in Figure 4.4(a), the $\alpha = 5.99°$ case has a relatively flat pressure contour on the upper surface, with the small rise in negative pressure around mid-chord resulting from the small region of flow separation from the airfoil surface. As the angle of attack increases to $\alpha = 11.01°$, a laminar separation bubble has formed on the upper surface, indicated by the region of constant pressure near the leading edge. The stagnation pressure is relatively high at the leading edge. For this angle of attack, the relatively shallow

pressure gradient over the rest of the upper surface of the airfoil is not strong enough to separate the turbulent boundary layer aft of the separation bubble. However, as the angle of attack is increased further to $\alpha = 13.11°$, the adverse pressure gradient strengthens, indicating that the airfoil will stall upon subsequent increase in angle of attack. There is more flow separation at the trailing edge of the airfoil, as indicated by a nearly constant pressure on the upper surface. The flow over the lower surface of the airfoil is relatively unchanged between $\alpha = 11.01°$ and $\alpha = 13.11°$.

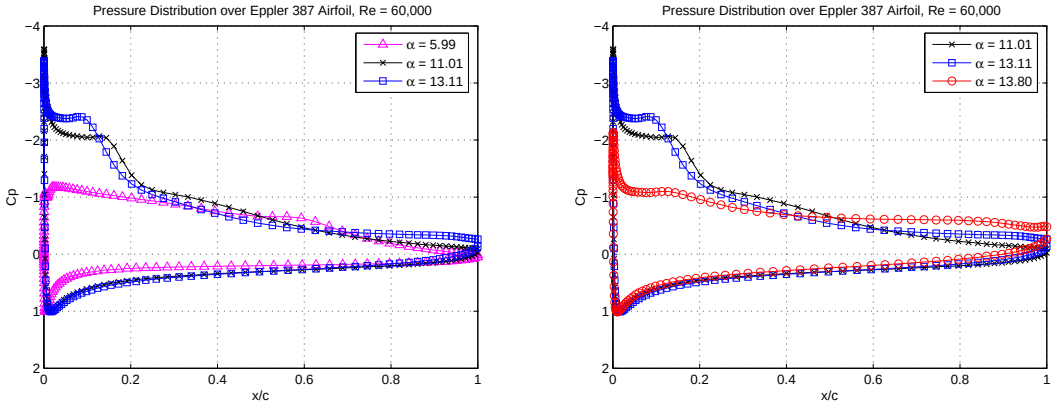

(a) Pre-Stall Regime

(b) Stall Reached

Figure 4.4: Pressure distribution

Examining the post-stall regime in Figure 4.4(b), with the addition of the $\alpha = 13.80°$ case, it can be seen that the decrease in negative pressure is an indication of stall at this angle of attack. The suction pressure is greatly reduced at the leading edge. Effectively, the LSB has burst and the flow separation from the trailing edge has merged with the LSB near the leading edge. The flow over the entire upper surface of the airfoil is separated, resulting in a relatively flat pressure contour.

	ν_t/ν
$\alpha = 2.93°$	26.711
$\alpha = 5.99°$	34.478
$\alpha = 11.01°$	55.965
$\alpha = 13.11°$	140.924
$\alpha = 13.80°$	363.414

Table 4.1: Eppler 387 Turbulent Viscosity Levels, ν_t

Additionally, the $\alpha = 13.80°$ distribution has a significant gap between the lower and upper surface pressures at the trailing edge, further indicating the flow is fully separated at this angle of attack.

4.1.6 Eddy Viscosity

The eddy viscosity is defined as the ratio of the turbulent viscosity to the laminar viscosity:

$$\frac{\nu_t}{\nu} = \frac{\tilde{\nu}^3}{\tilde{\nu}^3 + 7.1^3} \tag{4.1}$$

where ν is the laminar viscosity, ν_t is the turbulent viscosity, and $\tilde{\nu}$ is the working variable from the flow solver. Table 4.1 shows how the variables change with angle of attack.

The predicted eddy viscosity contours are plotted in Figure 4.6 for the Eppler 387 airfoil. One can expect to see low turbulence levels at shallow angle of attack where the flow will be primarily laminar. Examining $\alpha = 2.93°$ in Figure 4.5, it can

be seen that low levels of eddy viscosity exist only in the wake region because the flow over the airfoil is laminar. By increasing the angle of attack to $\alpha = 5.99°$ in Figure 4.6(a), the turbulence begins to move forward on the airfoil to mid-chord. This is the location of modest flow separation, as discussed with Figure 4.2(a). The low quantity of turbulence on the upper surface near the leading edge signifies that the boundary layer is still attached and laminar, while after the point of flow separation, the boundary layer reattaches as a turbulent layer. As the angle of attack increases to $\alpha = 11.01°$ in Figure 4.6(b), the LSB discussed in Figure 4.2(b) causes the flow to be turbulent over the airfoil aft of the reattachment point. Increasing the angle of attack further to $\alpha = 13.11°$, the point just before stall, causes the boundary layer to thicken considerably as can be seen in Figure 4.6(c). Notice, however, that the turbulence does not extend too far in the normal direction. Once stall is reached in Figure 4.6(d), the turbulent viscosity is much stronger and thicker over the complete airfoil as massive separation occurs.

As discussed in section 3.2.2, the Spalart–Allmaras turbulence model was used to assume turbulent flow over the entire airfoil though in reality there may be regions of laminar flow and transition to turbulent flow. It may be possible, therefore, that the flow solver assumes a thicker boundary layer and resultingly a higher viscous drag at low angles of attack which may not occur in the experiment. Although the Spalart-Allmaras model is not specifically designed for low Reynolds number flows and no transition model is used in the calculations, the calculated eddy viscosity values are not completely unreasonable since very small values are predicted in the leading edge region where laminar flow is expected at low angles of attack.

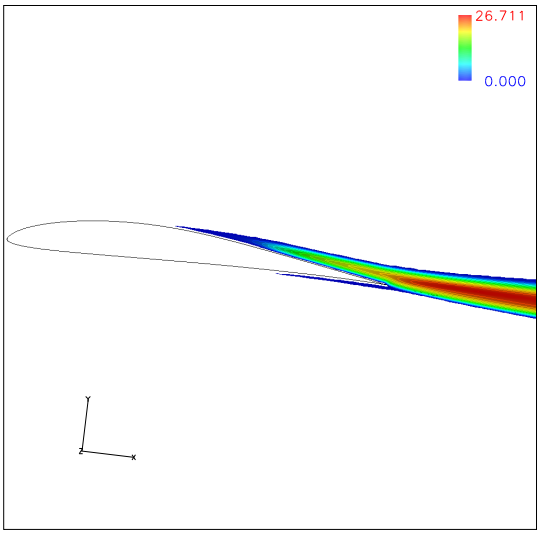

Figure 4.5: Eddy viscosity ratio over Eppler 387 airfoil at $\alpha = 2.93°$

4.1.7 Low-Mach Preconditioner Results

The Eppler 387 airfoil was run at 4, 8, and 12 degrees angle of attack without the low Mach number preconditioner, at the same Reynolds number of 60,000 and Mach number of 0.017. None of the cases came close to converging after 16,000 iterations. The timestep had to be reduced two orders of magnitude for the flow solver to even run. Thus the low Mach preconditioner must be used for this airfoil. The low Mach preconditioner is investigated for thinner airfoils in Section 4.2.7.

4.1.8 Summary

The TURNS code gives reasonable agreement for C_L, C_M, and C_D and excellent qualitative and quantitative prediction of stall. An investigation of the flow physics has shown the formation of the LSB, the stall mechanism, and the validity of several assumptions that aid in convergence speed and accuracy. Though the Eppler

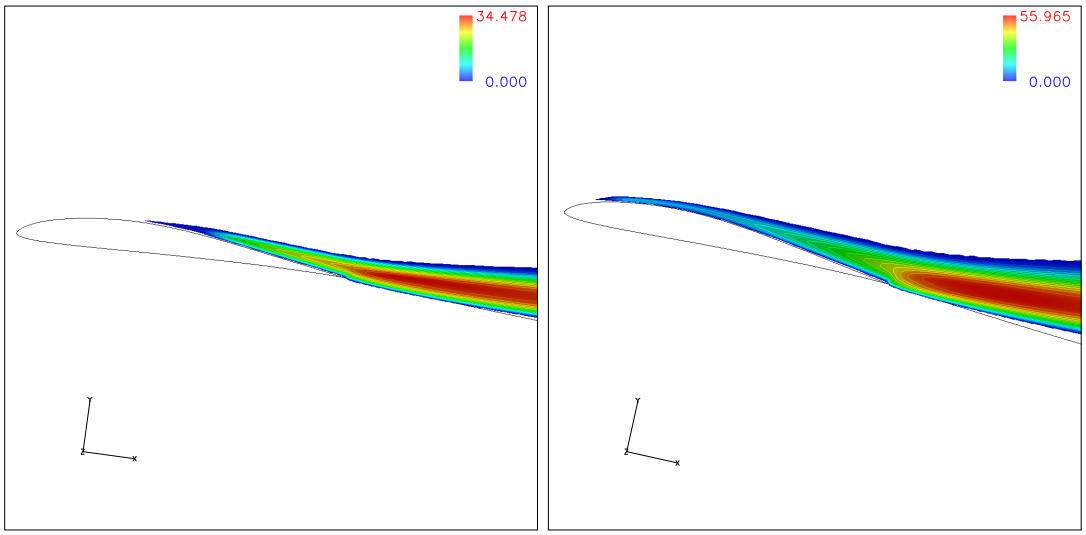

(a) $\alpha = 5.99°$ (b) $\alpha = 11.01°$

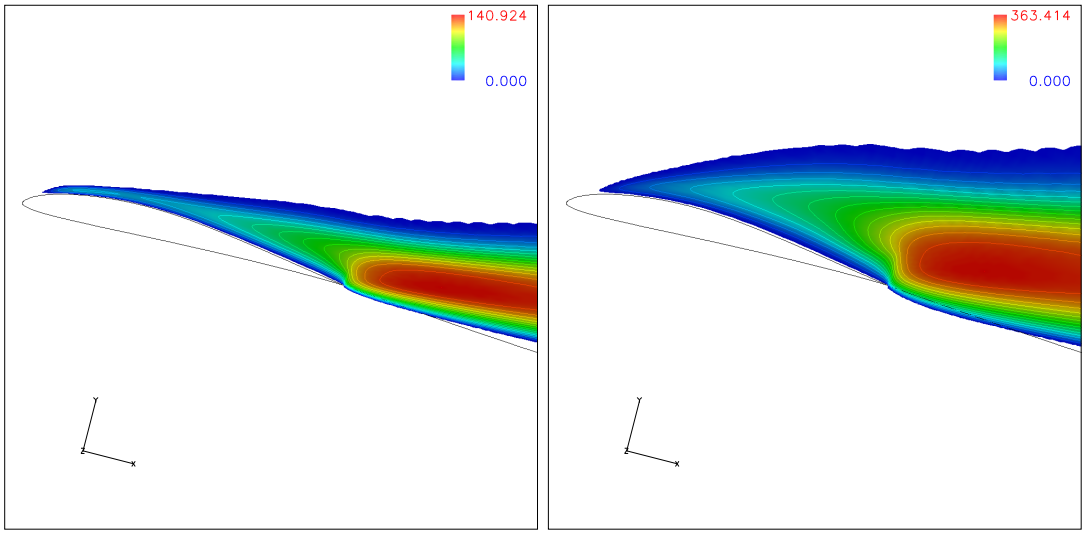

(c) $\alpha = 13.11°$ (d) $\alpha = 13.80°$

Figure 4.6: Eppler 387 Eddy viscosity ratio

387 airfoil is thicker than most MAV airfoils, this validation gives good insight into low Reynolds number flow.

4.2 2-D Results: Mueller Airfoil

4.2.1 The Experiment

The experiment, described in Ref. [1], was conducted in a water tunnel at the Hessert Center for Aerospace Research at the University of Notre Dame. The Reynolds number was 60,000, which leads to a Mach number of 0.016 in air. The airfoil model was 12 inches long with endplates on both sides to simulate 2-D flow. Again, adequately low turbulence levels were measured in the tunnel for these low Reynolds number measurements. The lift and drag were both measured from a force balance, with the measurements made on different platforms of the same device. The moment data was taken from the lift force balance as well. The experiment was conducted by increasing the angle of attack, and there was no pressure data recorded in the experiment.

4.2.2 Validation

Figure 4.7(a) shows good agreement between CFD predictions and the experimental data for the integrated lift coefficient throughout the linear range of lift-curve slope. Both OVERFLOW and TURNS tend to slightly under-predict C_L at extreme angles of attack. Potentially, this could result from predicting that the airfoil will begin to stall at a slightly lower angle of attack, leading to a smaller lift

coefficient in the stall regime. The maximum lift coefficient is slightly lower for the Mueller airfoil than for the Eppler 387 airfoil although stall is not as dramatic.

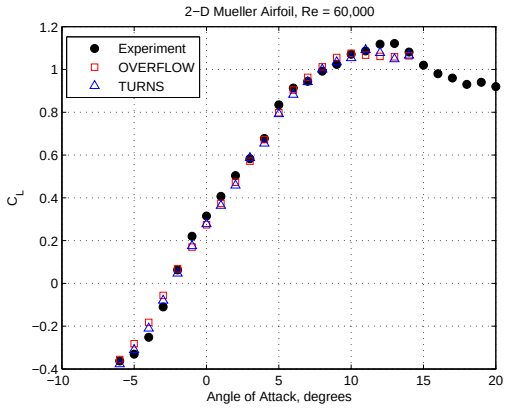

(a) Lift Validation

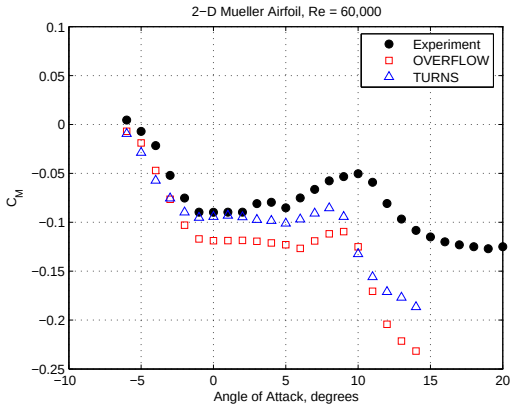

(b) Moment Validation

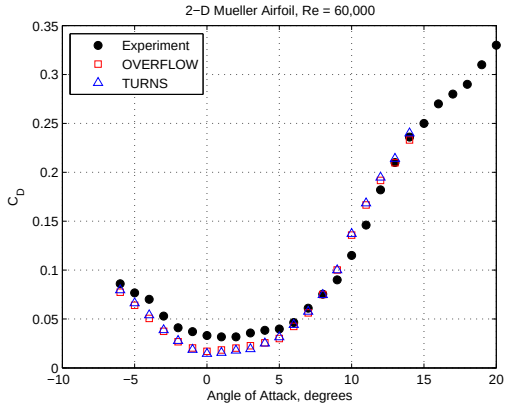

(c) Drag Validation

Figure 4.7: Mueller 2-D Results

Figure 4.7(b) shows reasonable agreement between CFD and moment coefficient data. As noted previously, CFD seems to predict stall at a shallower angle of attack. This is represented on the pitching moment curve as a small nose up

moment around $\alpha = 8°$ followed by a nose down pitching moment at $\alpha = 9°$ and $\alpha = 10°$. The TURNS code predicts results closer to the experimental values than the OVERFLOW solver. However, both predict stall at a slightly lower angle of attack. Due to the camber, the airfoil has a nose-down pitching moment at all angles of attack.

The drag validation is in Figure 4.7(c). It is readily noted that both the flow solvers under-predict the drag at moderately low angles of attack, and over-predict the drag at higher angles of attack. This is probably due to the assumption in both flow solvers that the flow is fully turbulent while in reality the flow in the experiment is transitional; at lower angles of attack the extent of the separation bubble is most likely under predicted while at higher angles of attack the fully turbulent assumption results in increased separation. Additionally, Ref. [1] contains a lengthy discussion on the influence of endplates on experimental 2-D tests for low Reynolds number flow. Mueller suggests the existence of "corner flow," defined as a region of flow at the endplate-airfoil boundary where the flow may circulate on the lower surface of the wing. This may be the reason for inaccuracy in the drag measurement. Corner flow significantly alters the 2-dimensionality of the flow, and it has been suggested that a 20% increase in the minimum drag may be added to take corner flow into account [1]. Using this margin of error, the CFD results seem quite reasonable.

4.2.3 Velocity Vectors

The velocity vector field predicted by TURNS around the Mueller airfoil is plotted at 4, 6, 9, and 10 degrees angle of attack in Figure 4.8. At $\alpha = 4°$, the flow is laminar over the majority of the airfoil surface except near the trailing edge where it separates. At $\alpha = 6°$, the point of flow separation has moved forward and a LSB has formed near the leading edge on the upper surface of the airfoil, identified by the small area of flow separation. As the angle of attack increases to $\alpha = 9°$, the LSB elongates and covers a larger portion of the upper surface of the airfoil. The flow over the trailing edge appears to be close to separating upon further increase in angle of attack. Finally, at 10 degrees, the flow over the upper surface is detached and separated as the LSB has effectively burst. In this condition, the airfoil produces less lift, as evidenced in Figure 4.7(a) where the lift curve slope has leveled off. This is a relatively low angle of attack at which to stall, suggesting that the airfoil undergoes "thin airfoil stall." The drop in lift-curve slope is perhaps not as dramatic due to the relatively low $C_{L_{MAX}}$. It can be seen that, when the flow is separated over the entire airfoil as in Figure 4.8(d), the drag has significantly increased.

4.2.4 Skin Friction Coefficient

The point of flow separation can more easily be seen where the skin friction coefficient changes sign, as in Figure 4.9. From this figure, it can be seen that the flow separates at $x/c = 0.8$ at $\alpha = 3°$. By increasing the angle of attack to $\alpha = 6°$,

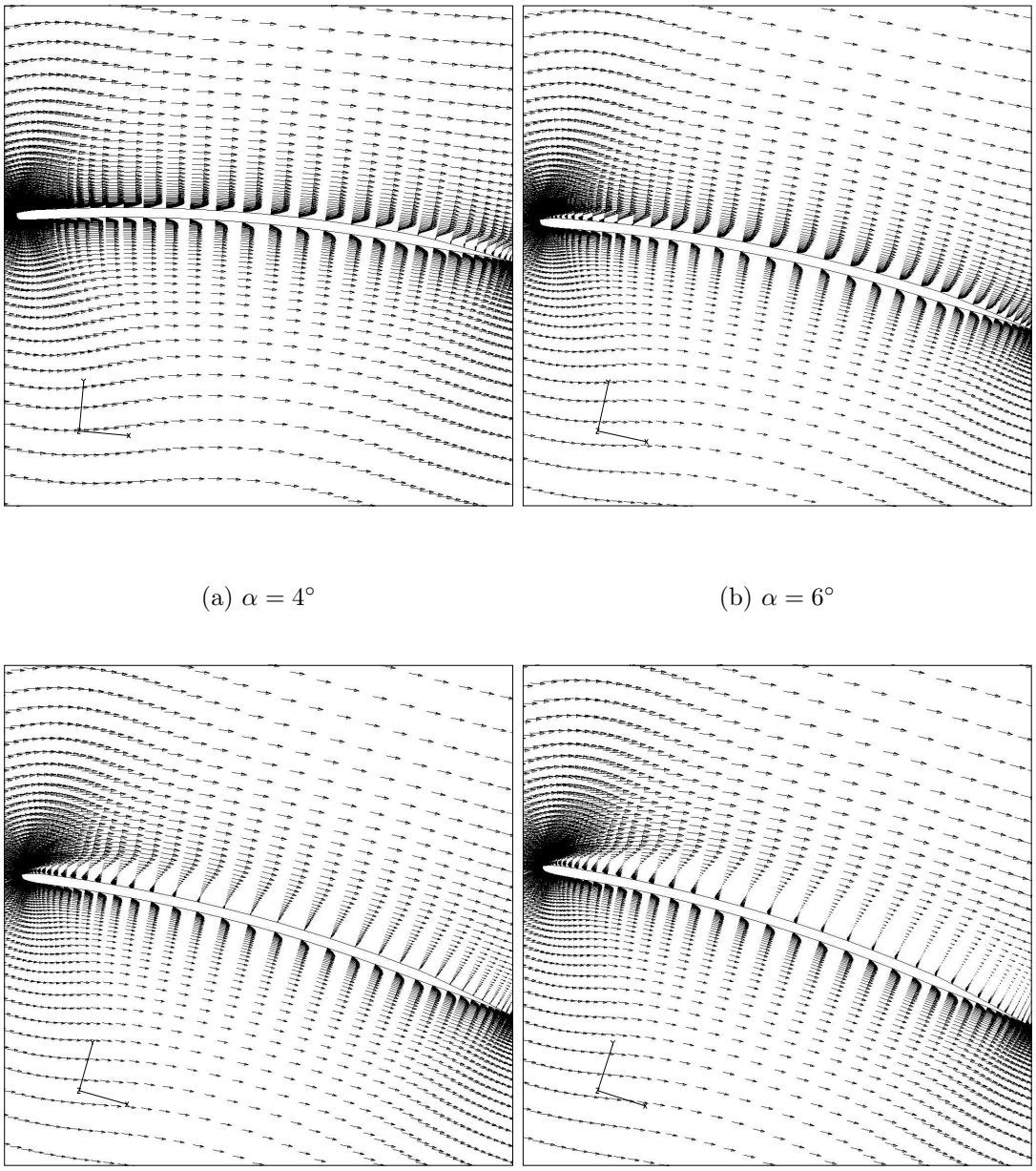

(a) $\alpha = 4°$ (b) $\alpha = 6°$

(c) $\alpha = 9°$ (d) $\alpha = 10°$

Figure 4.8: Mueller 2-D Velocity Vectors

the point of flow separation moves forward on the airfoil to $x/c = 0.2$. The laminar separation bubble covers 20% of the airfoil near the leading edge. The skin friction coefficient follows a similar curve for $\alpha = 9°$, before separating at the leading edge at $\alpha = 10°$.

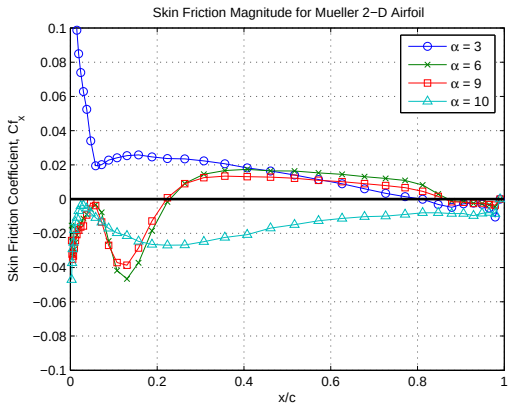

Figure 4.9: Skin Friction Coefficient over Mueller 2-D airfoil

4.2.5 Pressure Distribution

The pressure distribution for the Mueller airfoil at 6, 9, and 10 degrees angle of attack is plotted in Figure 4.10. At $\alpha = 6°$, the existence of an LSB on the upper surface manifests itself as a region of constant pressure. As the angle of attack is increased to $\alpha = 9°$, the LSB elongates, effectively creating a much more gradual transition to attached flow and strengthening the adverse pressure gradient. The suction pressure is the same for these two cases. By increasing the angle of attack further to $\alpha = 10°$, it can be seen that the suction pressure drops in magnitude while the adverse pressure gradient weakens as the flow is separated over the entire airfoil.

There is a significant difference between the upper and lower surface pressures at the trailing edge at this angle of attack, giving further evidence of massive flow separation in this region. Over the rest of lower surface however, the flow appears to be relatively unchanged over this range of angle of attack.

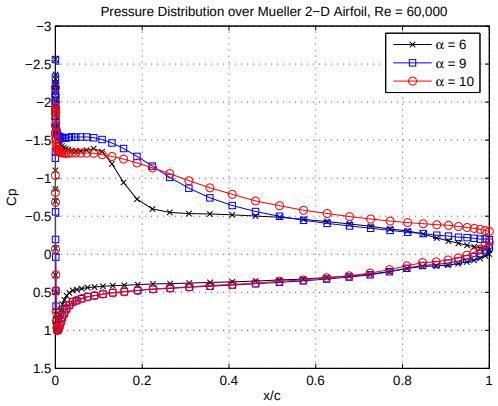

Figure 4.10: Mueller 2-D Pressure Contours

The pressure contours for the Mueller airfoil at $\alpha = 6°$ are plotted for the TURNS and OVERFLOW flow solvers in Figure 4.11. It can be seen that there is a slight difference in the predictions where the LSB forms at $x/c = 0.1$. The OVERFLOW solver predicts a shorter bubble with higher negative pressure, leading to a marginally higher lift coefficient with a stronger nose-down pitching moment than the TURNS predictions. This emphasizes the fact that predicting the LSB size and location is the key to obtaining good validation with experimental results.

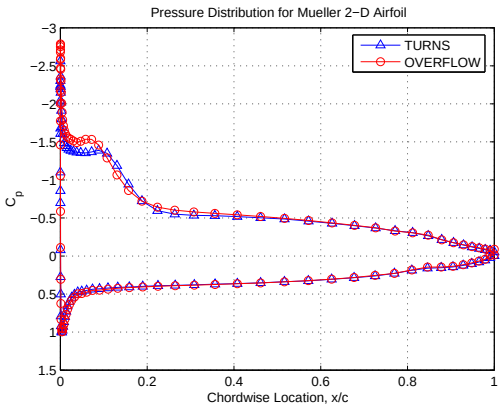

Figure 4.11: Pressure Contour for Different Flow Solvers

4.2.6 Eddy Viscosity

The predicted eddy viscosity ratio is given in Table 4.2 while the contours are plotted in Figure 4.12 and indicate that fairly low levels of turbulence are predicted in the immediate vicinity of the leading edge. The boundary layer is already relatively thick for $\alpha = 6°$ because the flow is turbulent aft of the LSB at the leading edge. Furthermore, the boundary layer thickens upon increasing the angle of attack from $\alpha = 6°$ to $\alpha = 9°$. The magnitude of the eddy viscosity is also increased in the wake. Increasing the angle of attack to 10 degrees in Figure 4.12(c) results in the turbulent region expanding in the normal direction. The turbulent boundary layer is shed as a turbulent wake at the trailing edge of the airfoil.

4.2.7 Low Mach Preconditioner Survey

To determine the effect of the low Mach preconditioner on the lift, drag, and moment calculations, the Mueller 2-D airfoil was examined at Mach numbers 0.01

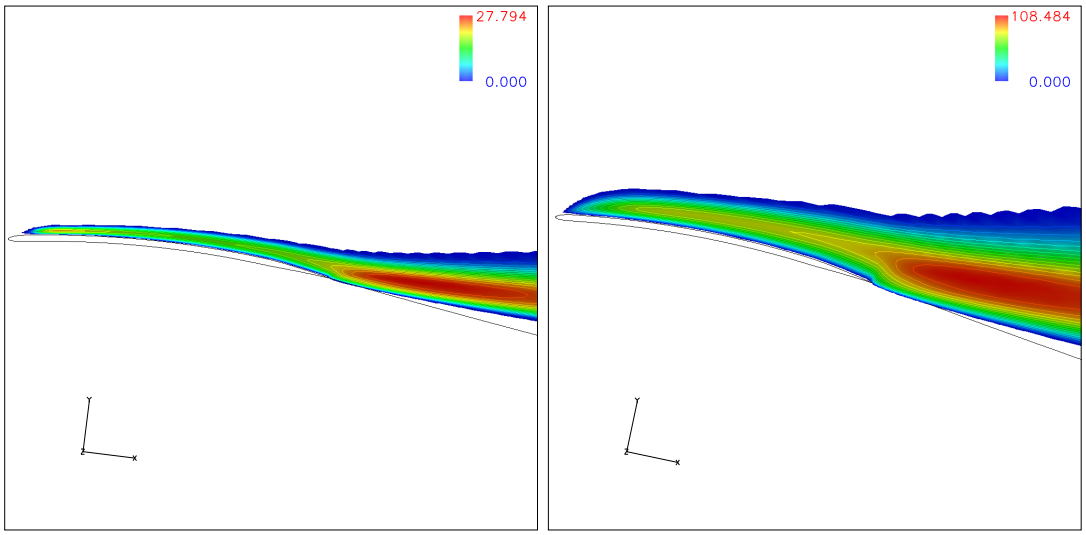

(a) $\alpha = 6°$ (b) $\alpha = 9°$

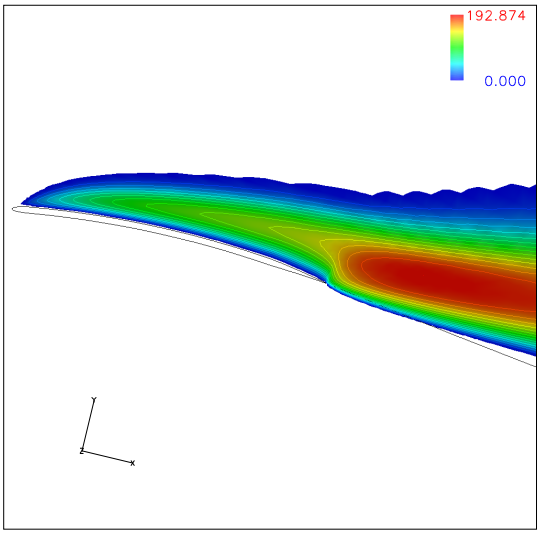

(c) $\alpha = 10°$

Figure 4.12: Contours of eddy viscosity ratio over Mueller 2-D airfoil

Angle of Attack (α)	ν_t/ν
6°	27.794
9°	108.484
10°	192.874

Table 4.2: Mueller 2-D Turbulent Viscosity Levels

Mach No.	C_L	C_M	C_D	C_L**	C_M**	C_D**
0.01	0.885	-0.097	0.044	1.069	-0.120	0.040
0.05	0.901	-0.095	0.042	1.063	-0.116	0.041
0.10	0.910	-0.096	0.041	1.054	-0.114	0.041
0.15	0.923	-0.098	0.039	0.950	-0.095	0.040
0.20	0.947	-0.096	0.043	0.944	-0.095	0.040

Table 4.3: Mach Number Survey Results (**—No low Mach Preconditioner)

through 0.2 at a Reynolds number of 60,000 and $\alpha = 6°$. The results of this survey can be seen in Table 4.3, with the experimental values of $C_L = 0.90$, $C_M = -0.075$, and $C_D = 0.044$ for $M = 0.016$.

Additionally, the solutions without the low Mach preconditioner took an average of three times as long to converge to the steady state solution. It can be seen from this table that the low Mach preconditioner may be necessary at these low Reynolds numbers for $M < 0.15$ to receive the same results as the flow solver with the low Mach preconditioner.

4.2.8 Summary

The TURNS and OVERFLOW flow solvers perform reasonably well at predicting the lift, moment, and drag coefficients for the Mueller 2-D airfoil. Upon investigating the flow physics, the laminar separation bubble is predicted fairly well although CFD predicts the bubble bursting at perhaps one degree angle of attack earlier than the experiment. The boundary layer is already thick near the stall boundary and the flow over the trailing edge seems readily apt to separate even at $\alpha = 9°$. Both flow solvers adequately resolve this combination of leading edge stall and thin airfoil stall.

It is noted from Figures 4.1(a) and 4.7(a) that both OVERFLOW and TURNS provide very reasonable results for the Eppler 387 and Mueller 2-D airfoils at low Reynolds number, even though the two airfoils are strikingly dissimilar. The Eppler airfoil is much thicker with its point of maximum camber near the quarter-chord while the Mueller wing is a very thin, circular arc with maximum camber at mid-chord. Comparing Figures 4.2(a) and 4.8(b) (both at 6 degrees), the flow is attached over a larger portion of the thinner Mueller airfoil than over the thicker Eppler 387. This is because the two airfoils exhibit different kinds of stall. CFD predicts the thinner airfoil to have a lower C_D, which is particularly useful for MAV applications. MAV airfoils are generally chosen to be thin and cambered to achieve a moderate maximum lift coefficient while producing low profile drag by keeping the flow attached over the majority of the airfoil at moderate angles of attack. Validating the experimental results associated with different airfoils from different wind

tunnels is necessary to establish a level of confidence in the flow solvers.

It is also worth mentioning that the flow solvers predict the lift to an average of 4

4.3 Static 3-D Results: Mueller Airfoil

4.3.1 The Experiment

The experimental apparatus for the 3-D experiment was the same as in the 2-D experiment, though an endplate was removed to create a cantilevered finite wing. The aspect ratio is referred to as the "semi-span Aspect Ratio" in Ref. [1] to emphasize the fact that the wing was used with an endplate. The TURNS flow solver uses a symmetry boundary condition at the blade root to simulate this "semi-span." The 3-D experiment with the Mueller wing was conducted at the same Reynolds number of 60,000 and a Mach number of 0.016. There was no wind tunnel wall effect taken into account for this experiment.

4.3.2 Validation

Both OVERFLOW and TURNS provide results in good agreement with the experimental data, as can be seen in Figure 4.13 for the lift, moment, and drag coefficients. Similarly to the 2-D cases, CFD tends to over-predict flow separation in the stall regime, thereby slightly under-predicting lift in this regions. The maximum lift coefficient is slightly less for the 3-D wing compared to the 2-D airfoil, possibly due to the spanwise distribution of lift and other 3-D effects. On the whole, the 3-D

lift predictions are much closer to the experimental data than for the 2-D predictions with the same airfoil.

The moment validation is reasonable with OVERFLOW and TURNS, although both predict a smoother curve in the region $-3^\circ < \alpha < 10^\circ$. Results from both CFD solvers show a small increase in nose-up pitching moment at $\alpha = 10^\circ$ rather than the experiment in which it occurs at $\alpha = 11^\circ$. The rise in pitching moment occurs at a higher angle of attack than in 2-D, perhaps due to 3-D effects. The computational results have reasonable qualitative agreement in the stalled flow regime at high angle of attack.

Similar to the lift, the drag is slightly overestimated at high angles of attack and slightly under estimated at lower angles of attack. Perhaps this is due to the absence of corner flow in the 2-D measurements, and the flow solvers capturing the 3-D effects very well quantitatively. Overall the agreement is quite good for both OVERFLOW and TURNS.

4.3.3 Chordwise Flow Separation

Regions of chordwise flow separation over the 3-D Mueller wing are shown in Figure 4.14. It can be seen that at $\alpha = 6^\circ$ Figure 4.14(a) there are two distinct reverse flow regions over the majority of the blade span: first a reverse flow region at the leading edge (due to LSB) and a second region near the trailing edge. However, the three-dimensional flow induced by the tip vortex eliminates the leading edge separation towards the tip of the wing. For the case of $\alpha = 9^\circ$ in Figure 4.14(b), it

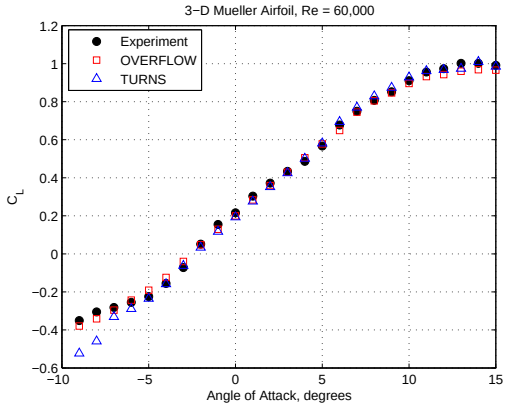

(a) Lift Validation

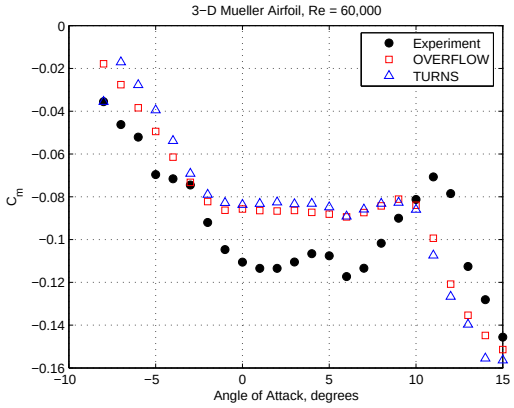

(b) Moment Validation

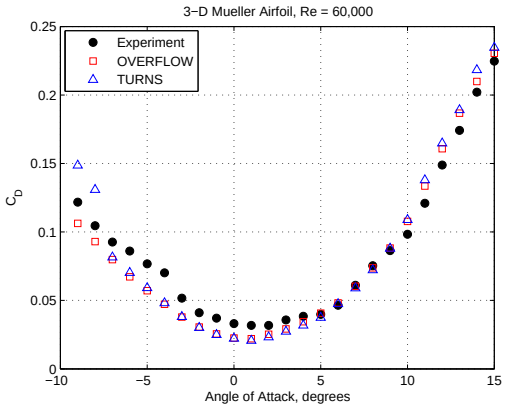

(c) Drag Validation

Figure 4.13: Mueller 3-D Results

can be seen that the first region of chordwise flow separation near the leading edge has increased as the LSB has elongated. In the 2-D airfoil results, the airfoil stalled between $\alpha = 9°$ and $\alpha = 10°$ and so this was investigated for the 3-D case. It can be seen from Figure 4.14(c) where $\alpha = 10°$ that the flow is separated from the root of the wing to nearly mid-span. Further increasing the angle of attack to $\alpha = 12°$ expands the region of flow separation outward toward the tip, where the flow has stalled over a large portion of the blade. The tip vortex induces a downwash velocity to lower the local angle of attack, and so the flow is attached in this region.

4.3.4 Chordwise Pressure Distribution

For the 3-D Mueller wing, the pressure distribution at $y/c = 49\%$, 78%, and 95% span are plotted along with 2-D results in Figure 4.15(a) for the case with $\alpha = 6°$. The LSB exists on the inboard section of the blade at $y/c = 49\%$, as can be seen by the constant pressure region near $x/c = 0.2$. The increased suction pressure on the wing due to the tip vortex forming above the wing is seen as a slight increase in C_p around $x/c = 0.7$ at 95% span. For the wing at a higher angle of attack ($\alpha = 12°$) in Figure 4.15(b), a shallow pressure gradient is seen near the leading edge of the wing on the upper surface as the blade undergoes stall. This gradual drop in pressure suggests the existence of flow separation over the majority of the blade span. Interestingly, the negative pressure increases in magnitude over the span at $\alpha = 12°$, while at $\alpha = 6°$, the negative pressure decreases in magnitude over the span. This is due to the competition for the change in the leading edge suction peak:

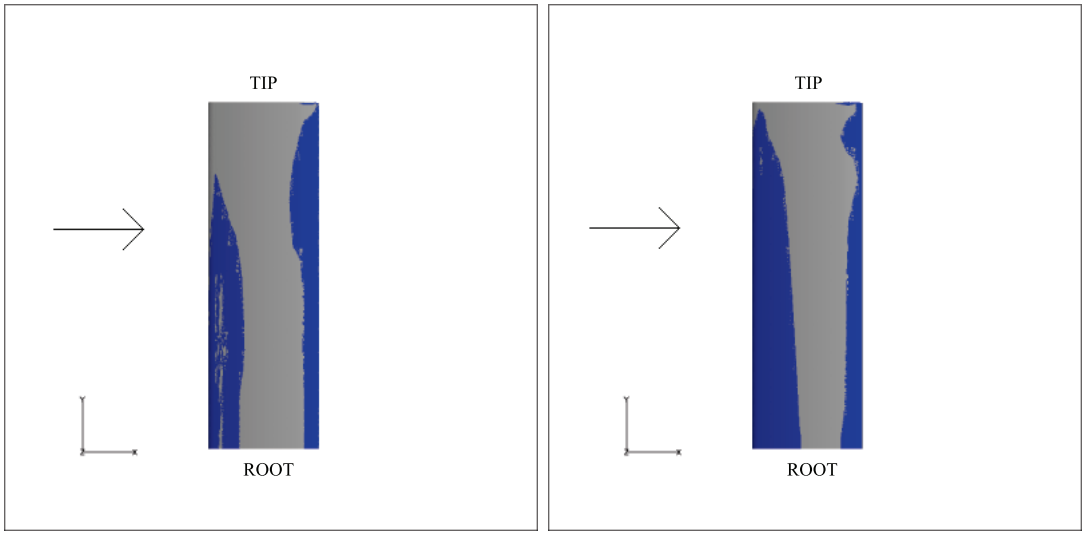

(a) $\alpha = 6°$ (b) $\alpha = 9°$

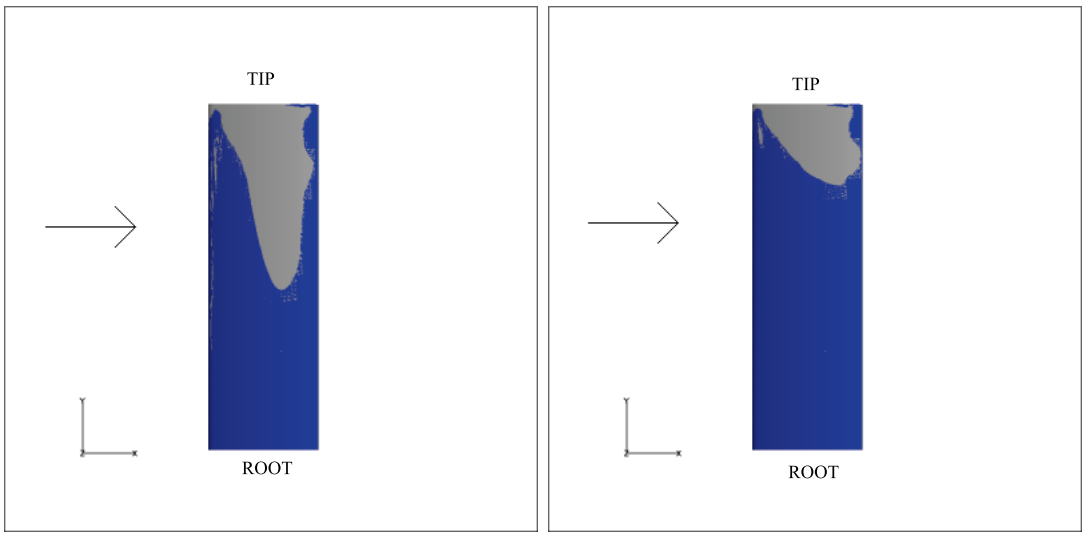

(c) $\alpha = 10°$ (d) $\alpha = 12°$

Figure 4.14: Mueller Wing Chordwise Reverse Flow Regions for Semi-Span Wing

the tip vortex reduces the local angle of attack (reducing the suction peak) while the decrease in separation toward the tip results in an increase in suction peak.

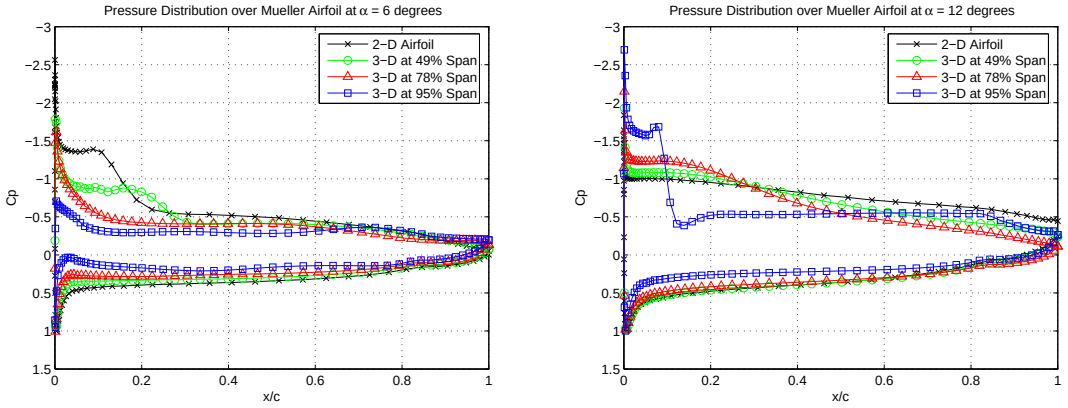

(a) 6° (b) 12°

Figure 4.15: Pressure Distribution for Mueller 3-D Results

4.3.5 Spanwise Pressure Contours

The tip vortex increases the suction pressure on the top of the blade as the flow is accelerated from the lower surface of the blade to the upper surface of the blade. However, the formation of the tip vortex is a 3-D effect that will produce less lift at the blade tip at moderate angles of attack due to the decrease in effective angle of attack. This can be seen in pressure contour plot along the wing span at $x/c = 61\%$ in Figure 4.16. The vortex has a higher pressure region fed from the lower surface of the blade wrapped tightly around the core, which has a high negative pressure fed from the upper surface of the blade.

Three-dimensional experiments and computations represent a much different

flow-field than in two-dimensions due to an unequal distribution of lift, formation of a tip vortex, and bound circulation on the blade. Thus, although two-dimensional airfoil results may be suitable for the inboard section of a blade, they are not acceptable at the outboard portion due to the tip vortex, as was discussed in Section 4.3.4.

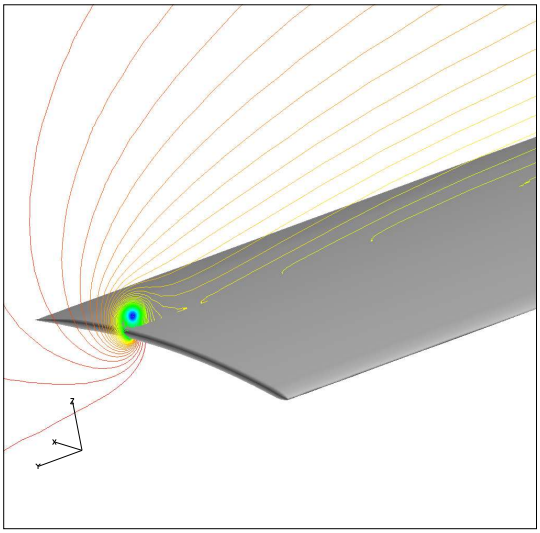

Figure 4.16: Pressure Contour over Mueller wing, $\alpha = 6°$, $x/c = 0.61$

4.3.6 Lift Distribution

Examining the lift distribution over the blade span gives insight into the extent of the effect of the tip vortex. Due to the spanwise flow component at the tip, evidence of the vortex can be seen as a gradual loss in lift with an increase in radial position towards the tip, as can be seen in Figure 4.17. Another interesting feature that CFD captures is the rotational velocity field from the vortex. This can be seen towards the tip where the induced velocity from the rotating vortex leads

to an increase in lift over half of the vortex with a decrease in lift over the other half. Figure 4.17 also shows how the point of maximum lift moves outboard with increasing angle of attack from $\alpha = 6°$ to $\alpha = 12°$.

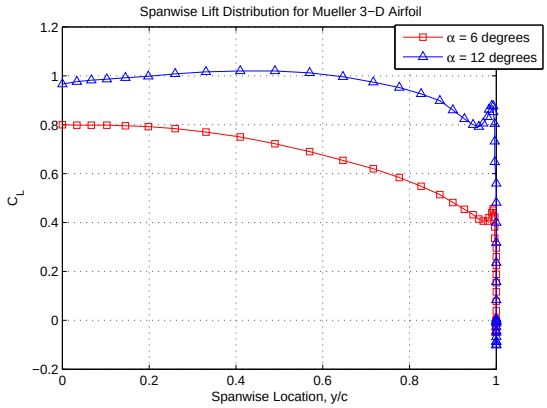

Figure 4.17: Lift Distribution

To analyze vortex formation over the chord at the blade tip, contours of pressure coefficient are plotted in Figure 4.18 at $x/c = 0.25$, 0.50, 0.75, and 1.0 at $\alpha = 6°$. It can be seen from these figures that the vortex is well developed by mid-chord, and continues to increase in size and magnitude as the flow moves over the blade. The vortex begins to dissipate as it leaves the blade primarily due to larger mesh spacing in the computations. Because the goal of this study was to validate the C_l, C_m, and C_d of the blade, capturing and retaining the details of the vortex is not of primary importance once it leaves the vicinity of the blade. Thus, prescribed wake methods were not used for these computations.

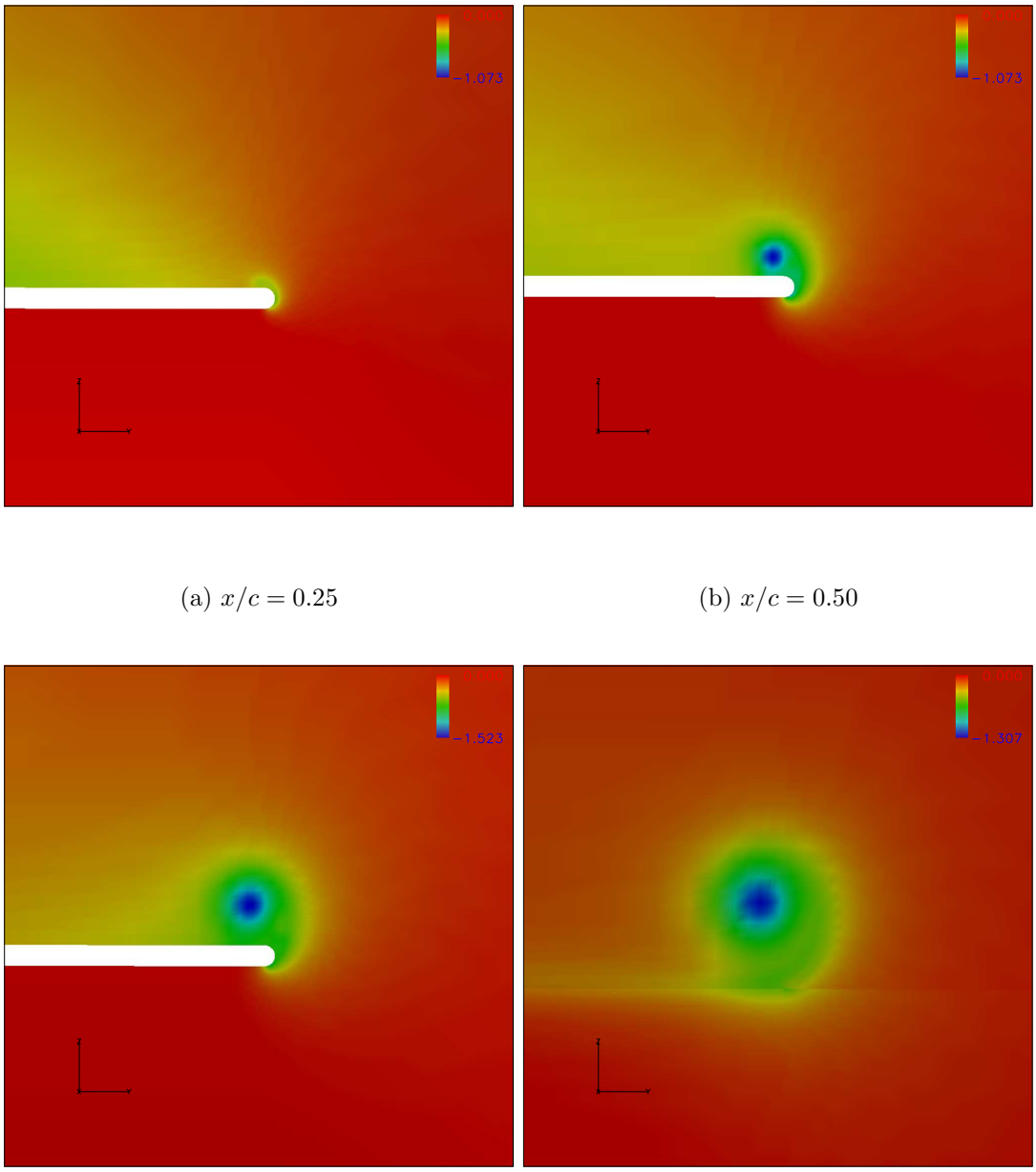

(a) $x/c = 0.25$

(b) $x/c = 0.50$

(c) $x/c = 0.75$

(d) $x/c = 1.00$ (Trailing Edge)

Figure 4.18: Pressure Contours showing vortex development over wing tip, $\alpha = 6°$

4.3.7 Vorticity

To further understand vortex development, the chordwise component of the vorticity ($\bigtriangledown \times \overrightarrow{V}$) is plotted in Figure 4.19. It can be seen that positive vorticity is fed into the vortex core from the lower surface while the negative vorticity is fed in from the upper surface. The intensity increases as the flow moves along the chord to the trailing edge in 4.19(d). A smaller and weaker counter-rotating vortex is also visible in Figure 4.19(c). As the vortex develops, it lifts away from the surface and is gradually dissipated by the flow solver.

4.3.8 Eddy Viscosity

Values of turbulent eddy viscosity are shown in Table 4.4. The turbulence levels are similar to those in the 2-D cases. It can be seen from the eddy viscosity plots for $\alpha = 6^\circ$ in Figure 4.20 that the boundary layer is thicker inboard. The eddy viscosity is at a maximum in the blade wake at 75% span where the flow is most turbulent. The boundary layer is relatively thin towards the tip where the spanwise flow induced by the formation of the tip vortex appears to minimize the separation and the thickening of the boundary layer. Similarly to the 2-D eddy viscosity plots, the boundary layer is relatively thin at the leading edge until the formation of the LSB at which the flow becomes turbulent, leading to a thicker boundary layer. For comparison, the contours of eddy viscosity are also plotted in Figure 4.21 for the wing at $\alpha = 12^\circ$. The turbulence is much stronger and thicker in the normal direction at the higher angle of attack due to a stronger pressure gradient

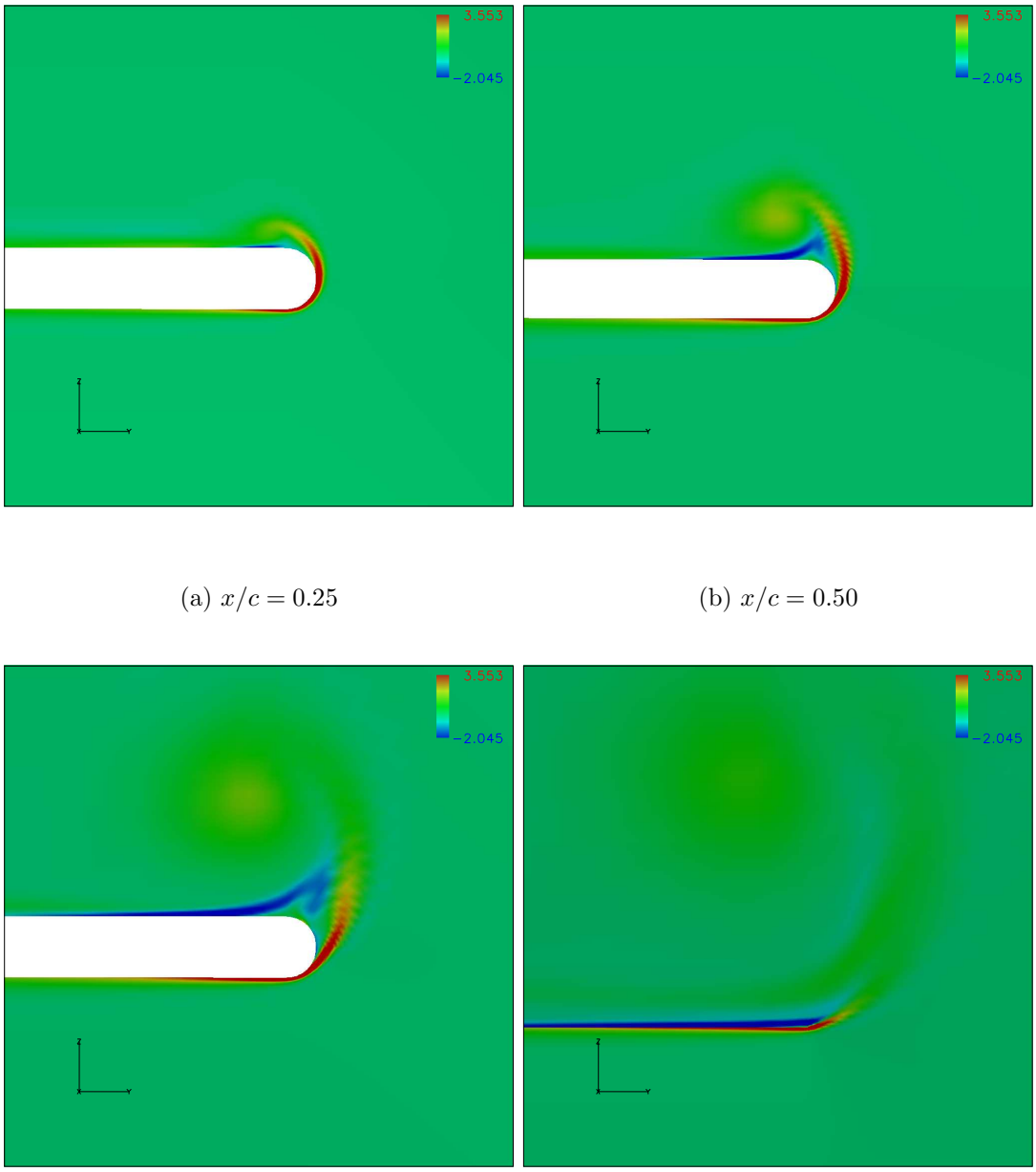

(a) $x/c = 0.25$

(b) $x/c = 0.50$

(c) $x/c = 0.75$

(d) $x/c = 1.00$ (Trailing Edge)

Figure 4.19: Chordwise vorticity showing vortex development over wing tip, $\alpha = 6°$

	ν_t/ν
6°	27.107
12°	314.553

Table 4.4: Mueller 3-D Turbulent Viscosity Levels, ν_t

over the upper surface of the airfoil, as was seen in the pressure distribution plots in Figure 4.15. The turbulence follows a similar pattern for the inboard and outboard stations as in the $\alpha = 6°$ case, including the dramatic reduction in boundary layer at the tip region where the flow remains more attached.

4.3.9 Summary

The Mueller 3-D wing has been validated through the linear lift-curve slope regime and CFD appears to have predicted stall reasonably well. Examining the flow physics has shown the impact of 3-D effects on the flow, most significantly in the formation of the tip vortex and a non-uniform spanwise distribution of lift. It is noticeable that the wing begins to stall at the root, with the region of flow separation expanding radially outward to the tip as the angle of attack increases. The boundary layer behaves similar to the 2-D cases inboard although it appears as if the spanwise velocity induced by the tip vortex reduces the turbulence in the chordwise direction at the tip.

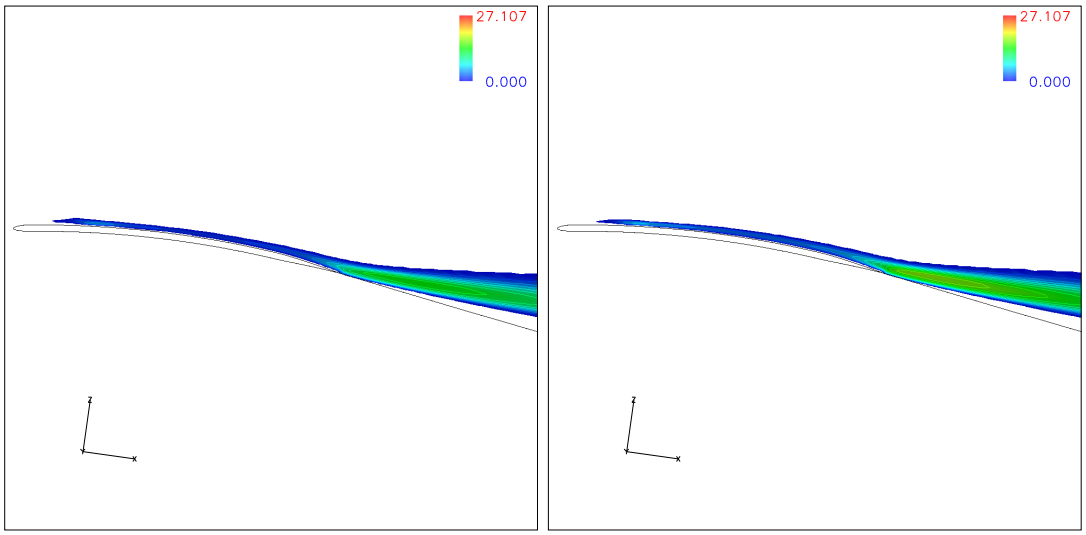

(a) $y/c = 0.25$ (b) $y/c = 0.50$

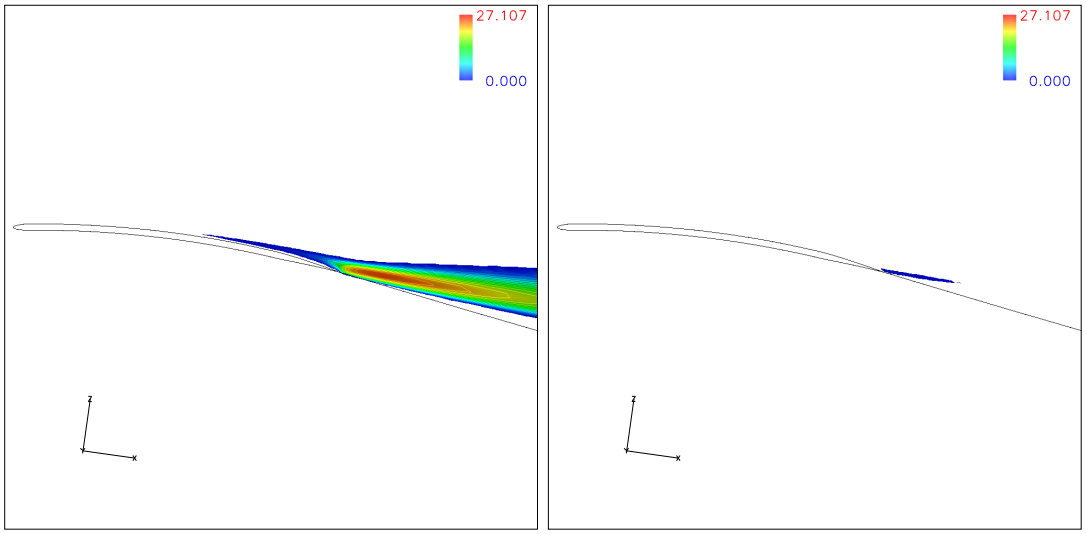

(c) $y/c = 0.75$ (d) $y/c = 0.95$

Figure 4.20: Eddy Viscosity, $\alpha = 6°$

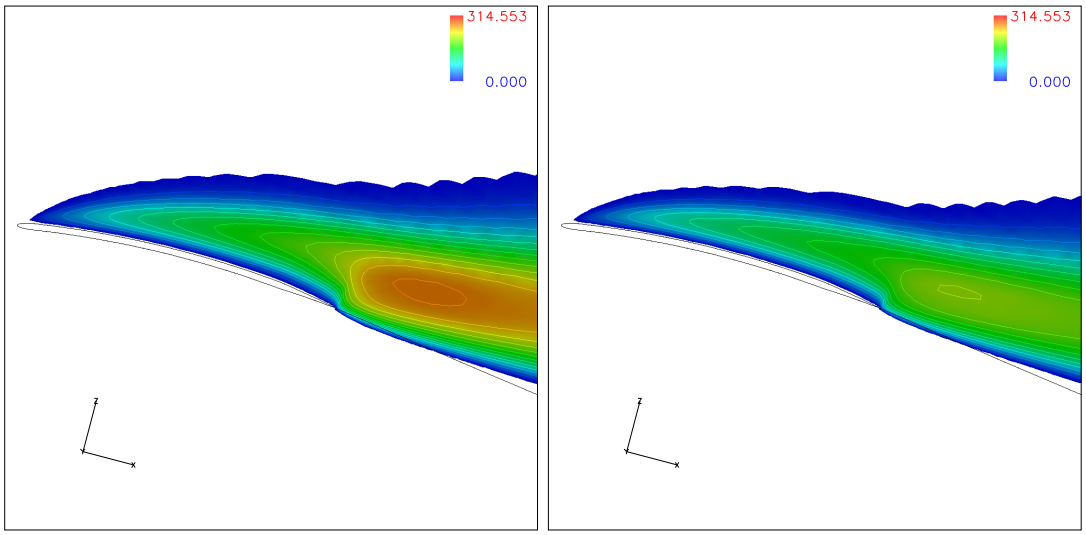

(a) $y/c = 0.25$ (b) $y/c = 0.50$

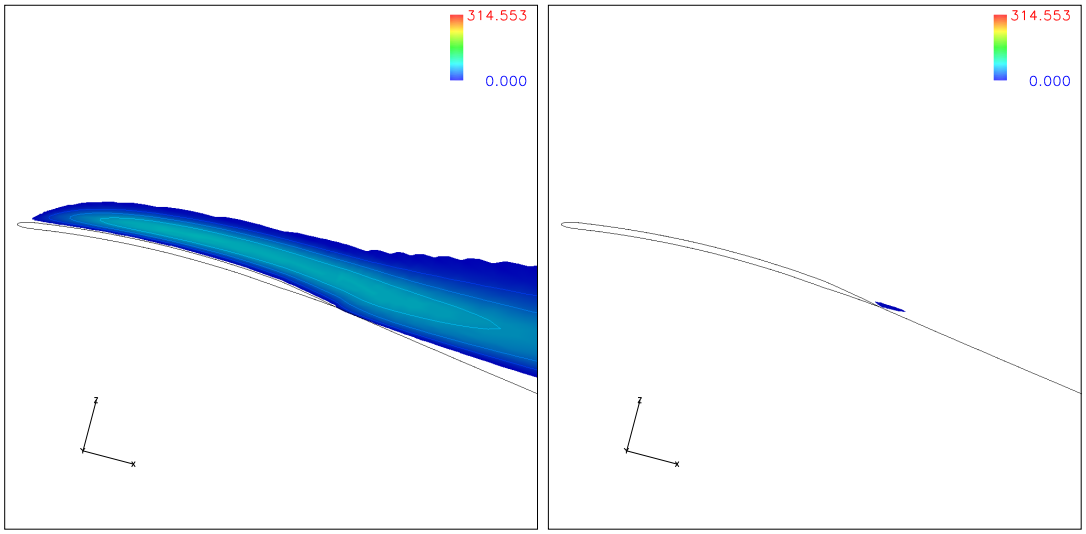

(c) $y/c = 0.75$ (d) $y/c = 0.95$

Figure 4.21: Eddy Viscosity, $\alpha = 12°$

4.4 Reynolds Number Effects

In the moderately low Reynolds number regime, good prediction of flow separation is the key to good computational results. The effect of modifying the Reynolds number is shown in Figure 4.22 for the Mueller 3-D wing using predictions from the OVERFLOW solver. Notably, the difference in lift between $Re = 60,000$ and $Re = 120,000$ is significantly larger than the difference between $Re = 120,000$ and $Re = 240,000$ as seen in Figure 4.22(a). This agrees with the results from Laitone [8] that suggests that there exists a mild increase in performance by increasing the Reynolds number above $Re = 70,000$. The drag curves in Figure 4.22(b) give similar results, and predict a larger C_d magnitude for lower Reynolds numbers due to increased viscous effects, leading to a thicker boundary layer. However, the predicted effects are also fairly mild. Also notably, α_0 is at a more negative angle of attack for the higher Reynolds number with a correspondingly lower C_{d_0}. Finally, examining the performance metric of $\frac{C_l}{C_d}$ gives the opportunity to see that a lower Reynolds number leads to poorer performance. Additionally, a lower Reynolds number has the $\frac{C_l}{C_d}$ peak shifted to a higher angle of attack. The CFD results agree reasonably well with experimental results in this regime, as can be seen in Figure 4.22(c).

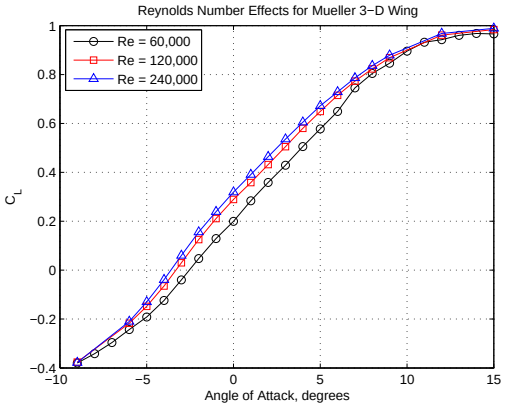

(a) Lift Comparison

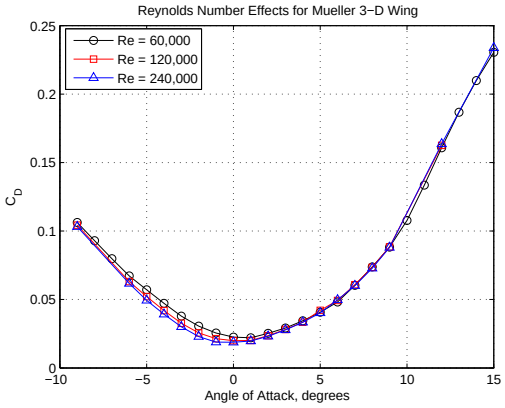

(b) Drag Comparison

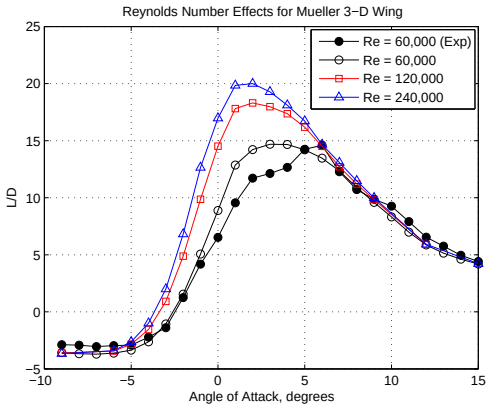

(c) L/D Comparison

Figure 4.22: Reynolds Number Effects

Chapter 5

Micro Air Vehicle in Hover

The TURNS flow solver was extended to compute the flowfield for a hovering rotor with low tip Reynolds number. Experimental data from Hein [11] was validated using this new capability. Though there is no experimental static 2-D and 3-D data, the first part of this chapter investigates 2-D and 3-D flow properties in order to gain an understanding of the flow characteristics over this particular airfoil. Using information from the 2-D and 3-D results for α_0 and C_{d_0} allows for good blade-element momentum theory (BEMT) approximations.

5.1 Experimental Setup

The MAV tested by Hein [11] had flow characteristics of a tip $Re = 51,200$ and a tip Mach number of 0.114 based on a rotor RPM of 5500. The 2-bladed rotor had a 7.62 cm span with 1.4 cm root cutout and 2.0 cm chord, giving an aspect ratio of 3.81 and a solidity of $\sigma = 0.1671$. The untwisted, untapered blades were manufactured with 7% camber based on a circular arc planform with thickness of 2.75%. These blades were modified to include a sharpened leading edge which was reported in Refs. [4, 15, 17] to give good performance at low Reynolds number. It is important to note that the camber was measured on an unsharpened blade; therefore, the effective camber may be slightly different because the camberline will

be altered by the sharpening in the final airfoil geometry. Though the experiment used blades with a blunt trailing edge, a blade with a slightly tapered trailing edge was modeled in the computations to allow good resolution at the trailing edge, and to be able to use the wake-cut boundary condition for a grid of C-type topology. This was discussed in Chapter 3 to have little effect on lift and drag results.

5.2 Static 2-D Results

Static 2-D results are approached to gain an understanding of the lift curve slope, drag characteristics, and airfoil performance of the Hein airfoil. The results are analyzed briefly so as to not lose focus on the main results of the hovering rotor.

5.2.1 Lift, Moment, Drag Curves

The lift, moment, and drag curves are plotted in Figure 5.1. The lift curve slope appears to be nonlinear in several regions. The curve can be analyzed in separate regions to gain a better understanding of the flow physics. In the low angle of attack region, from $\alpha = -4^\circ$ to $\alpha = 0^\circ$, the nonlinear behavior is attributed to the flow traversing the thin leading edge as the stagnation point is on the upper surface of the airfoil. This flow condition offers relatively poor performance for this airfoil, as expected.

Another distinct region on the curve, $\alpha = 0^\circ$ to $\alpha = 9^\circ$, is nearly linear with a small bump around $\alpha = 5^\circ$. Likely, a LSB has formed and moved forward on the airfoil. This jog in the lift curve slope is similar to the results presented in Ref. [13]

where LSB improved performance at moderate angles of attack. The increase in lift is mainly due to the separation bubble acting as a boundary layer trip. After reattachment, the boundary layer is turbulent over the rest of the airfoil. In this region, the lift curve slope is computed (in a least-squares fit) to be 5.9, which is relatively high for an airfoil in low Reynolds number flow. The drag curve slope is analogously low in this region, as can be seen in Figure 5.1(c), because the flow is attached over the majority of the airfoil.

The high angle of attack region from $\alpha = 9^\circ$ to $\alpha = 15^\circ$ is near the stall boundary where the airfoil reaches $C_{L_{MAX}}$ and begins to lose lift due to leading edge stall. The flow separation that previously was beneficial as a boundary layer trip no longer reattaches, leading to a loss in lift and sharp increase in drag. The computed $C_{L_{MAX}}$ is around 1.45 which is higher than for the Mueller airfoil because of the increased camber and sharpened leading edge which promotes a short LSB.

The pitching moment coefficient curve in Figure 5.1(b) is typical of cambered airfoils. At low angles of attack, the pitching moment is slightly nose-down while at higher angles of attack, it is severely nose-down. Stall can be seen at $\alpha = 14^\circ$ as the pitching moment curve is slightly nose-up before pitching down at stall. The levels of pitching moment are similar to those of the Mueller 2-D airfoil, which are stronger than the Eppler 387 airfoil due to the large amount of camber.

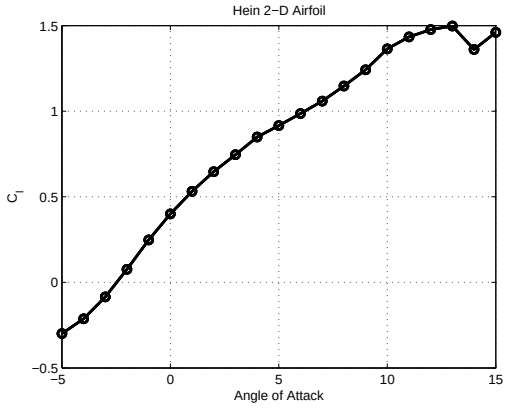

(a) Lift

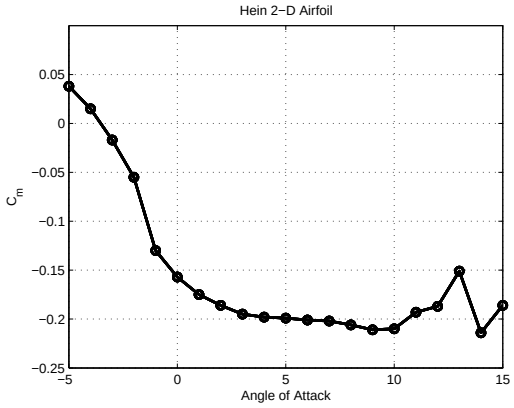

(b) Moment

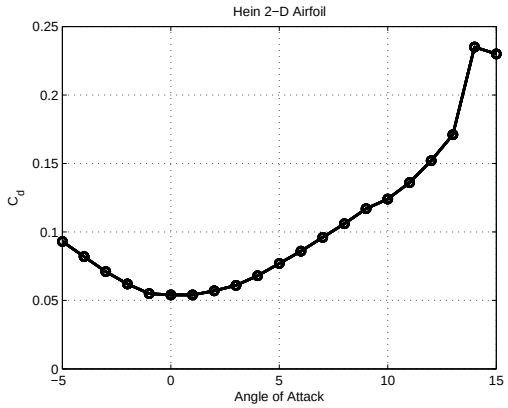

(c) Drag

Figure 5.1: Hein 2-D Results

5.2.2 Sharpened Leading Edge Effects

Examining the sharpened leading edge, there is a large area of low pressure on the upper surface where the flow expands over the sharpened leading edge and the change in geometry. The velocity vector plot in Figure 5.2(a) shows that the flow is attached over the upper surface of the airfoil at $\alpha = 6°$. Examining the pressure contours in Figure 5.2(b), it can be seen that a strong region of low pressure exists on the upper surface (and accompanying high pressure on the lower surface). Examining the leading edge at $\alpha = 13°$ in Figure 5.2(c) shows that the flow is recirculating within the LSB, as can be seen by the pressure contour in Figure 5.2(d).

5.2.3 Velocity Vectors

The velocity vectors are plotted for the 2-D Hein airfoil in Figure 5.3 at three representative angles of attack. It can be seen that the flow is generally attached over the majority of the upper surface of the airfoil at $\alpha = 6°$, with laminar separation near the trailing edge. As the angle of attack increases to $\alpha = 13°$, the point of laminar separation moves forward to the leading edge, and appears as a LSB. The flow is then attached as a turbulent boundary layer over the remainder of the airfoil. Increasing the angle of attack by one degree to $\alpha = 14°$ causes the flow to separate over the entire airfoil. Effectively, the bubble has burst, giving a leading edge stall type. It can also be seen from Figure 5.1(a) that the airfoil achieves a high maximum lift coefficient at $\alpha = 13°$ and then abruptly falls at $\alpha = 14°$ due to

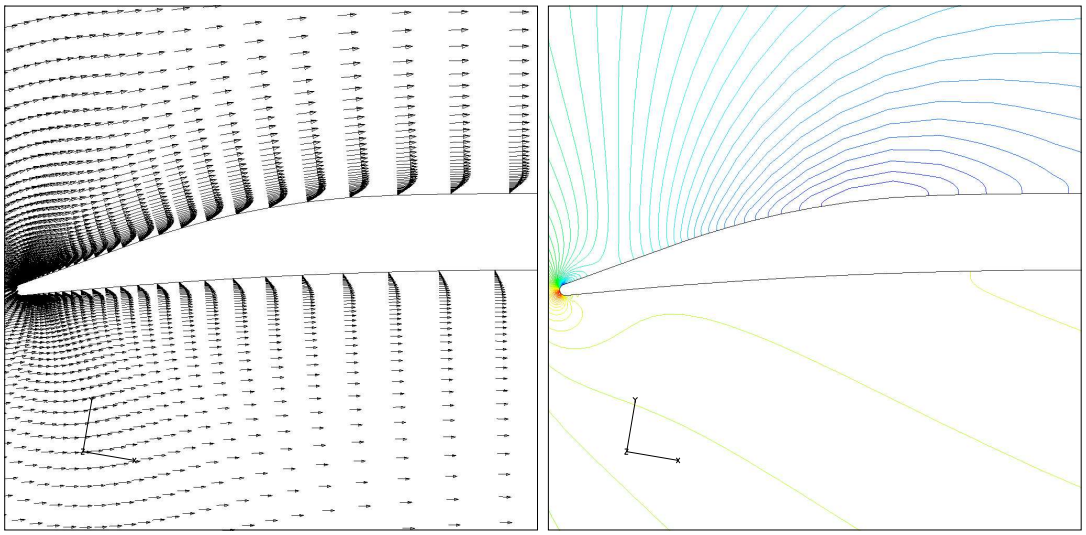

(a) Velocity Vectors, $\alpha = 6°$

(b) Pressure Contours, $\alpha = 6°$

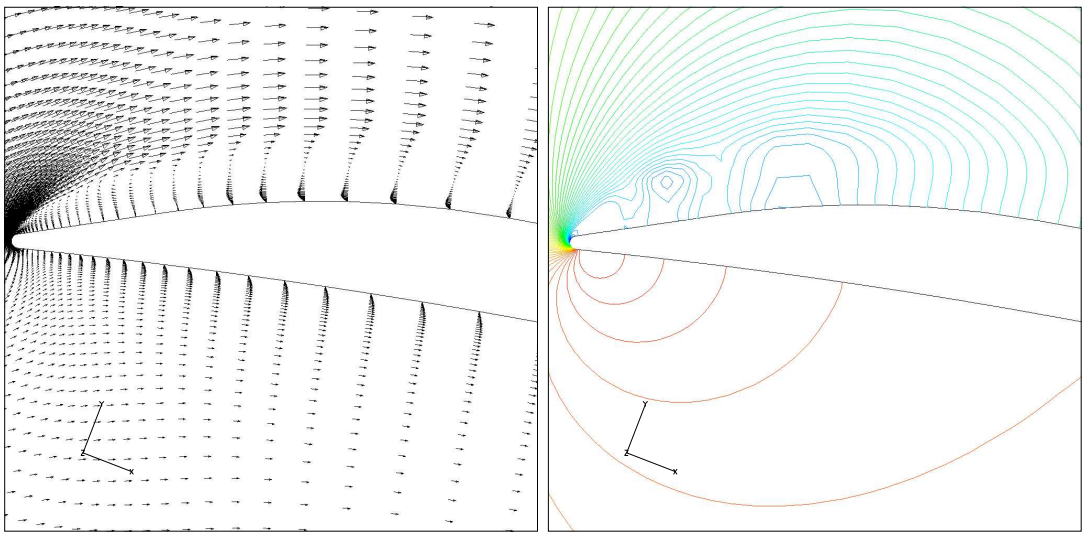

(c) Velocity Vectors, $\alpha = 13°$

(d) Pressure Contours, $\alpha = 13°$

Figure 5.2: Close-up of Leading Edge of Hein Airfoil

the flow separation.

5.2.4 Pressure Distribution

The pressure distributions in Figure 5.4 show the effect of the flow separation at the sharpened leading edge. This is very pronounced at the higher angles of attack where the flow stagnates, accelerates, and then separates briefly near $x/c = 0.1$. For the $\alpha = 13°$ case, the pressure contour still shows a bump in pressure near $x/c = 0.1$ although the suction pressure is much larger. There is a decrease in negative pressure on the upper surface due to flow separation. The airfoil stalls at $\alpha = 14°$ where there is a loss in negative pressure on the upper surface.

5.2.5 Eddy Viscosity

Turbulence levels can be examined in the eddy viscosity plots in Figure 5.5. The $\alpha = 6°$ case has a laminar boundary layer over much of the airfoil until the trailing edge where it separates. Due to the LSB on the upper surface at $\alpha = 13°$, boundary layer is thick over the entire airfoil. As the angle of attack increases further to $\alpha = 14°$, the eddy viscosity increases in magnitude (Table 5.1) and the boundary layer thickens.

5.2.6 Grid Refinement

To analyze the accuracy of the 2-D mesh that was used for the calculations in this section, a grid refinement study was completed. The grid parameters are in

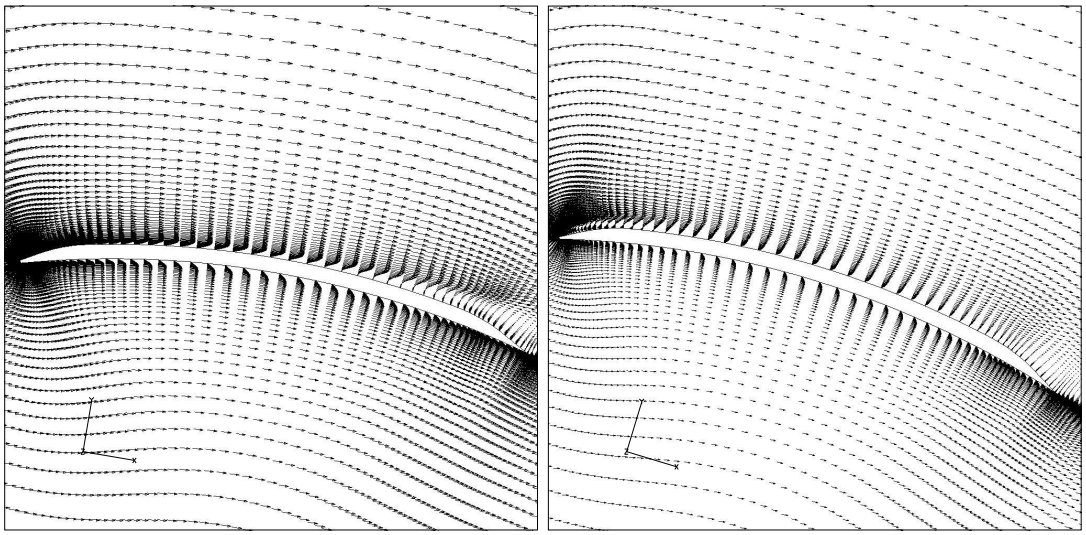

(a) $\alpha = 6°$ (b) $\alpha = 13°$

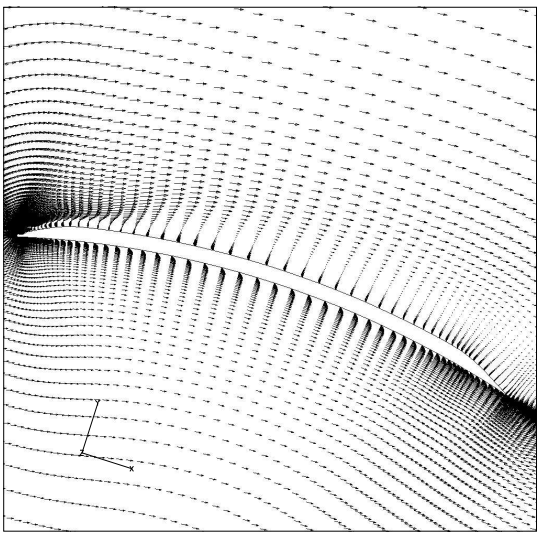

(c) $\alpha = 14°$

Figure 5.3: Hein 2-D Velocity Vectors

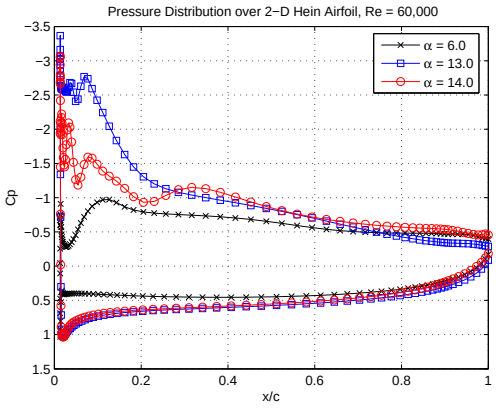

Figure 5.4: Hein 2-D Pressure Distribution

	ν_t/ν
$\alpha = 6°$	90.197
$\alpha = 13°$	84.460
$\alpha = 14°$	244.884

Table 5.1: Hein 2-D Turbulent Viscosity Levels, ν_t

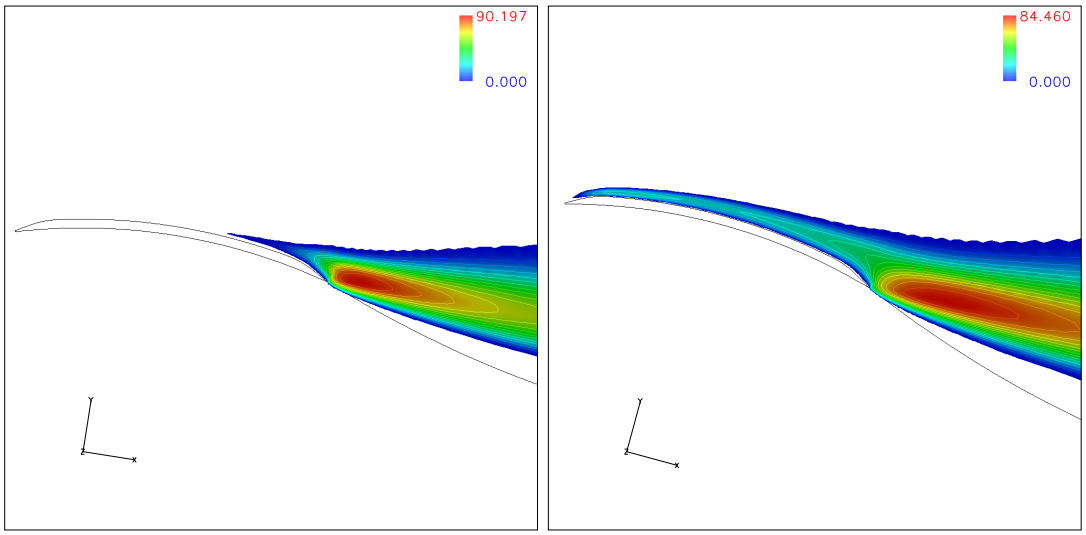

(a) $\alpha = 6°$ (b) $\alpha = 13°$

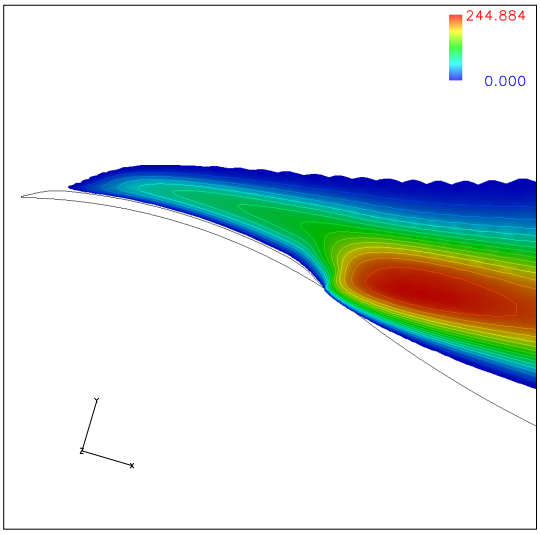

(c) $\alpha = 14°$

Figure 5.5: Eddy Viscosity Contours over Hein 2-D airfoil

	JDIM	KDIM	NPTS
Grid 1 "coarse"	227	81	1.8×10^4
Grid 2 "fine"	347	161	5.6×10^4

Table 5.2: 2-D Grids used in Refinement Study

Table 5.2. It can be seen that the fine grid contains 3 times as many points as the coarse grid. Because the lift, moment, and drag coefficients are nearly the same for both grids (as can be seen in Figure 5.6), it was concluded that the coarse mesh contains a sufficient number of points to compute an adequate solution while making efficient use of the computational resources available. Thus, the coarse mesh was used in subsequent 3-D calculations.

5.2.7 Summary

The Hein airfoil exhibits a relatively high maximum lift coefficient compared to the Eppler 387 and Mueller airfoils due to its large amount of camber and sharpened leading edge. The sharpened leading edge promotes transition to turbulent flow at high angles of attack where the change in geometry effectively trips the boundary layer. The cost of the high lift is relatively high nose-down pitching moments and high drag.

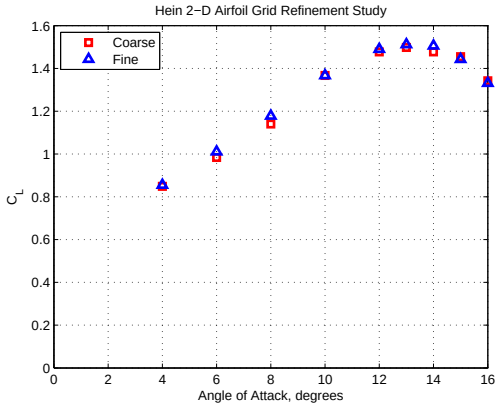

(a) Lift

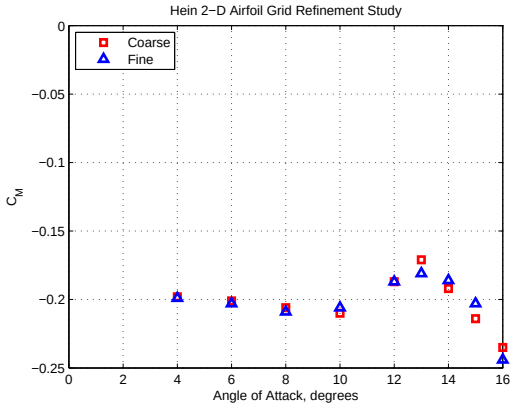

(b) Moment

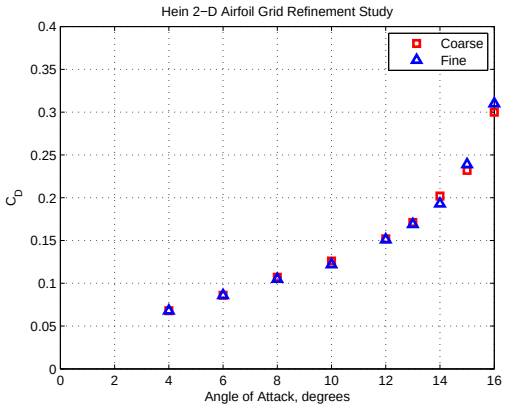

(c) Drag

Figure 5.6: Grid Refinement Study Results

5.3 Static 3-D Results

Static 3-D calculates are performed on a mesh system similar to the Mueller 3-D cases. The mesh collapses at the tip to form a C-O mesh to capture the tip vortex. The aspect ratio was 3.81, and the flow conditions were again $M = 0.114$ and $Re = 51,200$. The angles of attack examined are all positive, and correspond to the collective angles measured in the hover model to be discussed in the next section.

5.3.1 Lift, Moment, Drag Curves

The lift, moment, and drag curves for the 3-D Hein airfoil are shown in Figure 5.7. The 3-D lift curve is similar to the 2-D lift curve although the measured lift is slightly less due to 3-D effects. The pitching moment is again strong and nose-down, while the drag is also still high. Stall is predicted around the same angle of attack ($\alpha = 14°$) as the 2-D case, again of leading edge stall type.

5.3.2 Contours of Chord-wise Recirculation

The regions of chordwise flow recirculation are plotted in Figure 5.8 for several angles of attack. At $\alpha = 6°$ in Figure 5.8(a), the flow is separated at the trailing edge. Notably, the LSB does not form until the angle of attack is increased to $\alpha = 10°$. The region of flow separation at the leading edge expands as the angle of attack is increased to $\alpha = 14°$. The flow is still attached over the middle of the chord at this angle of attack; however, increasing the angle of attack further to $\alpha = 15°$ as

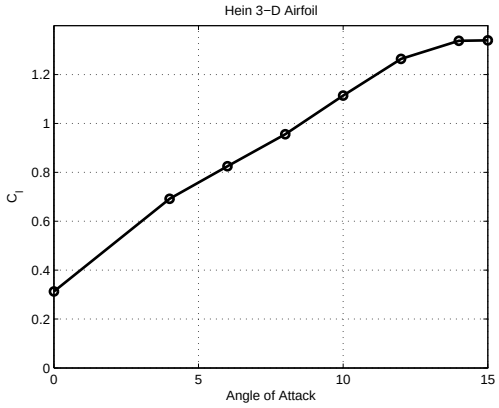

(a) Lift

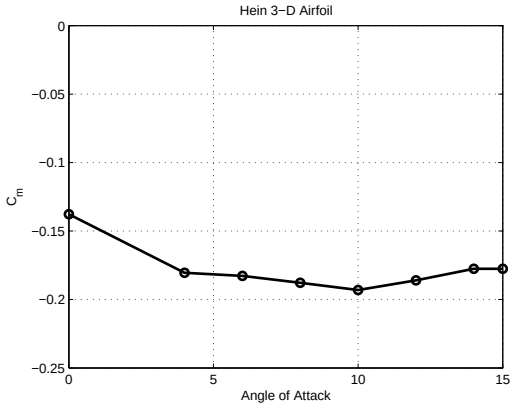

(b) Moment

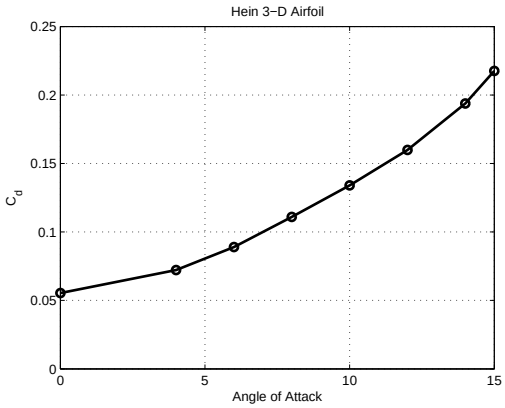

(c) Drag

Figure 5.7: Hein 3-D Lift, Moment, Drag Curves

in Figure 5.8(d) results in the flow stalling over the inboard section of the blade. This is at a slightly higher angle of attack than in the 2-D airfoil results, possibly due to the 3-D effects. For all of these plots, the flow over the tip region does not undergo flow recirculation in the chordwise direction due to the presence of the tip vortex which reduces the local angle of attack.

5.3.3 Pressure Distribution

An analysis of the chordwise pressure distribution at several spanwise locations is presented in Figure 5.9 for $\alpha = 15°$. The 3-D wing exhibits a similar pressure distribution as the 2-D airfoil at the inboard stations. The suction pressure is reduced at the leading edge with an increase in radial position. All of the 3-D stations have a relatively shallow pressure gradient because the the flow is turbulent over most of the airfoil. The outboard station has a particularly flat pressure contour, although Figure 5.8(d) indicates that the flow is attached in the chordwise direction. The tip vortex reduces the local angle of attack in this region, which keeps flow attached at the tip. The presence of the tip vortex also leads to a higher negative pressure over the chord.

5.4 Summary

The 3-D Hein wing stalls at a similar angle of attack as the 2-D airfoil with a high maximum lift coefficient. Similar to previous 3-D cases, the flow begins to stall inboard, and moves outboard upon subsequent increase in angle of attack. The

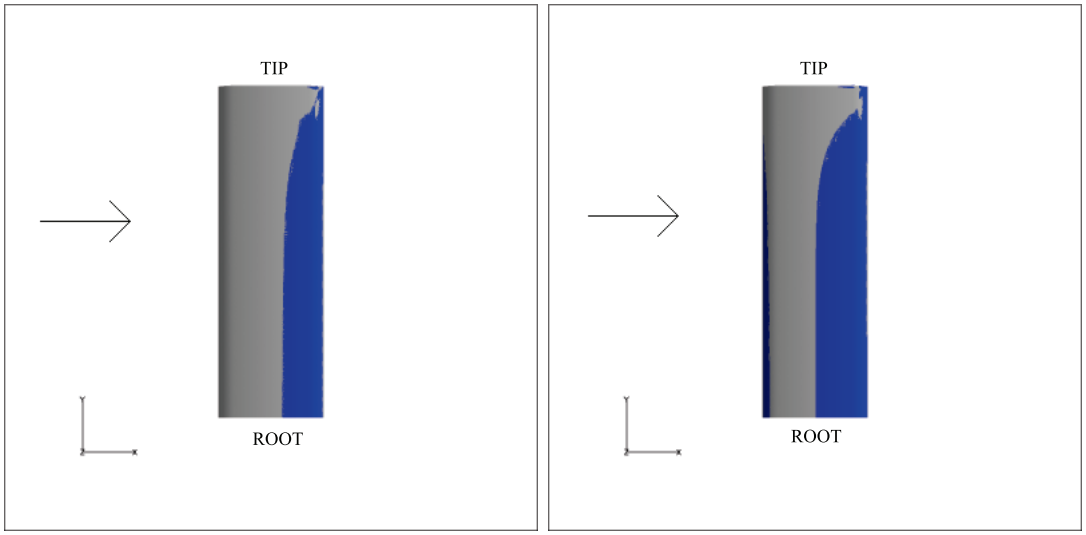

(a) $\alpha = 6°$ (b) $\alpha = 10°$

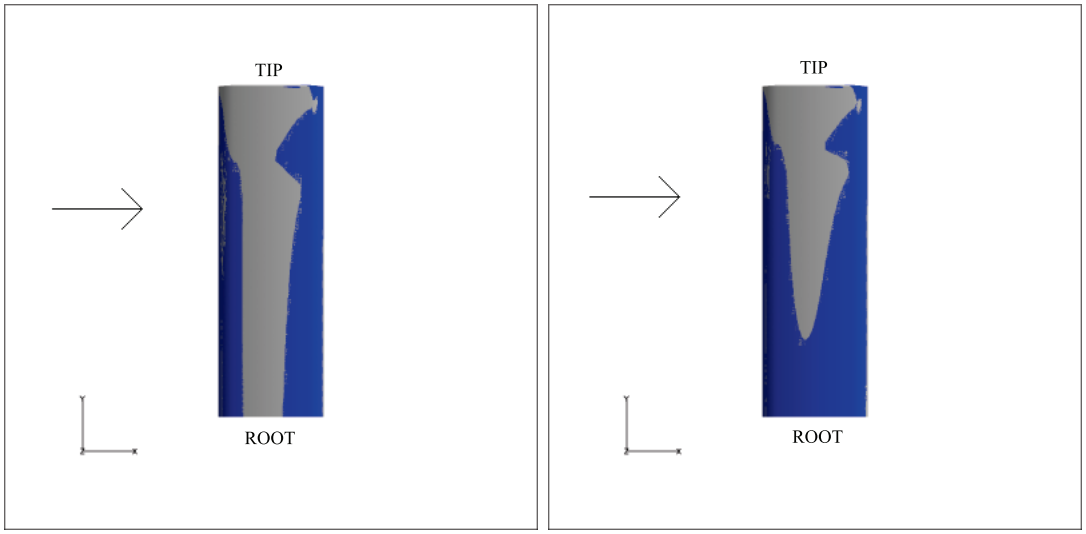

(c) $\alpha = 14°$ (d) $\alpha = 15°$

Figure 5.8: Regions of Chordwise Recirculation

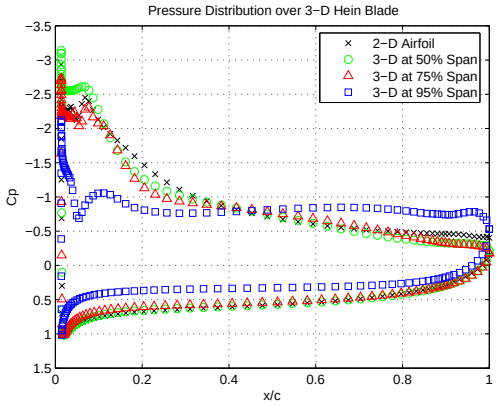

Figure 5.9: Hein 3-D Pressure Contours, $\alpha = 15°$

high amount of camber and sharpened leading edge give good lift characteristics and delay stall until higher angles of attack for this airfoil, although the pitching moment and drag coefficients are still relatively high.

5.5 Hover 3-D Results

The actual experiment conducted by Hein was for a 2-bladed MAV rotor with $Re_{tip} = 51,200$, $Re_{root} = 10,000$, $M_{tip} = 0.114$, $M_{root} = 0.03$. The experiment was conducted with the rotor thrusting downwards from a hover test stand to avoid the influence of ground effect. Flow visualization from the experiment showed considerable wake obstruction near the root, as can be seen in Figure 5.10. The TURNS code has a difficult time predicting the steady-state solution over the inboard portion of the blade because the flow near the root appears to be unsteady.

Experimental results are presented in quantities of FM, and C_T. For the computational results, it is possible to integrate the surface pressures acting on the

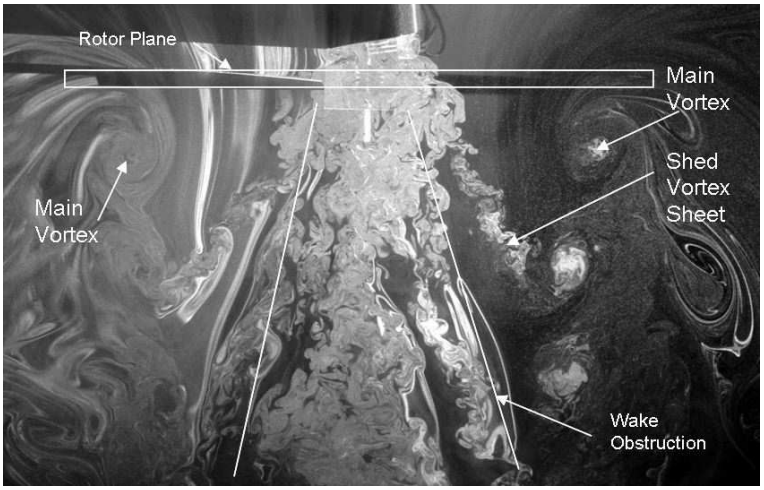

Figure 5.10: Flow Visualization for Hein rotor, from [11]

blade to find the sectional lift coefficient. This in turn can be used to find the sectional thrust and integrated thrust. The incremental lift per unit span, dL, is defined by:

$$dL = \frac{1}{2}\rho U^2 c C_l dy \tag{5.1}$$

where U is the local velocity, c is the local blade chord, and dy is the incremental length along the span. The incremental thrust per unit span, dT, can similarly be defined using small-angle simplifying assumptions as:

$$dT = N_b dL \tag{5.2}$$

where N_b is the number of blades. Substituting equation 5.1 into 5.2 yields (with $C_T = \frac{T}{\rho A(\Omega R)^2}$):

$$dC_T = \frac{N_b dL}{\rho A \left(\Omega R\right)^2} = \frac{N_b \left(\frac{1}{2}\rho U^2 c C_l dy\right)}{\rho \left(\pi R^2\right) \left(\Omega R\right)^2} \tag{5.3}$$

$$dC_T = \frac{1}{2}\sigma C_l \left(\frac{y}{R}\right)^2 d\left(\frac{y}{R}\right) \tag{5.4}$$

where $\sigma = \left(\frac{N_b c}{\pi R}\right)$. The total thrust can then be found by integrating Equation 5.4 across the blade span.

5.5.1 Convergence

The hover computations took several thousand iterations more for the residue to converge one order of magnitude, as can be seen in Figure 5.11(a). Although the residue is steadily decreasing, the thrust is slightly oscillating, as can be seen in Figure 5.11(b). Flow visualization of the TURNS solution at several instances in the computations showed that the loads on the outboard portion of the blade changed very little, although the loads on the inboard portion of the blade changed significantly. It can thus be concluded that the thrust is oscillating mainly due to unsteady effects on the inboard portion of the blade. The values of C_T taken as the "converged" solution for the results in this section are average values as illustrated in Figure 5.11(b).

5.5.2 Performance Curves

Figure 5.12 shows thrust curves for experimental, Blade-Element Momentum Theory (BEMT), and CFD results. BEMT is used to predict performance for helicopter rotors, as described in Ref. [37]. For the BEMT results, $\alpha_0 = -3°$ and $\overline{C_{d_0}} = 0.05$ based on the 2-D results presented in Section 5.2. BEMT was used with

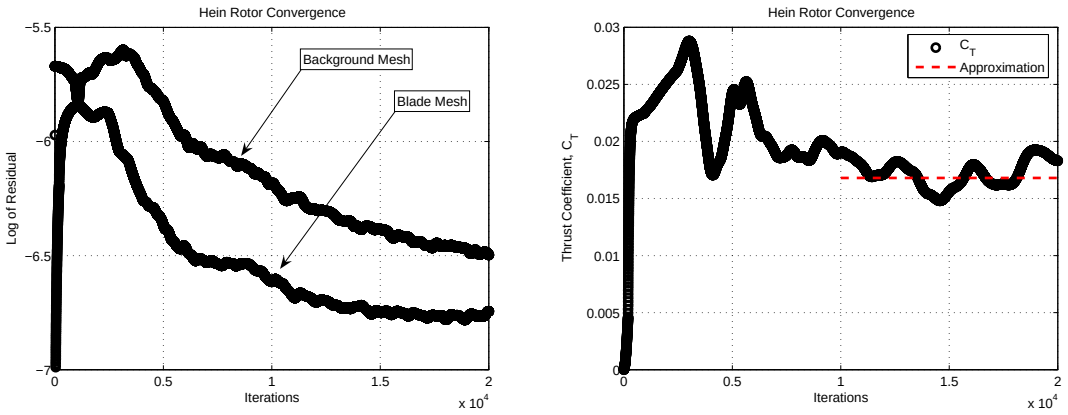

(a) Residual Convergence

(b) C_T Convergence

Figure 5.11: Hein Rotor Convergence Rates

ideal wake contraction based on full-size rotors. It can be seen that the TURNS flow solver slightly over-predicts the thrust for most collectives compared to the experimental data. It is also notable that results from the TURNS solver are closer to experimental data and BEMT approximations at higher collectives.

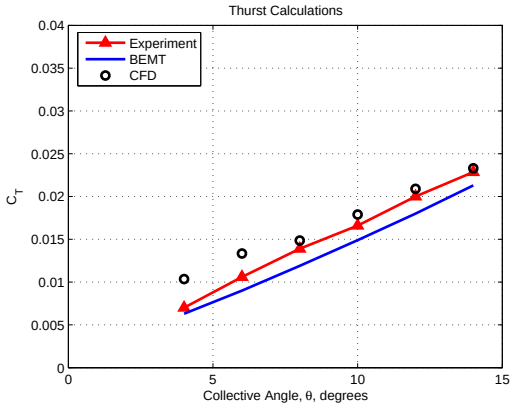

Figure 5.12: Hein Hover Results

Commonly the figure of merit (FM) is used to measure performance for heli-

copter rotors. It is important to note that at low Reynolds numbers, there may be coupling between the induced and profile power due to the relatively high viscous effects. The definition of FM is repeated in Equation 5.5 for clarity.

$$FM = \frac{\frac{C_T^{3/2}}{\sqrt{2}}}{\frac{\kappa C_T^{3/2}}{\sqrt{2}} + \frac{\sigma C_{d_0}}{8}} \tag{5.5}$$

Figure 5.13 shows the predicted FM from CFD, BEMT, and the FM calculated from experimental data against blade loading (C_T/σ). Due to the overprediction of thrust, CFD overpredicts FM because the effect of the profile power coefficient ($\frac{\sigma C_{d_0}}{8}$) will be smaller. The profile power may not be insignificant at low tip Reynolds numbers. The TURNS code may also be underpredicting drag, which leads to a higher FM. However, the TURNS code does predict a maximum FM at the highest blade loading, which is qualitatively correct. It is noted that experimental FM values agree reasonably well with BEMT approximations.

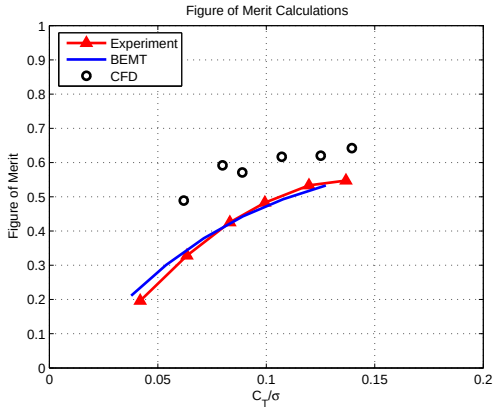

Figure 5.13: Hein Rotor Performance

To gain a better understanding of the rotor performance, the FM is broken down into ideal and actual power in Figures 5.14 and 5.15. The ideal power is

based solely on the rotor thrust ($C_{P_{IDEAL}} = \frac{C_T^{3/2}}{\sqrt{2}}$). The ideal power is plotted against collective angle in Figure 5.14(a), which is similar to Figure 5.12 because the ideal power is a simple function of rotor thrust. Alternatively, the ideal power required can be plotted against blade loading in Figure 5.14(b) where CFD gives reasonable agreement for most blade loadings.

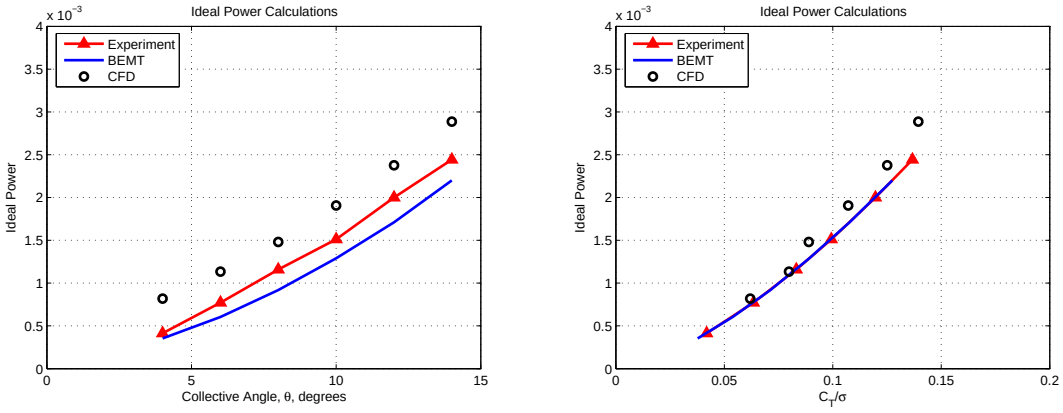

(a) Ideal Power vs. Collective Angle

(b) Ideal Power vs. Blade Loading

Figure 5.14: Hein Rotor Ideal Power

The actual power required by the MAV rotor is plotted with BEMT and CFD predictions against collective angle in Figure 5.15. The BEMT approximation is relatively low, perhaps because the profile power may be underpredicted because BEMT does not take into account low tip Reynolds number effects. CFD results closely approximate both BEMT and experimental results. This is probably due to the TURNS code over-predicting the thrust (and therefore induced power) and under-predicting the profile power. Examining how the actual power varies with blade loading again shows good qualitative agreement, particularly at high blade

loadings. It can be seen from Figure 5.15(b) that by underpredicting the actual power, CFD effectively overpredicts the FM.

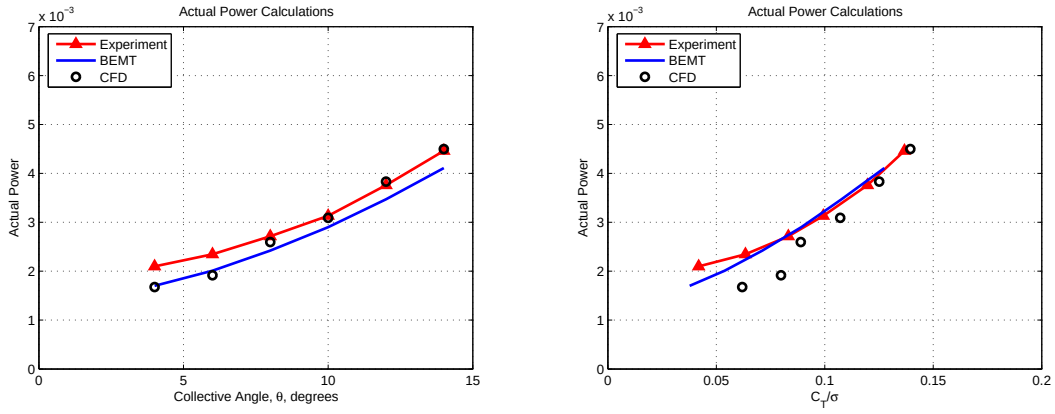

(a) Actual Power vs. Collective Angle

(b) Actual Power vs. Blade Loading

Figure 5.15: Hein Rotor Actual Power

5.5.3 Flowfield

In the TURNS solution, one vortex passage has been resolved in the rotor wake in addition to the vortex forming on the blade. These vortices can be seen in the background mesh in Figure 5.16. Notice that the wake has not contracted, as the vortex in the wake appears to be directly below the tip of the blade. Conversely, the vortices along the slipstream boundary have contracted a significant amount in the experiment (seen in Fig. 5.10). At one-half rotor revolution, the wake has contracted to $r/R = 0.8$, while at one full rotor revolution, the wake has contracted slightly further to $r/R = 0.78$. Thus, the loads on the blade in the CFD calculations may be slightly different from the experiment due to the different location of the tip

vortex in the wake. If the wake were to contract in the computational solution, the vortex would induce a velocity on the portion of the blade that produces a significant amount of lift. This vortex affects the blade loads and power calculations. Because the vortex is outboard of the tip, however, it induces a velocity on a portion of the blade where the lift produced is much lower. Therefore, the lift and drag calculations give somewhat better performance in terms of thrust and power than was measured experimentally.

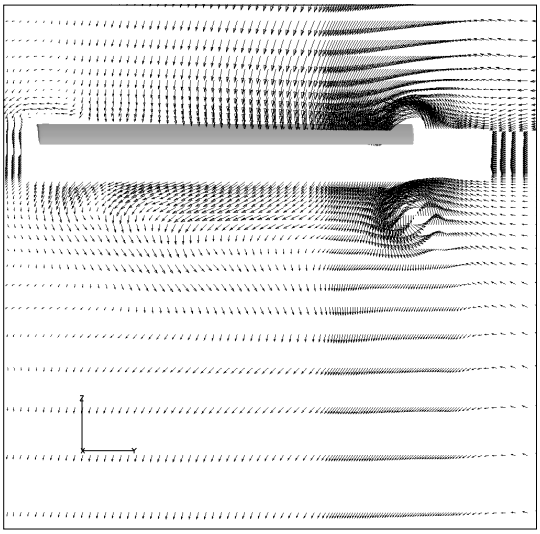

Figure 5.16: Background mesh, $\theta = 8°$

It is also noted that there is only one vortex resolved in the farfield mesh beneath the blade. The vortex at a later wake-age has diffused, mainly due to increased mesh spacing. The mesh spacing is fine at the blade where the vortex forms; however, the resolution decreases as the vortex convects downward. Thus, the influence of additional passes of the vortex on the blade is unknown.

The vortex is expected to convect along the slipstream boundary as the wake

contracts below the rotor disk. The farfield boundary 14 chords beneath the rotor was chosen to see the wake contraction ratio, which momentum theory gives as $\frac{1}{\sqrt{2}} = 0.707$. The measured contraction ratio was 0.76 (similar to the experiment), as can be seen in Figure 5.17. This is fairly close to the momentum theory approximation. The wake contraction ratio is somewhat prescribed by the boundary conditions, and thus the shape of the contraction is different than was seen in the experiment. In the experiment, the wake contracted significantly after one half rotor revolution, and little further in subsequent measurements. In the CFD solution, however, the wake has contracted slightly near the blade, and contracts significantly further in the far-field. Again, the wake could have been modeled with finer resolution but it was decided to keep the computational cost low because the objective was to obtain thrust and drag data. Additionally, accounting for swirl effects could possibly bring the wake contraction ratio closer to the BEMT approximation, as the flow at the boundary is prescribed by the boundary condition to be only in the axial direction.

The tip vortices can be examined further in the near-body blade mesh in Figure 5.18(a). It can readily be seen that the "old" vortex lies immediately below the blade tip, with little wake contraction. It can also be seen that the old vortex interacts with the new vortex. This interaction can be examined further in Figure 5.18(b) where it can be seen that the flow stagnates between the two vortices. The tip vortex forming at the blade tip can be examined further in Figure 5.18(c) (with reduced vector magnitude) where the vortex induces a flow from outside the tip region onto the upper surface of the blade.

The induced velocity from the tip vortex can be seen in an axial plane of the

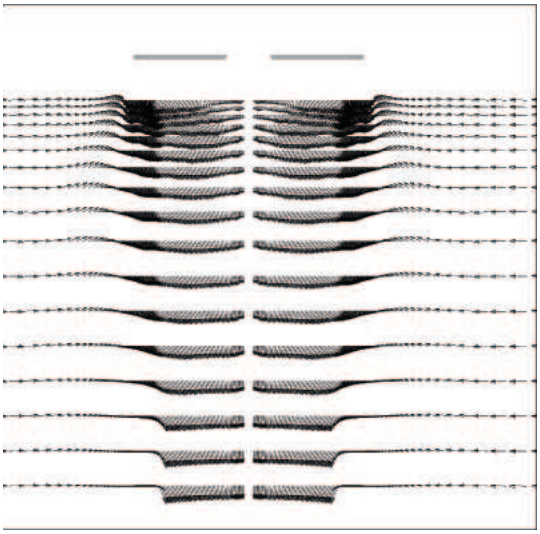

Figure 5.17: Wake Contraction in Hover

background mesh in Figure 5.19(a). Due to the rotation of the vortex, the induced velocity is positive on the outboard portion and negative inboard. The vortex core is also characterized by a low pressure center, as can be seen in Figure 5.19(b). The vortex passes underneath the succeeding blade and induces a velocity on the blade. This is known as a blade-vortex interaction (BVI).

An additional vortex also forms at the blade root, although this vortex is not as strong as the tip vortex because of the difference in local free-stream velocities. The velocity field induced by the root vortex can be seen in Figure 5.20. The root vortex contributes to the amount of turbulent flow in the downwash near the blade root, as can be seen in Figure 5.20(a) where the flow induced by the vortex is up through the root near the blade. Further inboard from the blade in the root cutout region, the flow stagnates and changes direction to flow down through the root cutout, as can be seen in Figure 5.20(b).

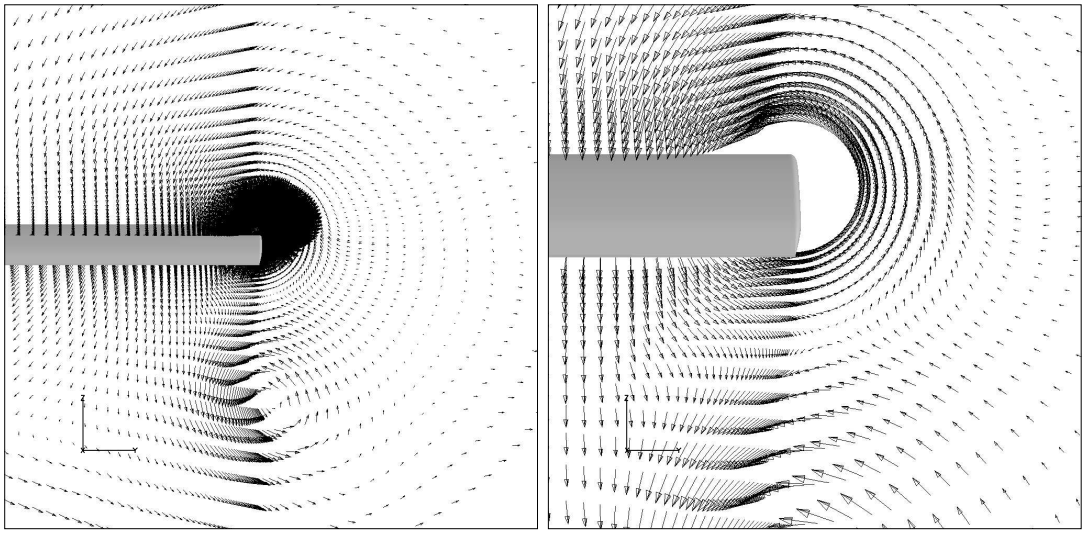

(a) Blade Tip

(b) Blade Tip (vortex omitted for clarity)

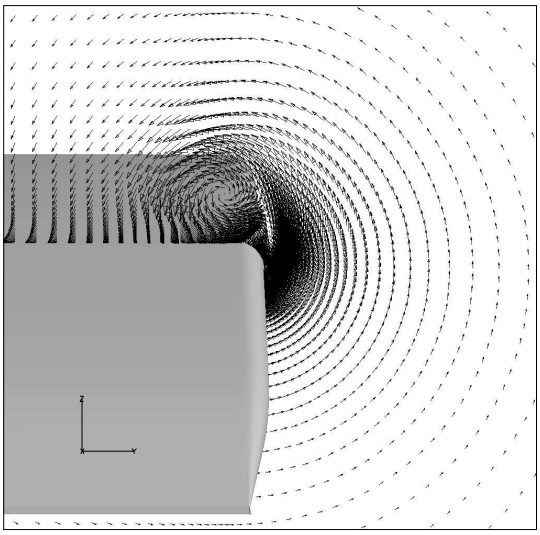

(c) Blade tip (with reduced vector magnitude)

Figure 5.18: Velocity Flow-field at $\theta = 8°$, 63% span, looking from trailing edge

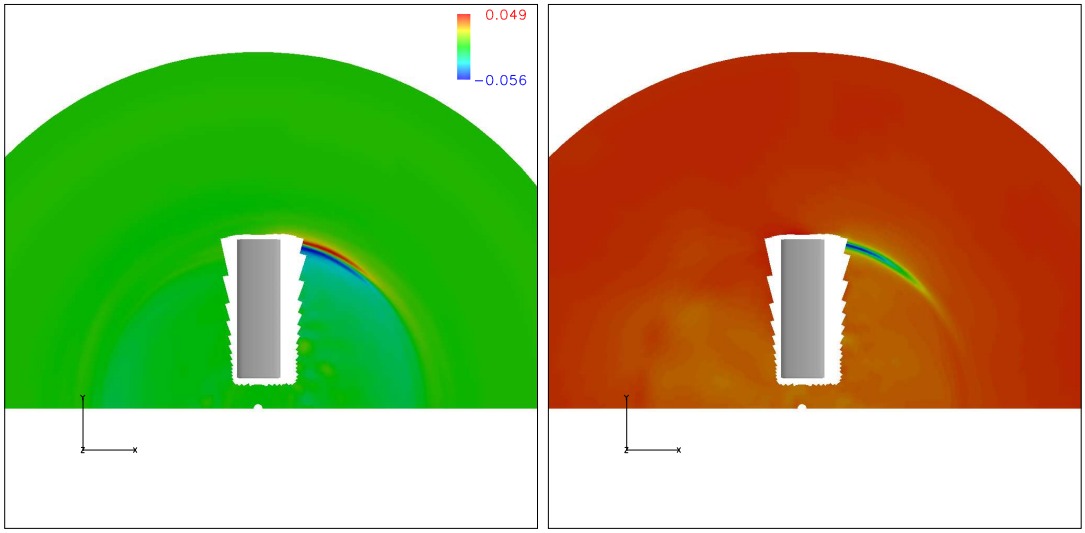

(a) Axial velocity contour at blade surface

(b) Pressure Contour at the blade surface

Figure 5.19: Axial velocity and pressure contours in the plane of the rotor, $\theta = 8°$

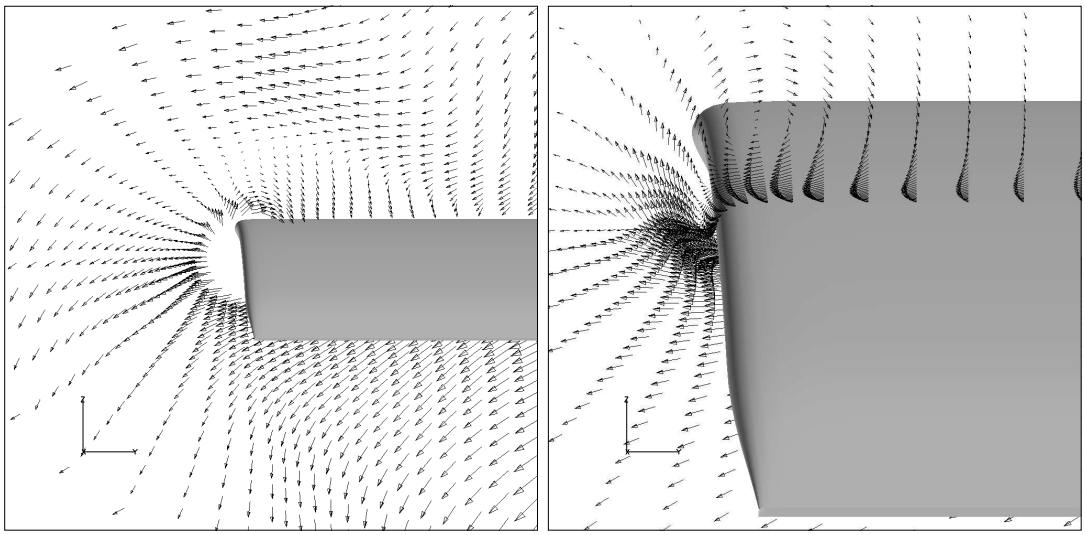

(a) Blade Root (vortex omitted for clarity)

(b) Blade Root

Figure 5.20: Velocity Flowfield at $\theta = 8°$, 63% span, looking from the trailing edge

The effects of the root and tip vortices can be examined further in Figure 5.21, which shows the induced inflow at $\frac{1}{2}c$ below the rotor for $\theta = 12°$. The tip vortex induces a relatively large velocity at this wake location. Beyond $\frac{r}{R} = 1$, the induced velocity of the rotor causes the flow to travel up to the rotor before being flushed through the rotor disk. The effect of the root vortex on the induced inflow is not as strong due to the large wake obstruction as discussed previously in this section.

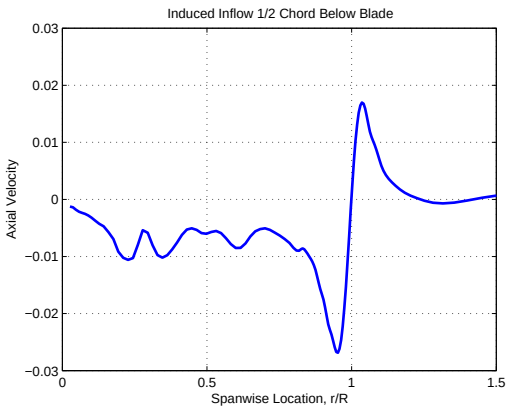

Figure 5.21: Induced Inflow at $\frac{1}{2}c$ Below the Rotor

5.5.4 Lift and Thrust Distributions

Sectional values of lift and thrust can be computed at each spanwise location for both BEMT and computational results, although there is no experimental distribution. The section lift coefficient is computed using the local velocity. The sectional lift distribution can be seen in Figure 5.22 for various collectives, and shows that the inboard portion of the blade has a high sectional lift coefficient. This portion of the blade experiences slight unsteady effects due to the wake obstruction,

as was seen in Figure 5.10. The flow may be recirculating in this region, or even flowing up through the rotor near the blade due to the tip vortex. The lift distribution is relatively constant across the blade span although the tip vortex induces a small velocity in the outboard 5% of the blade. The section lift coefficient increases with collective angle, as expected.

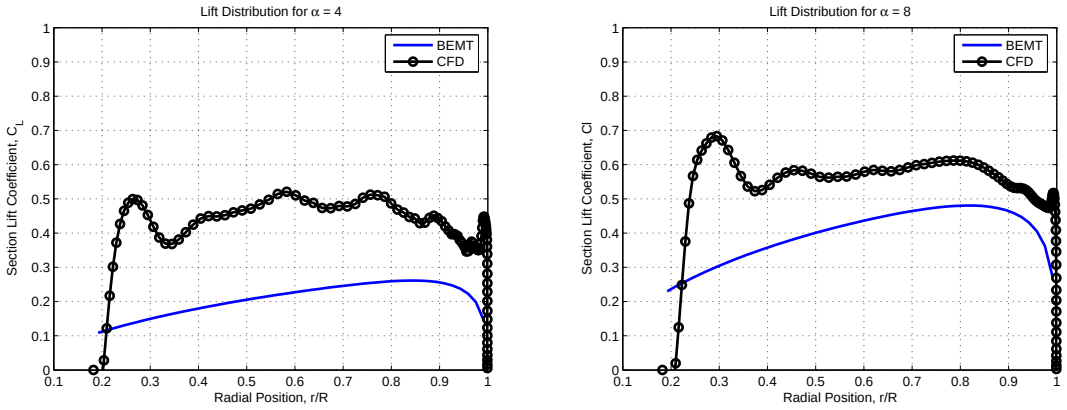

(a) $\theta = 4°$ (b) $\theta = 8°$

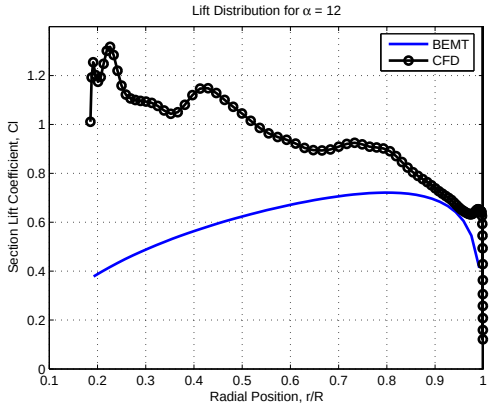

(c) $\theta = 12°$

Figure 5.22: Lift Distribution for Hovering MAV

The spanwise thrust distribution is plotted with the BEMT approximation for several collectives in Figure 5.23. The thrust is calculated with BEMT using the results from equation 5.4. The CFD results agree qualitatively with BEMT predictions, particularly at higher angles of attack. The tip effects are stronger in the CFD due to proper modeling of the induced velocity from the tip vortex forming on the blade, which has a significant effect for low aspect ratio blades. The thrust coefficients in Figure 5.12 were found by integrating the area under the curves in Figure 5.23. The small negative thrust region in Figure 5.23(c) at $\theta = 12°$ is possibly due to the aforementioned unsteady effects at the blade root.

5.5.5 Chordwise Flow Separation

Regions of chordwise flow separation are plotted in Figure 5.24. At $\theta = 4°$, there is only a small portion of flow recirculation on the upper surface of the blade. As the collective angle increases to $\theta = 8°$, the region of separation expands toward the trailing edge. Upon subsequent increase in collective, the region of flow separation expands further outboard and towards the leading edge at $\theta = 10°$. At $\theta = 14°$, the flow has stalled over the inboard portion of the blade (except near the root where the root vortex reduces the effective angle of attack). There are several regions on the blade where the flow separates and quickly reattaches. At the leading edge, this is probably due to the LSB. The flow is also separated at the trailing edge, similar to static 3-D computations where the turbulent boundary layer is unattached at high angles of attack.

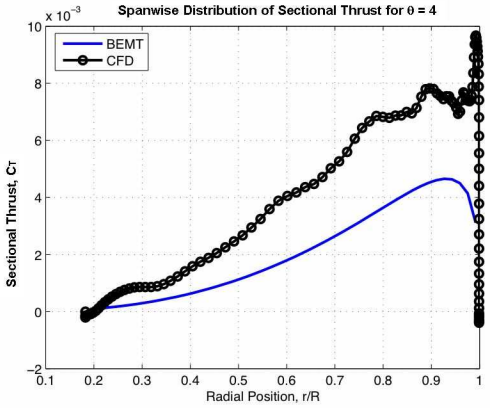

(a) $\alpha = 4°$

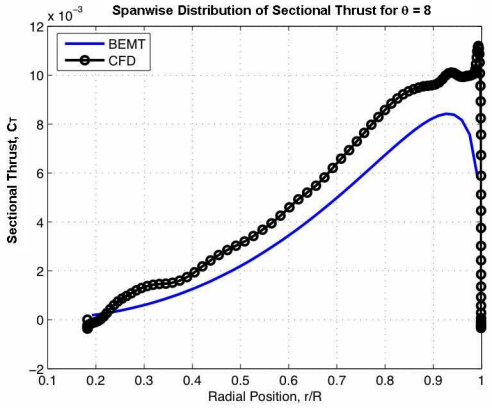

(b) $\alpha = 8°$

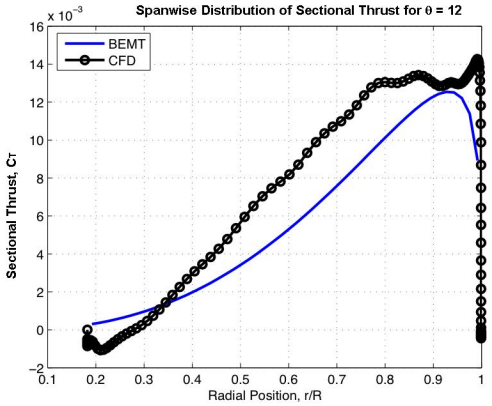

(c) $\alpha = 12°$

Figure 5.23: Spanwise Thrust Distribution for Hovering MAV

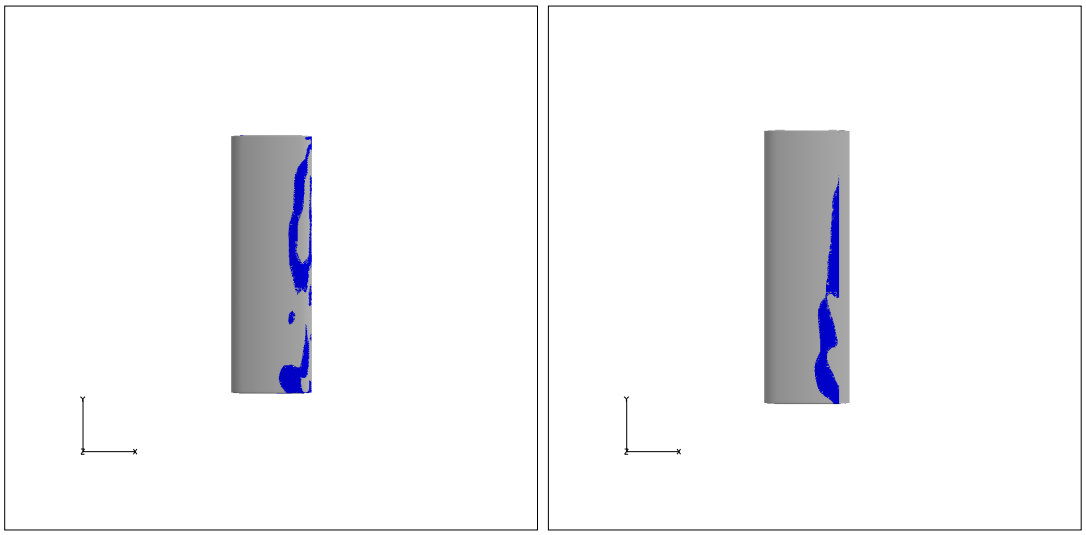

(a) $\theta = 4°$ (b) $\theta = 8°$

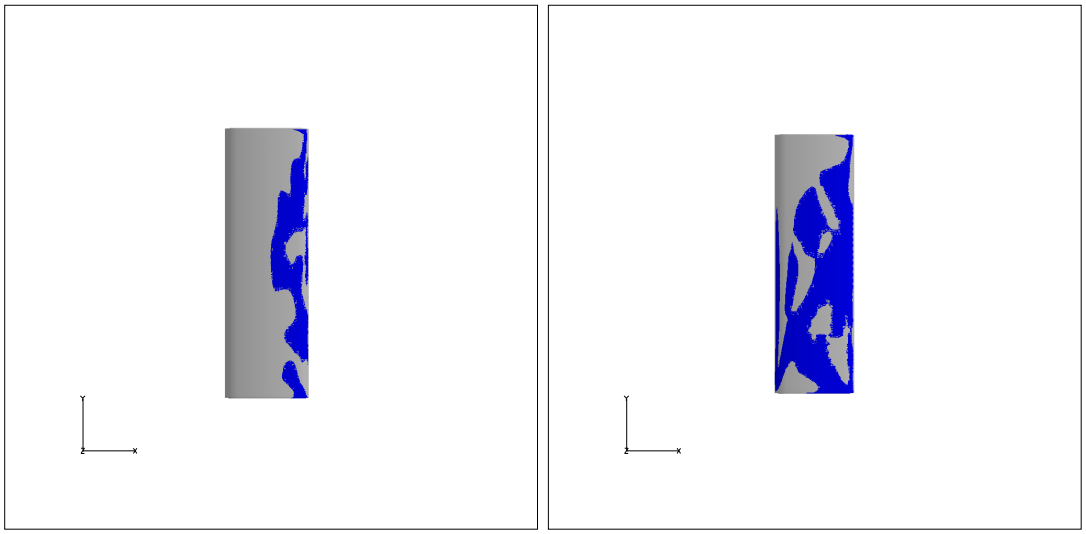

(c) $\theta = 10°$ (d) $\theta = 14°$

Figure 5.24: Regions of chord-wise flow separation

5.5.6 Summary

The Hein airfoil has been analyzed from a static 2-D, 3-D, and rotary 3-D perspective. The 2-D and 3-D results show high maximum lift coefficient while predicting stall at a higher angle of attack than the Eppler and Mueller airfoils. Chordwise pressure distributions show that the sharpened leading edge may trip the boundary layer, leading to increased performance. For the hover 3-D computations, the performance of the Hein MAV rotor was slightly over-predicted compared to BEMT and experimental results. High sectional lift coefficients were measured inboard where experimentally, there was significant wake obstruction at the root. The shed tip vortex captured in the wake showed no contraction after one half rotor revolution, which probably led to an over prediction of sectional lift and thrust on the outboard portion of the blade. Although there was a difference between predicted thrust and figure of merit, valuable insight has been gained into the effect of applying hover boundary conditions onto static 3-D results. The hover model could be improved at significant computational expense to include more detailed resolution of the background mesh to capture the shed vortices with higher fidelity, and could be extended to capture swirl effects in the rotor wake. However, at the validation level, the TURNS flow solver does reasonably well in extending its capability to a hovering rotor.

Chapter 6

Summary and Conclusions

Rotary Micro Air Vehicle (MAV) development is hindered in part by poor aerodynamic performance at low Reynolds numbers. Because these aircraft fly in the operational Reynolds number range of 20,000 to 70,000, the flow over the blades are significantly influenced by viscous forces. Low Reynolds number flows have been researched more frequently in the last decade and the amount of experimental knowledge is growing. Additionally, several computational studies have been made recently although the Reynolds numbers are generally not in the appropriate range for rotary wing MAVs. Few of these computational studies have investigated thin, highly cambered airfoils together with rotary wing MAVs. The methodologies for the 2-D and 3-D computations are then extended to a hovering rotor using the same flow solver, low Mach preconditioner, and turbulence model to allow for comparisons to be made between airfoils. Understanding the computational flow physics leads to a fundamental understanding of the problems and issues regarding CFD for MAVs and low Reynolds number flow in general.

The key to good computational results at low Reynolds number lies in the prediction of the laminar separation bubble (LSB). At low Reynolds numbers, LSBs tend to form on the upper surface of an airfoil, often between the leading edge and mid-chord. If the bubble is short, it will act as a boundary layer trip to turbulent

flow, thereby increasing performance. Conversely, if the bubble is long, the airfoil will have a relatively low maximum lift coefficient and will stall at a relatively low angle of attack. Thus, the development of the LSB plays an important role in the aerodynamic performance of a MAV.

To examine the flow physics particular to low Reynolds number flows and LSB development, computational fluid dynamics (CFD) is used. In static 2-D, an airfoil is modeled as a viscous wall in a C-type mesh whereas in static 3-D, the tip is closed into a C-O type mesh to better resolve the tip vortex. Overset meshes are used for hover 3-D cases where a cylindrical background mesh encloses the local blade mesh. The TURNS and OVERFLOW flow solvers are used (with the Spalart–Allmaras turbulence model) to reach the steady-state solution, and it is therefore possible to validate experimental lift, moment, and drag measurements with results from CFD.

This thesis marks an addition to the literature by validating low Reynolds number data from different wind tunnels in static 2-D and 3-D experiments. An emphasis has been given to understanding the flow physics by thoroughly analyzing the computational flow field. The importance of resolving the laminar separation bubble cannot be under-emphasized, as this is the key to resolving the lift-curve slope and stall characteristics. CFD has been used in this thesis to gain an understanding of spanwise lift and thrust distributions which are not easily measured in an experiment.

The main results from the CFD are:

- Experimental data for the Eppler 387 airfoil has been validated at a Reynolds

number of 60,000. CFD shows good agreement through the majority of the angle of attack range experienced by MAVs for the lift, moment, and drag coefficients. The formation of a LSB causes a slight bump in the lift and drag curves where the bubble moves forward on the airfoil with increasing angle of attack. Examining the pressure contours confirms the existence of a LSB on the upper surface at moderate to high angles of attack. This airfoil exhibits trailing edge stall combined with a LSB bursting, and the TURNS flow solver does an excellent job capturing stall at the same angle of attack as was measured experimentally.

- The slightly cambered circular arc from Mueller was validated in 2-D over a series of angles of attack. The lift, drag, and moment were validated with good agreement with experimental data. This airfoil experiences thin airfoil stall with a relatively low maximum lift coefficient. The LSB forms at a shallow angle of attack near the leading edge and elongates as the angle of attack is increased, until eventually the bubble bursts and the flow is separated over the entire airfoil. Due to the LSB, the boundary layer is relatively thick over most of the airfoil. Both OVERFLOW and TURNS predict stall reasonably well, though at a lower angle of attack than was measured experimentally.

- The Mueller airfoil was also investigated for a 3-D wing of low aspect ratio. The lift, moment, and drag curves showed very good agreement with experimental data, possibly due to the true 3-D nature of the experiment. The tip vortex was captured with good fidelity and the spanwise distribution of lift also closely

resembled representative curves. By examining the local vorticity and pressure at the tip, it was discovered that the tip vortex had a somewhat larger effect on the spanwise lift distribution due to the low aspect ratio of the wing. The induced velocity from the tip vortex reduces the local angle of attack, and thus the flow remains attached at relatively high angles of attack when the flow may be unattached inboard on the wing. The effects of increasing the Reynolds number were also examined and it was found that increasing the Reynolds number from 60,000 to 120,000 leads to moderate performance improvements while increasing from 120,000 to 240,000 leads only to a slight improvement in performance.

- The Hein MAV rotor was investigated at Reynolds number of 51,200, at an RPM of 5500 ($M = 0.114$). The thin, cambered airfoil with a sharpened leading edge that was used on the rotor was initially investigated from static 2-D and 3-D perspectives to gain insight into the flow physics. Relatively high lift coefficients were seen at all angles of attack, although this was accompanied by relatively large nose-down pitching moments and a significant increase in drag compared to the Eppler and Mueller airfoils. The airfoil stalled at a relatively high angle of attack, partially because of the sharpened leading edge which served as a boundary layer trip.

- For the hover computations, the flowfield over the 2-bladed Hein rotor was modeled computationally by half of the rotor disk with a periodic boundary condition. The rotor also had a large root cutout which experimentally led to

a large wake obstruction. The experimental figure of merit was relatively low compared to full-size helicopters due to the high rotor solidity, high zero-lift drag coefficient, and high induced power coefficient. The calculated thrust and figure of merit from the TURNS flow solver were slightly overpredicted compared to experimental data and Blade-Element Momentum Theory (BEMT). This was possibly due to high sectional lift coefficients over the inboard region of the blade. Additionally, the wake did not contract after one half rotor revolution in the computations, where the tip vortex was lying directly below the blade tip. The vortex location has an influence on the section lift coefficient, and so one would expect the blade-vortex interaction to have a more significant effect than was found computationally.

6.1 Future Work

Continuing work on this research project will focus on mainly on computational areas:

- Now that the low Mach preconditioner has been validated, the focus can shift to analyzing the effects of various turbulence and transition models that may resolve the flow more correctly at the airfoil surface.
- Adding significantly more points at the root and tip locations may allow for better resolution of the 3-D effects.
- Adding significantly more points in a wake capturing systems would give better resolution for resolving the blade-vortex interaction. Using the results from

the recent work in Ref. [35], the vortex may be able to be captured better with turbulence model modifications. Additionally, the wake contraction may be able to be improved by taking swirl effects at the bottom boundary into account.

- Making the TURNS code (with low Mach preconditioner) parallel will save significantly on computational time.

- From a performance perspective, results may also be able to be improved by examining the inflow characteristics near the rotor hub and blade root cutout. In the Hein experiment, there was a significant amount of flow blockage found at the root, and so placing more points in this region may give better results. Alternatively, the rotor hub could be modeled as a solid wall to prevent flow recirculation in this region.

- It may be worthwhile to examine the relationship between induced power and profile power at these low Reynolds numbers to see if any coupling exists between them, and if so, whether this is significant enough to warrant a new metric for measuring MAV performance.

- It may also be worthwhile to examine how BEMT approximations could take the blade aspect ratio and Reynolds number into account, as these both degrade rotor performance.

BIBLIOGRAPHY

[1] Mueller, T.J., "Aerodynamic Measurements at Low Reynolds Numbers for Fixed Wing Micro-Air Vehicles," Presented at the RTO AVT/VKI Special course on Development and Operation of UAVs for Military and Civil Applications, September 13-17, 1999, VKI, Belgium.

[2] Kunz., P.J., and Strawn, R.C., "Analysis and Design of Rotors at Ultra-low Reynolds Numbers," 40th AIAA Aerospace Sciences Meeting and Exhibit, Reno, NV, January 2002.

[3] Bohorquez, F., Rankins, F., Baeder, J.D., and Pines, D.J., "Hover Performance of Rotor Blades at Low Reynolds Numbers for Rotary Wing Micro Air Vehicles. An Experimental and CFD Study," 21st AIAA Applied Aerodynamics Conference, Orlando, FL, June 2003.

[4] Sathaye, S., Yuan, J., and Olinger, D.J., "Lift Distributions on Low-Aspect-Ratio Wings at Low Reynolds Number for Micro-Air Vehicle Applications," 22nd AIAA Applied Aerodynamics Conference, Providence, RI, June 2004.

[5] Selig, M.S., Guglielmo, J.J., Broern, A.P., Giguere, P., "Experiments on Airfoils at Low Reynolds Numbers," 34th AIAA Aerospace Sciences Meeting and Exhibit, Reno, NV, January 1996.

[6] Torres, G.E., and Mueller, T.J., "Low-Aspect-Ratio Wing Aerodynamics at Low Reynolds Numbers," *AIAA Journal*, Vol. 42, No. 11, pp. 865-873.

[7] Pelletier, A., and Mueller, T.J., "Low Reynolds Number Aerodynamics of Low-Aspect-Ratio, Thin/Flat/Cambered-Plate Wings," *Journal of Aircraft*, Vol. 37, No. 5, pp. 825-832.

[8] Laitone, E.V., "Wind Tunnel Tests of Wings at Reynolds Numbers Below 70000," *Experiments in Fluids* Vol. 23, 1997, pp 405-409.

[9] Mönttinen, J.T. "Computational Study of the Effect of Winglets on the Performance of Micro-Aerial Vehicles," Ph. D. Dissertation. Arizona State University, AZ, 2004.

[10] Selig, M.S., Champine, B., "Low-Speed Airfoil Data - Volume 3: E387C.LFT," http://www.aae.uiuc.edu/m-selid/pub/lsat/vol1/E387C.LFT Accessed 20 September 2004.

[11] Hein, B.R., "Hover Performance of a Micro Air Vehicle: Rotors at Low Reynolds Number," 2005 AHS Lichten Award Competition.

[12] Carmichael, B.H., "Low Reynolds Number Airfoil Survey," Volume I, NASA Contractor Report 165803, November, 1981.

[13] Bastedo, W.G., and Mueller, T.J., "Spanwise Variation of Laminar Separation Bubbles on Wings at Low Reynolds Number," *Journal of Aircraft,* Vol. 23, No. 9, September 1986, pp.687-694.

[14] Marchman, J.F., "Aerodynamic Testing at Low Reynolds Numbers," *Journal of Aircraft,* Vol. 24, February, 1987, pp. 107-114.

[15] Lowson, M.V., "Aerodynamics of Aerofoils at Low Reynolds Numbers," UAVs - 14th Unmanned Air Vehicle Systems International Conference, United Kingdom, April, 1999.

[16] Ol, M.V., McAuliffe, B.R., Hanff, E.S., Scholz, U., and Kahler, C., "Comparison of Laminar Separation Bubble Measurements on a Low Reynolds Number Airfoil in Three Facilities," 35th AIAA Fluid Dynamics Conference, Toronto, June, 2005.

[17] Laitone, E.V., "Aerodynamic Lift at Reynolds Numbers Below 7×10^4," *AIAA Journal,* Vol. 34, No. 9, pp 1941-1942.

[18] O'Meara, M.M., and Mueller, T.J., "Laminar Separation Bubble Characteristics on an Airfoil at Low Reynolds Numbers," *AIAA Journal,* Vol. 25, No. 8, pp. 1033-1041.

[19] Kroo, P., "The Mesicopter," *Ph. D. Dissertation*, Stanford, CA, November, 2001.

[20] Singh, A.P., "A Computational Study on Airfoils at Low Reynolds Numbers," Proceedings of the ASME Fluids Engineering Division, FED-253, ASME, 2000, pp 405-411.

[21] Kellogg, M.I., and Bowman, W.J., "Parametric Design Study of the Thickness of Airfoils at Reynolds Numbers from 60,000-150,000," 42nd AIAA Aerospace Sciences and Exhibit, Reno, Nevada, January, 2004.

[22] Shum, Y.K., Marsden, D.J., "Sepration Bubble Model for Low Reynolds Number Airfoil Applications," *Journal of Aircraft*, Vol. 31, No. 4., July, 1994, pp. 761-766.

[23] Elimelch, Y., Arieli, R., and Iosilevskii, G., "On the Onset of Transition at Low Reynolds Number Flow Over Airfoils," 4th AIAA Theoretical Fluid Mechanics Meeting, Toronto, Canada, June, 2005.

[24] Gupta, V., Baeder, J.D., "Low Mach Number Preconditioning for Tiltrotor Rotor-Wing Interaction," AHS 4th Decennial Specialist's Conference on Aeromechanics, San Francisco, CA, January, 2004.

[25] Leishman, J.G., Principles of Helicopter Aerodynamics, Cambridge University Press, Cambridge, England, UK, 2000, Chapter 7.

[26] White, F.M. Viscous Fluid Flow, McGraw-Hill, Inc., New York, NY, 1991, Chapter 4.

[27] Leishman, J.G., Principles of Helicopter Aerodynamics, Cambridge University Press, Cambridge, England, UK, 2000, Chapter 2.

[28] Holst, T., Elements of Computational Fluid Dynamics, March, 1991.

[29] White, F.M. Viscous Fluid Flow, McGraw-Hill, Inc., New York, NY, 1991, Chapter 1.

[30] Srinivasan, G., and Baeder, J.D., "TURNS: A Free Wake Euler/Navier-Stokes Numerical Method for Helicopter Rotors," *AIAA Journal,* Vol. 31 No. 5, May 1993, pp. 2371-2378.

[31] Gupta, V., *Ph.D. Dissertation*, University of Maryland, College Park, 2005.

[32] Baldwin, B. and Lomax, H., "Thin Layer Approximation and Algebraic Model for Separated Flows," AIAA paper 78-257.

[33] Durbin, P., "A Reynolds Stress Model for Near Wall Turbulence," *Journal of Fluid Mechanics,* Vol. 249.

[34] Spalart, P., and Allmaras, S., "A One Equation Turbulence Model for Aerodynamic Flows," 30th Aerospace Sciences Meeting and Exhibit, AIAA, Reno, NV, January, 1992.

[35] Duraisamy, K., "Studies in Tip Vortex Formation, Evolution, and Control," *Ph.D. Dissertation,* University of Maryland, College Park, 2005.

[36] Buning, P.G., Jespersen, D.C., Pulliam, T.H., Chan, W.M., Slotnick, J.P., Krist, S.E., and Renze, K.J., "OVERFLOW User's Manual, Version 1.8g," NASA Langley Research Center, March 1999.

[37] Leishman, J.G., Principles of Helicopter Aerodynamics, Cambridge University Press, Cambridge, England, UK, 2000, Chapter 3.